

# Instabilities in layered liquids induced by external fields

Von der Universität Bayreuth  
zur Erlangung des Grades eines  
Doktors der Naturwissenschaften (Dr. rer. nat.)  
genehmigte Abhandlung

von

Günter Auernhammer

geboren am 9. Dezember 1971 in Weißenburg/Bayern

1. Gutachter: Prof. Dr. H. R. Brand  
2. Gutachter: Prof. Dr. H. Pleiner

Tag der Einreichung: 21. Juli 2003  
Tag des Kolloquiums: 26. Januar 2004



*“Es ist schlimm genug”, rief Eduard, “dass man jetzt nichts mehr für sein ganzes Leben lernen kann. Unsre Vorfahren hielten sich an den Unterricht, den sie in ihrer Jugend empfangen; wir aber müssen jetzt alle fünf Jahre umlernen, wenn wir nicht ganz aus der Mode kommen wollen.”*

*J. W. Goethe [42]*



---

# Contents

<b>Contents</b>	<b>i</b>
<b>List of Technical Notes</b>	<b>v</b>
<b>Zusammenfassung</b>	<b>vii</b>
<b>1 Introduction</b>	<b>1</b>
1.1 General considerations . . . . .	1
1.2 Experimental motivation . . . . .	4
1.2.1 Alignment of oriented samples . . . . .	4
1.2.2 Reorientation phenomena under applied shear . . . . .	6
1.3 Standard description of liquid crystals . . . . .	7
1.3.1 Nematic liquid crystals . . . . .	8
1.3.2 Smectic- <i>A</i> liquid crystals . . . . .	10
1.4 Review of other approaches . . . . .	12
1.5 Remark . . . . .	13
<b>2 Motivation and basic idea</b>	<b>15</b>
2.1 A theorist's view . . . . .	15
2.2 Motivation for the present approach . . . . .	16
2.3 Physical idea of the model . . . . .	18
<b>3 Including the director</b>	<b>23</b>
3.1 Macroscopic hydrodynamic equations . . . . .	23
3.2 Solution techniques . . . . .	32
3.3 Spatially homogeneous state . . . . .	35

3.4	Stationary instability . . . . .	36
3.4.1	Minimal set of variables . . . . .	36
3.4.2	Coupling to the velocity field . . . . .	38
3.4.3	Including the order parameters . . . . .	45
<b>4</b>	<b>Linear Analysis: Discussion of the results</b>	<b>51</b>
4.1	Oscillatory instability . . . . .	51
4.2	Effect of other external fields . . . . .	52
4.3	Comparison to experiments . . . . .	55
<b>5</b>	<b>Comparison to MD simulations</b>	<b>57</b>
5.1	Molecular dynamics simulations: basics . . . . .	57
5.1.1	Integration scheme . . . . .	58
5.1.2	Coupling to a heat bath . . . . .	59
5.1.3	Shear algorithm . . . . .	60
5.1.4	Model system . . . . .	61
5.2	Results of the molecular dynamics simulations . . . . .	63
5.3	Comparison analytic theory <i>vs.</i> simulations . . . . .	65
5.3.1	Details of the analytic approach . . . . .	65
5.3.2	Comparison . . . . .	69
5.3.3	Concluding remarks . . . . .	71
<b>6</b>	<b>Weakly non-linear analysis</b>	<b>73</b>
6.1	General procedure . . . . .	73
6.2	Iterative solution . . . . .	76
<b>7</b>	<b>Summary and conclusions</b>	<b>81</b>
<b>A</b>	<b>Frozen-in magnetic order in uniaxial gels</b>	<b>85</b>
A.1	Introduction . . . . .	85
A.2	Experimental part . . . . .	86
A.2.1	Preparation of the samples . . . . .	86
A.2.2	Measurements . . . . .	87
A.3	Results . . . . .	88

---

A.3.1	Magnetic properties of the gel cylinders . . . . .	88
A.3.2	Optical properties of thin samples . . . . .	89
A.3.3	Mechanical measurements . . . . .	90
A.4	Discussion . . . . .	91
A.5	Conclusions and perspective . . . . .	92
<b>B</b>	<b>Comparison to the first model</b>	<b>95</b>
<b>C</b>	<b>Generating the set of governing equations</b>	<b>97</b>
C.1	Definitions and structuring the equations . . . . .	97
C.2	Linearization and the adjoint problem . . . . .	102
C.3	Hierarchy of equations . . . . .	104
C.3.1	Order $a^2$ . . . . .	104
C.3.2	Order $a^3$ . . . . .	105
	<b>References</b>	<b>109</b>

*CONTENTS*

---



# List of Technical Notes

1.1	Typical shear geometries . . . . .	5
2.1	Linear stability analysis . . . . .	18
3.1	Reversible currents . . . . .	30
3.1	(continued) . . . . .	31
3.2	Typical values of the material parameters . . . . .	37
6.1	Properties of the amplitude equation . . . . .	75
6.2	Absence of $\theta^{(1)}$ . . . . .	77

*LIST OF TECHNICAL NOTES*

---

# Zusammenfassung

## I Experimentelle Motivation

Diese Dissertation ist durch die Ergebnisse einer Reihe von Scherexperimenten an lamellaren Phasen motiviert worden. Untersucht wurden z.B. lamellare Phasen von Blockcopolymeren [48, 49, 62, 69, 106, 119, 123, 127, 132, 135, 145], niedermolekulare thermotrope Flüssigkristalle [55, 101, 114], lyotrope lamellare Phasen von niedermolekularen [29, 31, 85, 88, 142] und polymeren [140, 141] amphiphilen Molekülen und flüssigkristalline Polymere [93, 95]. Meist wird für Systeme mit niedriger Viskosität (z.B. niedermolekulare lyotrope Systeme) ein Rheometer in Couette-Anordnung gewählt, während die Messungen an hochviskosen Materialien (z.B. Blockcopolymeren) oft an den sog. Kegel-Platte oder Platte-Platte Anordnungen durchgeführt werden (s. Abb. 1).

Trotz all dieser Unterschiede in den Details zeichnet sich eine erstaunliche gemeinsame Tendenz in diesen Experimenten ab: Ist das System in einer Konfiguration präpariert, in der die Schichten parallel zu den Ebenen konstanter Geschwindigkeit liegen (“parallele” Orientierung), so ist diese Konfiguration bis zu einer kritischen Scherrate stabil. Wird die Scherrate jedoch über einen kritischen Wert erhöht, so wird die parallele Orientierung instabil. Nach hinreichend langer Zeit findet man dann entweder Schichten, die senkrecht zur Vortizitätsrichtung ausgerichtet sind (also in der Ebene liegen, die durch die Geschwindigkeits- und Gradientenrichtung aufgespannt wird, “senkrechte” Orientierung), oder die Lamellen haben sich zu geschlossenen, zwiebelartigen Strukturen (multi-lamellaren Vesikeln) aufgerollt. Diese Destabilisierung der parallelen Orientierung ist umso überraschender als die Standardformulierung der entsprechenden hydrodynamischen Theorie (jene von smektisch-*A* Flüssigkristallen [25, 26, 81, 104]) eine solche Instabilität nicht vorhersagt.

## II Physikalischer Mechanismus

Da Unterschiede im mikroskopischen Aufbau der experimentellen Systeme zu vergleichbaren Ergebnissen führen, scheint es angemessen, eine möglichst allgemeine Theorie als Grundlage einer erweiterten Theorie zu benutzen: Die hydrodynamische Beschreibung von smektisch-*A* Flüssigkristallen ist ein geeigneter Ausgangspunkt für einen solchen Zugang. Im Rahmen der theoretischen Beschreibung nähern wir die verschiedenen Scher-

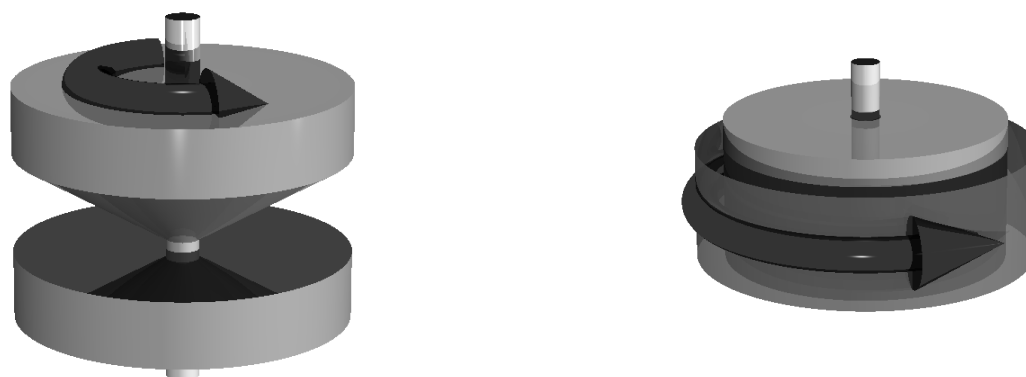


**Abbildung 1:** Zwei typische Rheometer in schematischer Darstellung: Links eine Kegel-Platte Anordnung, rechts ein Couette-Rheometer.

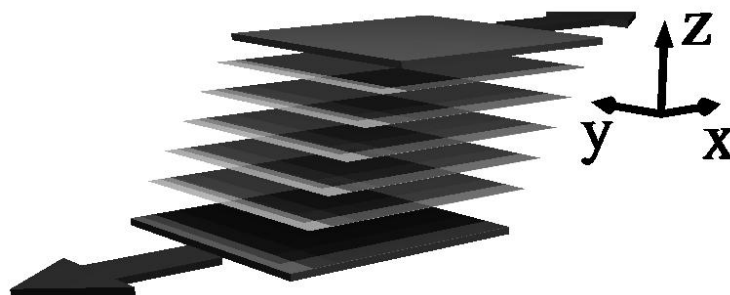


**Abbildung 2:** Die verschiedenen Schergeometrien werden durch zwei parallele, unendlich ausgedehnte Platten, die sich mit gleicher (konstanter) Geschwindigkeit in entgegengesetzte Richtungen bewegen, angenähert.

geometrien durch zwei parallele, unendlich ausgedehnte Platten an. Beide Platten bewegen sich mit gleicher (konstanter) Geschwindigkeit in entgegengesetzten Richtungen (s. Abb. 2).

Ein Gedankenexperiment am Beispiel niedermolekularer thermotroper Flüssigkristalle führt uns zu der gesuchten Erweiterung der makroskopisch-hydrodynamischen Beschreibung von smektisch-*A* Flüssigkristallen. In einem smektisch-*A* Flüssigkristall sind die Moleküle bevorzugt in Schichten angeordnet. Zusätzlich sind die Molekülachsen im Mittel parallel zur Schichtnormalen ausgerichtet. Vernachlässigen wir nun für einen Moment die Schichtstruktur, so haben wir ein System vor uns, das einem nematischen Flüssigkristall in homeotroper Orientierung sehr ähnlich ist. Von nematischen Flüssigkristallen ist aber bekannt, dass eine von außen angelegte Scherung ein Drehmoment auf den Direktor (die gemittelten Molekülachsen) ausübt. Dieses Drehmoment führt im einfachsten Fall zum sog. *flow alignment*, einem Kippen des Direktors in Flussrichtung.

Die Grundidee unseres Zugangs ist, dass dieses Drehmoment auch in der smektisch-*A* Phase vorhanden ist. Der Direktor ist aber so an die Schichtnormale gekoppelt, dass im Gleichgewicht beide parallel sind. Unter dem Einfluss äußerer Felder wird das Drehmo-

ment auf den Direktor durch ein Drehmoment, das durch die Kopplung an die Schichtnormale entsteht, kompensiert. Daraus folgt dann ein endlicher (aber meist kleiner) Winkel zwischen der Schichtnormalen und dem Direktor. Als Ursache für diesen Kippwinkel kommt nicht nur ein Scherfeld in Frage, auch von außen angelegte elektrische oder magnetische Felder wirken auf Direktor und Schichtnormale unterschiedlich und können so eine Verkipfung des Direktors erzeugen. Dieser Kippwinkel ist keine hydrodynamische Variable im strengen Sinn, vielmehr handelt es sich hierbei um eine langsam relaxierende Größe.

### III Theoretische Behandlung

Die Methoden der irreversiblen Thermodynamik erlauben uns mit Hilfe von Symmetrieargumenten die makroskopisch-hydrodynamischen Gleichungen für unser erweitertes Modell eines smektisch-*A* Flüssigkristalls aufzustellen. Dabei berücksichtigen wir die smektischen Freiheitsgrade (Schichtverschiebung und smektischer Ordnungsgrad), die nematischen Freiheitsgrade (Direktor und nematischer Ordnungsgrad) und das Geschwindigkeitsfeld als makroskopische Variablen. Wir analysieren den so erhaltenen Satz von makroskopisch-hydrodynamischen Gleichungen in mehreren Schritten:

- Räumlich homogener Zustand bei gegebener Geschwindigkeit der Platten
- Stabilitätsbereich dieses räumlich homogenen Zustands als Funktion der verschiedenen Materialparameter
- Schwach nicht-lineare Analyse an der Grenze des Stabilitätsbereichs

#### III.a Räumlich homogener Zustand

Hat man als Ausgangszustand eine defektfreie smektische Schichtung in paralleler Orientierung, so ergibt sich folgendes Bild: Ein lineares Scherprofil löst die Impulserhaltungsgleichung. Der Kippwinkel des Direktors ist für kleine Scherraten proportional zur Scherrate, während die smektische Schichtung unverändert bleibt.<sup>1</sup>

Die bevorzugte Dicke einer smektischen Schicht ist proportional zur Projektion der gemittelten Molekülachsen (des Direktors) auf die Schichtnormale. Als Folge des Kippwinkels verkürzt sich jeodoch diese Projektion. Somit ist das Verkippen des Direktors  $\hat{n}$  um einen Winkel  $\theta$  gleichbedeutend zu einer effektiven Dehnung der Schichten (bei festgehaltener tatsächlicher Schichtdicke wird die bevorzugte Schichtdicke verringert, s. Abb. 3).

---

<sup>1</sup>Im Fall eines angelegten Magnetfelds ist der Kippwinkel proportional zum Quadrat der Magnetfeldstärke.

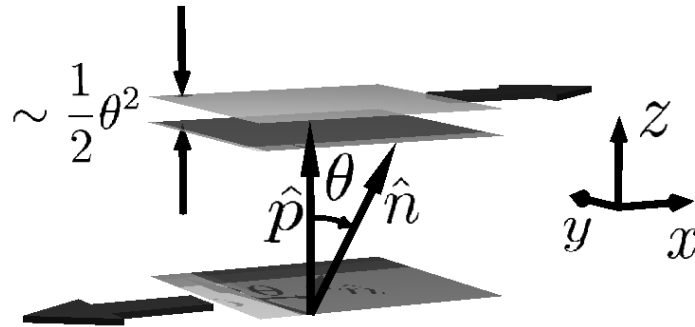


**Abbildung 3:** Ein endlicher Winkel  $\theta$  zwischen der Schichtnormalen  $\hat{p}$  und dem Direktor  $\hat{n}$  ist gleichbedeutend mit einer effektiven Dehnung der Schichten. Im Fall kleiner  $\theta$  ist die effektive Dehnung proportional zu  $\theta^2/2$ .

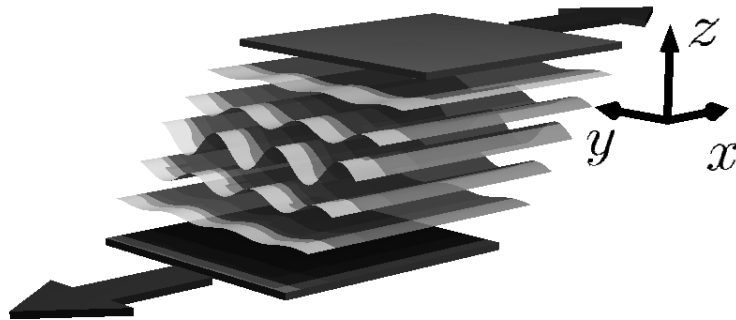


**Abbildung 4:** Oberhalb einer kritischen Schwelle für die Scherrate reagiert das System mit einer undulatorischen Instabilität auf die effektive Dehnung.

### III.b Lineare Stabilitätsanalyse

Es zeigt sich, dass der oben beschriebene räumlich homogene Zustand oberhalb einer kritischen Scherrate instabil gegen eine undulatorische Instabilität ist<sup>2</sup> (vgl. Abb. 4). Der Wellenvektor dieser Undulationen zeigt in Vortizitätsrichtung, d.h. er ist senkrecht zur Fluss- und Gradientenrichtung. Als Funktion der Materialparameter variiert der kritische Kippwinkel des Direktors deutlich. Für einen typischen niedermolekularen thermotropen Flüssigkristall ergibt sich ein kritischer Kippwinkel  $\theta$  von ein paar Grad. Für alle physikalisch interessanten Werte der Materialparameter können wir eine oszillatorische Instabilität ausschließen.

Koppelt man den Betrag des (nematischen oder smektischen) Ordnungsparameters, den Ordnungsgrad, an diese hydrodynamischen Gleichungen, so bleiben die kritischen Werte praktisch unverändert, der Ordnungsgrad unduliert jedoch analog zu den Schichten. Die Undulationen des Ordnungsgrades sind in der Nähe des Randes maximal. Diese Undula-

---

<sup>2</sup>Eine ähnliche Instabilität ist auch an smektisch-A Phasen zu beobachten, die senkrecht zu den Schichten gedehnt werden [16, 28].

tionen des Ordnungsgrads zeigen einen Weg auf, wie die Schichtstruktur aufgebrochen werden kann. Defekte werden bevorzugt in Regionen mit niedrigerem Ordnungsgrad gebildet, weil dort die mit den Defekten verbundene Energie niedriger ist. Eine genaue Analyse des Einflusses von Defekten würde jedoch den Umfang dieser Arbeit sprengen.

### III.c Schwach nicht-lineare Analyse

Aus der linearen Stabilitätsanalyse können keine Aussagen über die Struktur der Instabilität oberhalb der Schwelle abgeleitet werden. Deshalb bestimmen wir die Art der Bifurkation (super- oder subkritisch) mit Hilfe einer schwach nicht-linearen Analyse. Es zeigt sich, dass in fast allen physikalisch relevanten Bereichen des Parameterraums die Bifurkation superkritisch ist. Insbesondere wächst dann die Amplitude der Undulationen kontinuierlich mit dem Abstand zur Schwelle an, dabei ist die Amplitude proportional zur Quadratwurzel des Abstands zur Schwelle.

## IV Vergleich der Ergebnisse mit Experimenten und Molekular-Dynamik-Simulationen

### IV.a Experimente

Qualitativ stimmt die hier entwickelte Theorie gut mit den zu Beginn erwähnten Experimenten überein. Neuere Experimente an lyotropen Systemen zeigen, dass der Übergang von parallelen Lamellen zu multi-lamellaren Vesikeln über einen Zwischenzustand führt. Dieser Zwischenzustand besteht entweder aus undulierenden Lamellen oder aus multi-lamellaren Zylindern. Für das in diesen Experimenten benutzte System sind genügend Materialparameter bekannt, so dass ein semi-quantitativer Vergleich mit der oben entwickelten Theorie möglich ist. Aus diesem Vergleich ergibt sich, dass der Durchmesser der beobachteten Objekte vergleichbar ist mit der kritischen Wellenlänge der Undulationen.

### IV.b Molekular-Dynamik-Simulationen

Im Rahmen einer Kooperation mit Simulationsphysikern vom Max-Planck-Institut für Polymerforschung in Mainz konnte ein detaillierter Vergleich mit Molekular-Dynamik-Simulationen durchgeführt werden. Simuliert wurde ein Modellsystem für geschichtete Flüssigkeiten, bestehend aus viergliedrigen Kettenmolekülen  $A_2B_2$ , mit den beiden Monomeren A und B. Die Teilchen in einer Kette sind durch Federn verknüpft. Teilchen verschiedener Ketten ziehen sich an, wenn sie gleichartig sind, und stoßen sich ab, wenn sie verschiedenartig sind. Schersimulationen an der lamellaren Phase dieses Systems bestätigen zwei wichtige Vorhersagen des analytischen Modells:

- Die Scherung bewirkt ein Verkippen des Direktors in Flussrichtung, wobei die Schichten zunächst unverändert bleiben.

- Oberhalb einer kritischen Scherrate bilden sich stationäre Undulationen aus, deren Wellenvektor in Vortizitätsrichtung zeigt.

Außer diesen qualitativen Übereinstimmungen ergibt der quantitative Vergleich ein (im Rahmen der gemachten Näherungen) befriedigendes Ergebnis.

## V Schlussbemerkungen

In dieser Arbeit wird eine erweiterte makroskopisch-hydrodynamische Beschreibung von smektisch-*A* Flüssigkristallen entwickelt. Zentraler Punkt dieser Beschreibung ist, dass der Direktor (die gemittelten Molekülachsen) und die Schichtnormale in smektisch-*A* Flüssigkristallen nicht starr aneinander gekoppelt sind, sondern, unter dem Einfluss äußerer Felder, einen endlichen Winkel einschließen können. Diese Erweiterung erlaubt eine direkte Interpretation von Scherexperimenten an einer Reihe von Systemen, die ähnlich zu smektisch-*A* Flüssigkristallen sind. Vergleiche mit experimentellen Ergebnissen und Molekular-Dynamik-Simulationen zeigen eine gute qualitative und eine semi-quantitative Übereinstimmung.

## VI Experimenteller Anhang: Herstellung und Charakterisierung uniaxialer magnetischer Gele

Im Rahmen einer binationalen Kooperation mit der Arbeitsgruppe vom P. Martinoty an der Université Louis Pasteur (Strasbourg, Frankreich) war der Autor an der Herstellung und Charakterisierung uniaxialer magnetischer Gele beteiligt.

Die magnetischen Eigenschaften des Gels gehen auf magnetische Nanoteilchen zurück, die in die Gelmatrix eingebettet sind. Ein angelegtes Magnetfeld während der Vernetzungsreaktion führt zu einer leicht beobachtbaren optischen und magnetischen Anisotropie des Gels. Das Gel besitzt eine endliche, eingefrorene Magnetisierung, was zu einem für Ferromagnete typischen Verhalten in kleinen, homogenen Magnetfeldern führt. Messungen des Schermoduls während der Vernetzungsreaktion zeigen, dass sich das Fortschreiten der Reaktion durch eine Kohlrausch-Williams-Watts-Funktion (gestreckte Exponentialfunktion) beschreiben lässt. Im Gegensatz zu den magnetischen und optischen Eigenschaften ist das Gel mechanisch isotrop.



---

# Chapter 1

## Introduction

### 1.1 General considerations

A simple picture (like the one we all have learned in high-school) distinguishes between three states of matter: solid, liquid, and gas. But nature is too creative to fit in such a simple scheme and after a closer look, things become more complicated. The first complication comes in when we are scanning everyday examples for these states of matter. For example solids may be isotropic (*i.e.*, invariant under rotations) and homogeneous (*i.e.*, invariant under translations) like window glass. But solids may also be well oriented like a salt crystal. For many materials (like water) the structure of the solid state depends on the thermal history: When cooling water slowly, it freezes and forms ice crystals, but when the temperature drop is too fast a amorphous, glassy state will result. Also the liquid state of matter may be more complex: Liquids are typically isotropic and homogeneous. But in 1888/89 Reinitzer synthesized and Lehmann interpreted correctly [70] a first prominent exception:<sup>1</sup> Liquid crystals (“fliessende Krystalle”). The notion liquid crystal, which sounds like a contradiction, describes a state which is neither solid nor isotropically liquid but combines partial order with fluid-like properties. In the 1920s Vorländer and coworkers synthesized and characterized many liquid crystalline substances (see, *e.g.*, Refs. [125, 126] for reviews).

At this point a short review of the properties of crystals is helpful. In most crystals the building units (group of atoms or molecules) are stacked in a well ordered way: They have a well defined orientation and their centers of mass form a regular lattice. For a typical crystal there is a direct transition from the isotropic liquid to this ordered state. In liquid crystals the situation is different and each of the discussed ordering phenomena (orientational ordering of the molecules, positional ordering of the centers of mass along the three spatial directions) can appear separately. Thus giving rise to a huge family of so called mesophases.<sup>2</sup> In the following we concentrate only on those phases which are

---

<sup>1</sup>According to Lehmann, Reinitzer published his findings in Refs. [109, 110] and as a personal communication to Lehmann.

<sup>2</sup>We refer the reader, *e.g.*, to Ref. [26] for an overview over the mesophases of liquid crystals.

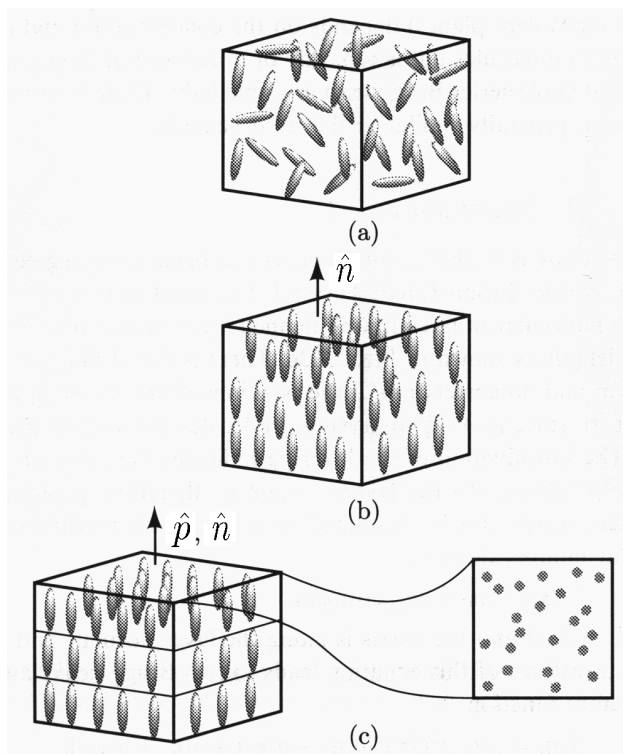


**Figure 1.1:** A possible sequence of mesophases for a liquid crystal. With decreasing temperature first the isotropic liquid (a) is transformed into a state in which the molecules are oriented on average along one direction (the director  $\hat{n}$ ) but the centers of mass have no order: the nematic phase (b). When cooling further, the centers of mass of the molecules order in layers with a layer normal  $\hat{p}$ . In (c) a smectic-*A* phase is shown, where  $\hat{p}$  and  $\hat{n}$  are parallel (picture taken from Ref. [13]). At the end of such a sequence of mesophases, typically, the system reaches either a glassy or a crystalline state.

relevant for this work. Figure 1.1 gives an example of a possible sequence of mesophases including an isotropic, a nematic (no positional order but on average orientational order along the director  $\hat{n}$ ) and a smectic-*A* phase (additionally, positional order along a layer normal  $\hat{p}$ , which is parallel to  $\hat{n}$ ). When cooling further some other mesophases might appear. At low temperatures the system typically reaches a crystalline or a glassy state.

The above description was originally developed for low molecular weight thermotropic liquid crystals. These are typically rather small (typical size: 20 – 40 Å) organic molecules (called mesogens) which exhibit in their liquid phase a sequence of mesophases. Since the arguments are only based on the symmetry properties of the system, these are not restricted to low molecular weight liquid crystals and similar phases can also be observed in a number of different systems,<sup>3</sup> *e.g.*:

- **Liquid crystalline polymers and elastomers:** The mesogens can be connected in two ways to polymer chains. If (some or all) of the monomers forming the polymer chains are mesogens one speaks of a main chain liquid crystalline polymer. Alternatively the mesogens can be connected as side chains to the main chain of the polymer *via* (flexible) spacers to make up a side chain liquid crystalline polymer (see Fig. 1.2). In the present work no results from main chain liquid crystalline polymers are considered, because in these systems the dynamics is dominated by the polymer dynamics. In contrast, side chain liquid crystalline polymers behave

<sup>3</sup>These systems are part of the field of complex liquids and/or soft condensed matter.

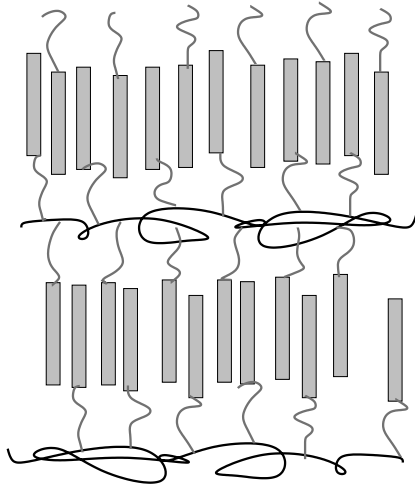


**Figure 1.2:** Sketch of a side chain liquid crystalline polymer in the smectic- $A$  phase. The mesogens (gray rectangles) are connected to the polymer backbone (black) *via* flexible spacers (gray).



**Figure 1.3:** Sketch of a lyotropic liquid crystal in the  $L_\alpha$  phase. The space between the lamellae is filled with solvent (water).

more liquid crystalline like. Many of the phases known from low molecular weight liquid crystals also exist in liquid crystalline polymers. The polymer backbones can also be crosslinked forming a liquid crystalline elastomer.

- **Lyotropic system:** In contrast to thermotropic liquid crystals (see above), which change between different liquid crystalline phases as a function of temperature, lyotropic liquid crystals exhibit the mesophases as a function of concentration. A simple example of lyotropic liquid crystals is a concentrated aqueous solution of surfactant molecules (having a hydrophilic head and a hydrophobic tail). Among other phases this system shows a smectic- $A$ -like phase (often called  $L_\alpha$  phase, see Fig. 1.3) consisting of stacked flat bilayers. This system has two microscopic length scales: The membrane thickness (approximately given by twice the surfactant length, typically 20 – 30 Å) and the repeat distance, which can be several times larger than the membrane thickness.
- **Block copolymers:** Block copolymers are macromolecules built up from polymer chains of different types. These polymer chains are connected by covalent bonds, leading in the simplest case to a diblock copolymer. When the two blocks are (below a certain temperature) immiscible, they segregate on a microscopic scale.<sup>4</sup> Below this  $T_{ODT}$  (temperature of the order-disorder transition) block copolymers form ordered phases. The structure of the phase is mainly given by the length

<sup>4</sup>A macroscopic phase separation is hindered by the bonds between the blocks and can only occur in polymer blends.

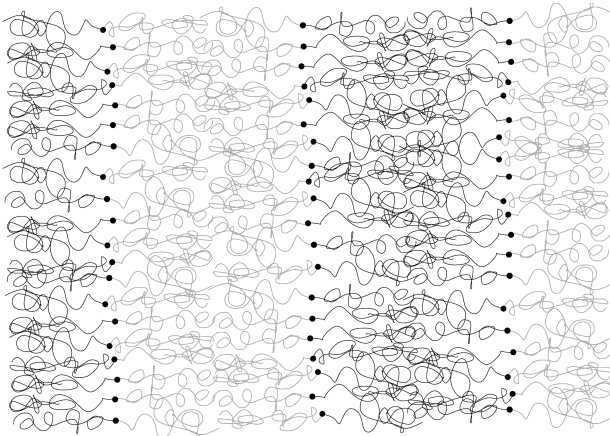


**Figure 1.4:** Sketch of a diblock copolymer below the  $T_{ODT}$  in the lamellar phase.

of the blocks. As a function of the ratio between the two block lengths, diblock copolymers form a number of mesophases, including a smectic- $A$ -like phase at a ratio of about 1:1 (see Fig. 1.4). The repeat distance of these lamellar phases is (depending on the molecular weight of the polymer) typically in the range from 10 nm to 100 nm.

In this thesis, we deal with the reaction of the smectic layering in these systems to an applied external field. The main part is dedicated to the influence of an applied shear field, but we also discuss other fields. Our work has been motivated by a number of experiments which we review in the following section.

## 1.2 Experimental motivation

Submitted to an applied external field, these complex liquids show an interesting coupling between their internal structure and the flow field.

### 1.2.1 Alignment of oriented samples

External fields can orient the existing mesophase over large distances. In low molecular weight liquid crystals applying electric or magnetic fields is a standard technique to produce aligned samples. Recently, it has been shown that also block copolymers can be aligned when the order-disorder transition takes place in an external electric field [8, 121].

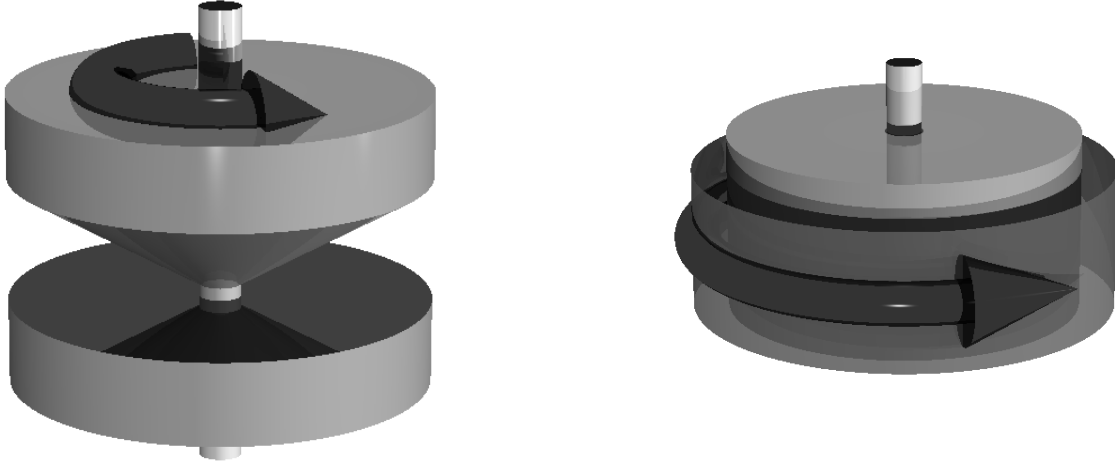
As first observed by Keller and coworkers [36, 59] shear can orient the ordered phase of block copolymers.<sup>5</sup> We note that these first experiments were not done on lamellar phases. But when a renewed interest on the flow properties of block copolymers arose in the 1990's, a similar alignment of the lamellar phase was observed in many systems.

---

<sup>5</sup>In their case the shear was applied *via* an extrusion process, *i.e.*, the shear rate was not constant.

**Technical Note 1.1** Typical shear geometries

Normally, the experiments described in this section are performed in one of the following shear geometries.



On the left we show a cone-plate rheometer which is typically used for large amplitude oscillatory shear in highly viscous materials like block copolymers. In a cone-plate geometry the average shear rate is constant throughout the sample but the sample thickness varies. Some of the experiments are done with a rheometer where the upper cone is replaced by a plate (plate-plate geometry). Then the amplitude of the shear is a function of the position in the sample but the sample has a uniform thickness.

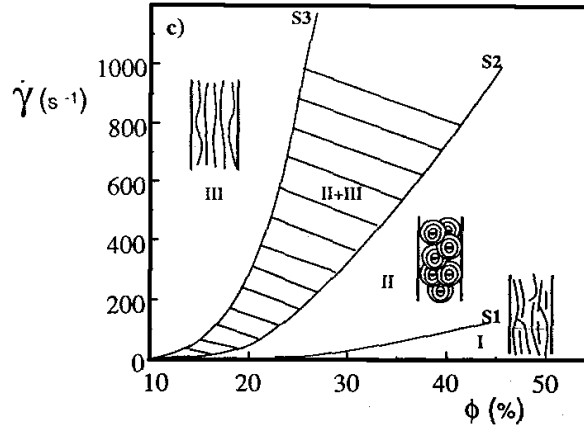
The Couette cell depicted on the right is normally used in shear experiments using systems with lower viscosities, like lyotropic materials. Often Couette cells are used to apply a steady rather than an oscillatory shear.

Due to these different geometries a detailed and direct comparison between all the systems mentioned is not straightforward.

When the block copolymer melt is cooled down below the order-disorder temperature into the lamellar phase, a polydomain sample is obtained. If a large amplitude oscillatory shear is applied to such a sample<sup>6</sup> the layers orient with the layer normal  $\hat{p}$  either parallel or perpendicular to the plates [48, 49, 62, 119, 123, 127, 132, 135, 145]. Which orientation is obtained after applying large amplitude oscillatory shear for some time (typically hours) seems to depend on the details of the sample preparation (thermal history) and the way of applying the shear (amplitude, frequency and temperature of the sample). For an overview over these experiments see, *e.g.*, Ref. [132]. These experiments are typically done in cone-plate or plate-plate rheometers (see Technical Note 1.1).

<sup>6</sup>“Large amplitude” in this case means strain amplitudes of the order of 1.

**Figure 1.5:** Roux and coworkers [29] investigated the orientation behavior of a lyotropic  $L_\alpha$  phase (using a Couette type rheometer). At low shear rates  $\dot{\gamma}$  they observed a stable parallel orientation. When increasing the shear rate, the parallel lamellae became unstable and formed multi-lamellar vesicles (“onions”). As depicted in this plot the critical shear rate depends on the volume fraction  $\phi$  of the surfactant (plot taken from Ref. [29]). For low surfactant concentrations further structural changes appear at higher shear rates.



## 1.2.2 Reorientation phenomena under applied shear

A number of experiments show that aligned samples, which are stable under (or have formed under) certain shear conditions, can become unstable and reorganize to a different orientation. The investigated systems differ significantly in their microscopic details, but show nevertheless striking similarities in their macroscopic behavior under shear.

The systems under investigation include block copolymers [48, 49, 62, 69, 106, 119, 123, 127, 132, 135, 145], low molecular weight thermotropic liquid crystals [55, 101, 114], lyotropic lamellar phases (both low molecular weight [29, 31, 85, 88, 142] and polymeric [140, 141]), and liquid crystalline side-chain polymers [93, 95].

The common features of all these experiments can be described as follows. Starting with an aligned sample where the layers are parallel to the planes of constant velocity (“parallel” orientation), the layering is stable up to a certain critical shear rate [29, 71, 85, 88, 101, 114, 132, 142, 140, 141].<sup>7</sup>

At higher shear rates, the situation depends on the nature of the system (in Figs. 1.5 and 1.6 we show two examples). Either multi-lamellar vesicles [29, 31, 88, 141] (“onions”, typically in lyotropic systems) form or the layers seem to turn by  $90^\circ$  such that they include the velocity and the gradient direction [48, 69, 71, 94, 101, 114, 132, 145] (“perpendicular” orientation, typically in solvent free systems).

In some of the systems a third regime is observed at even higher shear rates with a parallel orientation [29, 71]. If the starting point of the experiment is a randomly distributed

<sup>7</sup>In steady shear experiments the “shear rate” is directly defined. In experiments with large amplitude oscillatory shear Leist *et al.* [71] have shown for diblock copolymers that the control parameter for the destabilization of the parallel alignment is proportional to the oscillation frequency of the upper plate/cone times the shear amplitude, *i.e.*, the shear rate.

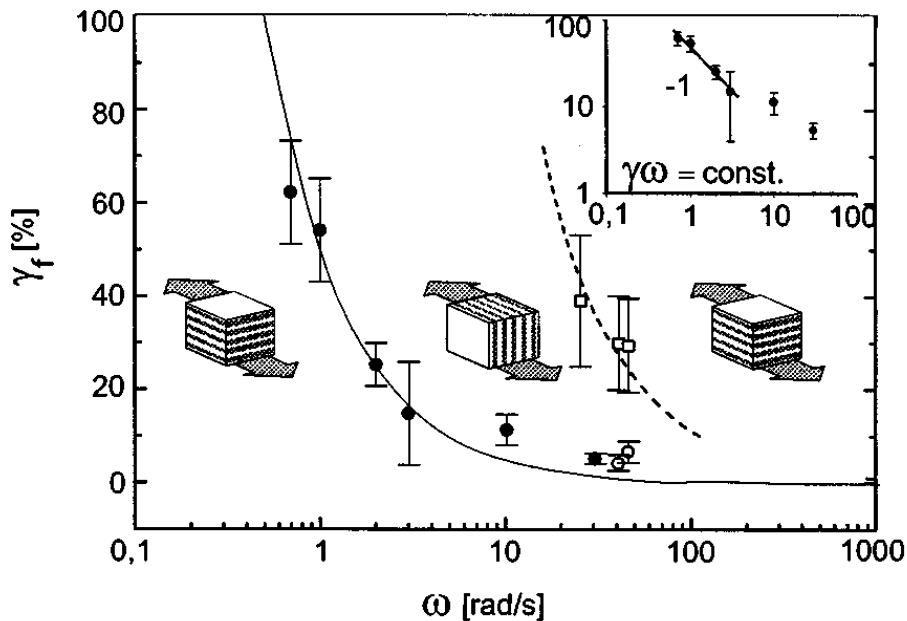


**Figure 1.6:** Wiesner and coworkers [68, 71, 73, 132, 138] investigated in detail the behavior of the parallel alignment of diblock copolymers under large amplitude oscillatory shear (using a plate-plate geometry). They observed a transition from the original parallel alignment to the perpendicular alignment with increasing frequency  $\omega$  and increasing amplitude  $\gamma_f$  of the shear. The plot shows that the transition is controlled by the shear rate (the solid line shows a  $\omega \cdot \gamma_f = \text{const.}$  curve). At higher shear rates a second transition back to parallel layers is observed (plot taken from Ref. [71]).

lamellar phase (*i.e.*, a polydomain sample), the first regime is not observed [31, 48, 127, 145]. This last point illustrates that experiments on layered liquids depend on the history of the sample. In our further discussion we will restrict ourselves to systems showing a well aligned parallel orientation before shear is applied.

The experimental similarities between different systems indicate, that the theoretical description of these reorientations can be constructed, at least to some extent, from a common basis independent of the actual system (on the other hand, a description including the differences between the systems under investigation must refer closer to their microscopic details). When looking for a macroscopic description, the well established standard smectic-*A* hydrodynamics [25, 26, 81, 104] is a good starting point for such a theoretical approach.

### 1.3 Standard description of nematic and smectic-*A* liquid crystals

The main difference between an isotropic liquid and a mesophase is the fact that at least one continuous symmetry of the isotropic system is spontaneously broken. In the

following sections we review the consequences of this symmetry breaking in two examples: the nematic phase (where only the rotational symmetry is broken) and the smectic-A phase (where a positional ordering along one direction is established).

### 1.3.1 Nematic liquid crystals

The nematic phase is characterized by a preferred axis denoted by the director  $\hat{n}$  and the degree of alignment  $S$ . Whereas the definition of the director is straightforward (it is the preferred axis),<sup>8</sup> a suitable expression for  $S^{(n)}$  is more subtle. The conventional definition is to use the weighted average over the distribution function of the molecular axes [24, 26, 76, 77]

$$S^{(n)} = \frac{1}{2} \langle 3 \cos^2 \theta_n - 1 \rangle = \int f(\theta_n) \frac{1}{2} (3 \cos^2 \theta_n - 1) d\Omega, \quad (1.1)$$

with the angle  $\theta_n$  between the director and the actual molecular axis and the distribution function of the molecular axes  $f(\theta_n)$ .

Macroscopically, the nematic phase is characterized by a uniaxial behavior. In contrast to isotropic materials, *e.g.*, the linear materials law connecting the magnetization  $\vec{M}$  with the applied field  $\vec{H}$

$$M = \chi H, \quad (1.2a)$$

where  $\vec{M}$  is parallel to  $\vec{H}$  (and it suffices to write the equation for the moduli), is in the nematic phase no longer a scalar equation.<sup>9</sup> The tensorial character of magnetic susceptibility  $\chi_{ij}$  has to be taken into account

$$M_i = \chi_{ij} H_j, \quad (1.2b)$$

with a uniaxial  $\chi_{ij} = \chi_{\perp} \delta_{ij} + \chi_a n_i n_j$  consisting of an isotropic part proportional to  $\chi_{\perp}$  and an anisotropic contribution proportional to  $\chi_a$ . Using this property one can also construct an suitable order parameter by extracting the traceless anisotropic part of  $\chi_{ij}$  [23, 26]

$$Q_{ij} = G \left( \chi_{ij} - \frac{1}{3} \delta_{ij} \sum_k \chi_{kk} \right). \quad (1.3a)$$

$Q_{ij}$  vanishes in the isotropic phase and its normalization constant  $G$  can be chosen at will. A convenient choice connects  $Q_{ij}$  to  $\hat{n}$  and  $S^{(n)}$ :

$$Q_{ij} = \frac{2}{3} S^{(n)} \left( n_i n_j - \frac{1}{3} \delta_{ij} \right) \quad (1.3b)$$

---

<sup>8</sup>Note that  $\hat{n}$  does not distinguish between head and tail, it defines the axis but no direction.

<sup>9</sup>In the following we will denote a vectorial quantity of unit length (like the director) with a small hat above the symbol (*e.g.*,  $\hat{n}$ ) and all vectorial quantities with an arrow on top of the symbol (*e.g.*,  $\vec{M}$ ). In both cases the components get a Latin index (*e.g.*,  $n_i$ ,  $M_j$ ). Tensorial quantities are either denoted with an underlined symbol (*e.g.*,  $\underline{\chi}$ ) or with two Latin indices (*e.g.*,  $\chi_{ij}$ ).  $\delta_{ij}$  represents the Kronecker symbol.



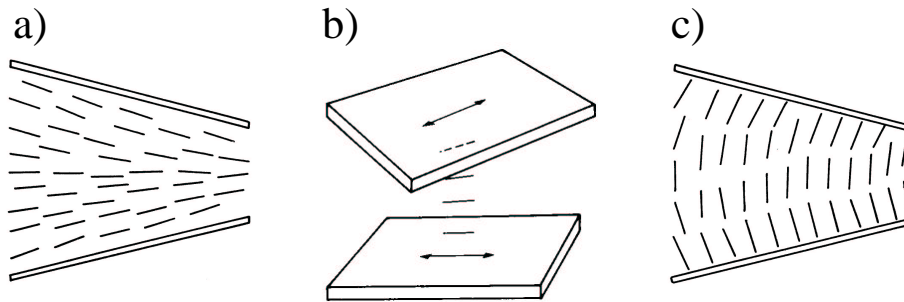


**Figure 1.7:** The three basic deformations of a nematic liquid crystal: a) splay, b) twist, and c) bend. (pictures taken from Refs. [14, 26])

In the following we will describe the nematic degrees of freedom using the director  $\hat{n}$  and the strength of the nematic order  $S^{(n)}$ . However, we note that a description of the nematic phase using  $Q_{ij}$  is also possible (see, *e.g.*, Refs. [52, 53]).

In the absence of external fields, the rotational symmetry of the isotropic fluid is broken spontaneously at the transition to the nematic phase. This implies that all orientations of the director are equivalent and (spatially homogeneous) states which differ in their director orientation are energetically equivalent. In other words, the free energy of the system cannot depend on the director orientation itself. But spatially inhomogeneous variations in the director field will cost energy. One can expect that the nematic part of the free energy is an analytic expansion in gradients of the director. As Frank [38] has first shown, the lowest order terms in this expansion can be written as:

$$\begin{aligned} \epsilon_{nemat} = & \frac{1}{2}K_1(\nabla \cdot \hat{n})^2 + \frac{1}{2}K_2[\hat{n} \cdot (\nabla \times \hat{n})]^2 \\ & + \frac{1}{2}K_3[\hat{n} \times (\nabla \times \hat{n})]^2. \end{aligned} \quad (1.4)$$

The three elastic constants  $K_1$ ,  $K_2$ , and  $K_3$  are connected with splay, twist and bend deformations of the director (see Fig. 1.7).

When exposed to external fields, a nematic liquid crystal shows characteristic instabilities, *e.g.*, the well known Fredericksz transition. An additional term in the free energy couples the director to an external magnetic field (in cgs units):

$$\epsilon_{mag} = -\frac{1}{2}\chi_a \left( \hat{n} \cdot \vec{H} \right)^2 \quad (1.5)$$

This instability is typically observed in a thin cell (thickness  $d \sim 10 - 100\mu\text{m}$ ), where boundaries are treated such that the director is perpendicular to the boundaries (homeotropic alignment). In the absence of the boundaries the director would turn such that it is parallel to the field.<sup>10</sup> In the presence of boundaries, the director is fixed at the boundaries and can only turn in the bulk of the sample. The elastic energy connected

<sup>10</sup>In a typical low molecular weight nematic liquid crystal the anisotropic part of the magnetic susceptibility is positive.

with this deformation gives rise to a lower threshold for the magnetic field necessary to observe an instability. If the magnetic field lies within the sample plane, the director turns in the direction of the applied field for fields larger than

$$H_c = \frac{\pi}{d} \sqrt{\frac{K_1}{\chi_a}}. \quad (1.6)$$

A coupling to another external field (the deformation of the elastomer matrix) can be observed in nematic liquid single crystal elastomers. These elastomers can be synthesized such that they exhibit a single domain in the nematic phase (liquid single crystal elastomers, see Ref. [66]). If these elastomers are stretched perpendicular to the director, the director turns towards the stretching direction leading to reorientation of the director [64, 65, 128, 129].

### 1.3.2 Smectic-*A* liquid crystals

In smectic-*A* liquid crystals a positional ordering along one axis is established. The resulting planes can be described by a density wave

$$\rho(\vec{r}) = \rho(z) = \rho_0 + \rho_1 \cos\{q_0[z - u(\vec{r})]\} + \dots, \quad (1.7)$$

with the arbitrary choice  $\hat{p} \parallel \hat{e}_z$ . The variable  $u(\vec{r})$  describes the layer displacement out of their equilibrium position and the wave vector  $\vec{q}_0 = q_0 \hat{e}_z$  incorporates the layering and is parallel to the layer normal  $\hat{p}$ . To characterize a smectic-*A* phase one needs the strength of the ordering (which is proportional to  $\rho_1$ ) and the position of the layers. For the latter one there are two possibilities: i) In a situation with small curvature, the layer displacement is the more convenient variable. ii) For strong deformations the phase  $\varphi = z - u$  has to be used [79, 105]. A suitable order parameter is the complex number [25, 26]

$$\Phi = S^{(s)} \exp\{iq_0(z - u)\}, \quad (1.8)$$

where  $S^{(s)}$  is proportional to  $\rho_1$ . In this thesis we only consider small deviations from flat layers, consequently,  $u$  and  $S^{(s)}$  are good variables in our case.

The smectic part of the free energy must be invariant under rigid translations and rotations of the whole system. Therefore, the layer displacement  $u$  and its first in-plane gradients cannot contribute to the free energy.<sup>11</sup> The lowest order gradient expansion of the smectic-*A* free energy is given by [26]:

$$\begin{aligned} \epsilon_{smect} = & \frac{1}{2} B_0 (\nabla_{\parallel} u)^2 + \frac{1}{2} K (\nabla_{\perp}^2 u)^2 \\ & + \frac{1}{2} K' (\nabla_{\parallel}^2 u)^2 + \frac{1}{2} K'' (\nabla_{\parallel}^2 u) (\nabla_{\perp}^2 u). \end{aligned} \quad (1.9)$$

---

<sup>11</sup>Note that, in a linear approximation, first transverse gradients are equivalent to rotations of the system.

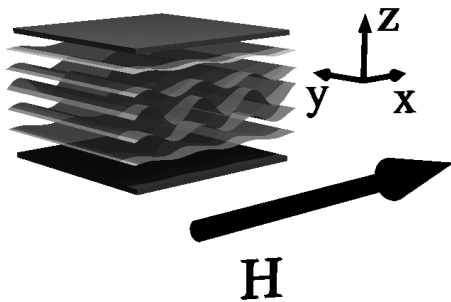


**Figure 1.8:** Smectic- $A$  liquid crystals with a positive anisotropy of the magnetic susceptibility  $\chi_a$  exhibit an undulation instability (Helfrich-Hurault instability) under an applied transverse magnetic field (for high enough fields).

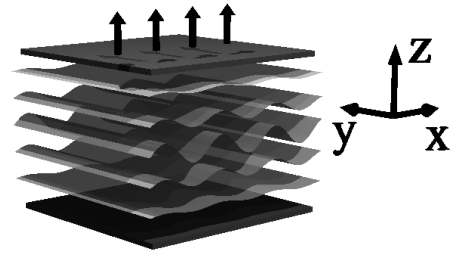


**Figure 1.9:** Dilation perpendicular to the smectic layers induce, above a finite but usually small relative dilation, an undulation instability.

Here we used the parallel and transverse nabla symbols ( $\nabla_{\parallel}$  and  $\nabla_{\perp}$ ), which denote the gradients parallel and perpendicular to the preferred direction (the layer normal). The terms in the second line of Eq. (1.9) are only given for completeness. In fact, they are typically not observable because they are dominated by the  $B_0$  term. For this reason, we will neglect them throughout this thesis. The remaining two terms represent layer dilation/compression and curvature of the layers, respectively.

Similarly to nematic liquid crystals, smectic- $A$  liquid crystals show characteristic instabilities under external fields. In the same geometry as for the Freedericksz transition in the nematic liquid crystal, also a smectic- $A$  liquid crystal shows an instability under an applied magnetic field. In this case the tendency of the molecules to align with the external field is hindered by two facts. Similar to the nematic case there might be orienting effects of the boundaries. And, more importantly, the smectic layers must be compressed to allow a rotation of the layer normal. Due to the layered structure, a global reorientation is not possible, but the layers can rotate locally and develop an undulation instability (known as the Helfrich-Hurault instability [50, 57]<sup>12</sup>). A typical situation is depicted in Fig. 1.8.

Due to the positional ordering along one direction, a smectic- $A$  liquid crystal is also sensitive to mechanical deformations along this direction. When the layers are dilated along their layer normal they can accommodate this stress by a rotation (*i.e.*, by increasing their apparent thickness along the direction of the stress). However, in a finite sample a layer rotation is necessarily connected with a compression of the layers at some point and so a global reorientation is again impossible. In contrast local rotations are possible. As pointed out by Clark and Meyer [16] and Delaye, Ribotta, and Durand [28], a dilation of the smectic layers leads, above a threshold, to an undulation instability of the layers.

<sup>12</sup>We note that the calculations by Helfrich and Hurault have been performed for cholesteric liquid crystals, which have a macroscopic description similar to smectic- $A$ .

Since the compression modulus of the smectic layers is rather high, the threshold value of the relative dilation  $\varepsilon_c$  is typically small and given by

$$\varepsilon_c = 2\frac{\pi}{d}\sqrt{\frac{K}{B_0}}, \quad (1.10)$$

with the layer thickness  $d$ . The situation just above onset is sketched in Fig. 1.9. This instability is also observed in block copolymers, see, *e.g.*, Refs. [18, 19]. Weilepp and Brand investigated a similar situation in liquid single crystal elastomers [128, 130]. In agreement with experiments by Nishikawa and Finkelmann [90, 92, 91] they found an undulation instability.

Before finishing this section on smectic- $A$  liquid crystals, we note that the Landau-Peierls instability for one-dimensional solids (see, *e.g.*, Ref. [67]) is also present in smectic- $A$ -like systems. This instability destroys long range order in one-dimensional solids due to a diverging fluctuation amplitude of the layer displacement. For all experimental sample thicknesses the actual fluctuation amplitude is so small that this instability can be neglected. The signature of the Landau-Peierls instability is, however, measurable (for lyotropic systems see, *e.g.*, Ref. [113]).

## 1.4 Review of other approaches

The above considerations were only based on arguments about conserved quantities and the symmetry of the system. For this reason they are independent of the actual microscopic structure of the systems. As already mentioned in the experimental part of this introduction, the systems under investigation vary significantly in their microscopic structure. In contrast to our macroscopic hydrodynamic approach, for some systems there are other approaches which include more microscopic features of the systems.

In lyotropic liquid crystals the material parameters introduced in the previous sections can be related to the properties of single membranes (as first shown by Helfrich [51]). The main result of Helfrich is that the compression modulus  $B_0$  of lyotropic systems is due to the fluctuation of the lamellae. Coupling these fluctuations of the membranes to the shear some authors also found the possibility for a destabilization of the parallel orientation [11, 80, 139]. When the life time of the fluctuations is of the order of the characteristic time associated with the shear, the fluctuations interact with the shear. This interaction influences the amplitude of the fluctuations. Depending on their wave vector some fluctuations may be suppressed leading to a reduced Helfrich repulsion of the layers [80] or an additional excess area of the membranes [139], and, under appropriate conditions, to an undulation instability of the layers. In block copolymers the polymer conformation can be coupled to the applied shear stress using a free energy minimization [133] leading to a tilting of the molecules and a subsequent undulation instability. Close to the order-disorder transition (*i.e.*, in the weak segregation limit), also some theories investigate the behavior of the concentration field in an external shear field by the means of a Fokker-Planck equation [84] or a time dependent Ginzburg-Landau equation [15, 30].

In contrast to these mesoscopic approaches we search for an approach in the hydrodynamic macroscopic regime. This means, we investigate the stability on time scales long compared to the fluctuation time scale and on length scales large compared to any microscopic length scale. In other words, the more microscopic details used in the approaches mentioned above are averaged out in a macroscopic hydrodynamic approach.

## 1.5 Remark

This thesis is directly connected to the following publications, in which results of this doctoral work have been published or will be published.

- AUERNHAMMER, G. K., BRAND, H. R., AND PLEINER, H. *The undulation instability in layered systems under shear flow - a simple model*. Rheol. Acta **39** (2000), 215 – 222.
- AUERNHAMMER, G. K., BRAND, H. R., AND PLEINER, H. *Destabilization of a layered system by shear flow*. Proceedings of the Freiburger Arbeitstagung Flüssigkristalle **29** (2000), V19.
- AUERNHAMMER, G. K., BRAND, H. R., AND PLEINER, H. *Shear-induced instabilities in layered liquids*. Phys. Rev. E **66** (2002), 061707 (1 – 14).
- COLLIN, D., AUERNHAMMER, G. K., GAVAT, O., MARTINOTY, P., AND BRAND, H. R. *Frozen-in magnetic order in uniaxial magnetic gels: preparation and physical properties*. Macromol. Rapid Commun. (2003), in print.
- SODDEMANN, T., AUERNHAMMER, G. K., GUO, H., DÜNWEIG, B., AND KREMER, K. *Shear-induced buckling of smectic-A: MD simulations vs. analytic theory*. in preparation.



---

# Chapter 2

## Motivation and basic idea<sup>1</sup>

### 2.1 A theorist's view

The experimental similarities between systems of different molecular constituents indicate that the theoretical description of these reorientations can be constructed—at least to a large extent—from a common generic basis. A description including specific differences must refer closer to the microscopic details.

In this work we want to develop a hydrodynamic approach to these reorientation phenomena. Consequently, we assume that all internal microscopic time scales are short compared to the times we are interested in and all microscopic lengths are small compared to the lengths the theory is applied to. Especially, the resulting description is only valid when the externally imposed time and length scales (due to the shear rate and the system size) are large compared to the microscopic scales (*e.g.*, the life time of layer fluctuations and the repeat distance of the layering).

The well established standard hydrodynamic description of smectic-*A* liquid crystals (see, *e.g.*, Refs. [25, 26, 81, 104] and Sec. 1.3) is a good macroscopic starting point for such a theoretical approach.

In the present work we approximate the experiments described in Sec. 1.2 in the following way. The sample is placed between two laterally infinite, parallel plates (see Fig. 2.1). The upper plate (located at  $z = d/2$ ) moves with a constant velocity  $\vec{v}_u = d\dot{\gamma}\hat{e}_x/2$  to the right and the lower plate (at  $z = -d/2$ ) moves with the same velocity in the opposite direction ( $\vec{v}_l = -d\dot{\gamma}\hat{e}_x/2$ ). Thus the sample is submitted to an average shear given by  $|\vec{v}_u - \vec{v}_l|/d = \dot{\gamma}$ , with the  $x$  direction as the flow direction and the  $y$  axis parallel to the neutral (or vorticity) direction of the flow.

Placing a layered liquid in such a shear cell, the three basic orientations shown in Fig. 2.2 are possible spatially homogeneously, but only the parallel and perpendicular orientations can be stable under steady shear conditions. If we allow for spatially inhomogeneous

---

<sup>1</sup>Chapters 2 to 4 are based on Refs. [2, 3, 4]

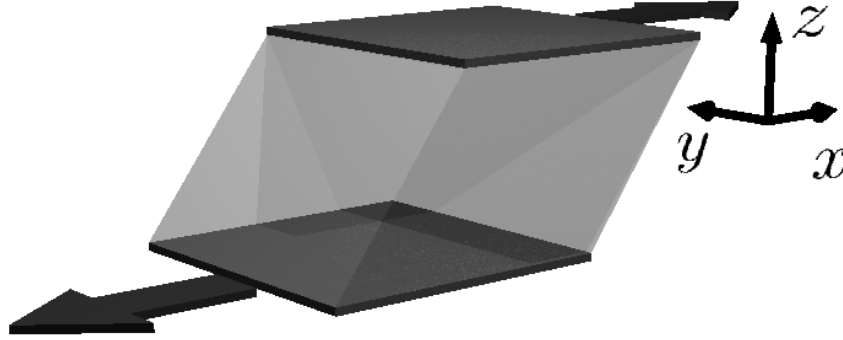


**Figure 2.1:** At the level of our approximations all shear geometries can be considered to be represented by a laterally infinite layer with the upper plate moving to the right and the lower plate moving to the left.

configurations, also other more complex situations are possible, see, *e.g.*, Chapter 6. The experiments described in Sec. 1.2 suggest that a well ordered parallel orientation is stable at low shear rates and unstable above a certain (critical) shear rate.

## 2.2 Motivation for the present approach

Let us start our theoretical considerations by the consideration of a standard smectic-*A* liquid crystal under steady shear. In the standard description the macroscopic hydrodynamic equations for an incompressible smectic-*A* liquid crystal read (see, *e.g.*, [26, 75] and Sec. 3.1):

$$\frac{\partial}{\partial t}u + v_j \nabla_j u = p_i v_i - \lambda_p \Psi, \quad (2.1)$$

$$\rho \left( \frac{\partial}{\partial t}v_i + v_j \nabla_j v_i \right) = p_i \nabla_j \psi_j + \nabla_j (\nu_{ijkl} \nabla_l v_k) - \nabla_i P, \quad (2.2)$$

$$\nabla_i v_i = 0, \quad (2.3)$$

with the velocity field  $\vec{v}$ , the thermodynamic force connected with  $u$ ,  $\Psi = -\nabla_i \psi_i = (\delta\epsilon)/(\delta u)$ , the pressure  $P$  and the viscosity tensor  $\nu_{ijkl}$ . The spatially homogeneous solution follows immediately. The system will show a linear shear profile and an unperturbed smectic layering (for both parallel and perpendicular orientation of the layers).

In a sample with parallel alignment the apparent viscosity is  $\nu_3$ , which can easily be seen from the force on the upper boundary,

$$\vec{F}_{\parallel} = \hat{e}_z \cdot \underline{\sigma} = \dot{\gamma} \nu_3 \hat{e}_x, \quad (2.4)$$

or the dissipation function

$$R = \nu_{ijkl} (\nabla_j v_i) (\nabla_l v_k) = \nu_3 \dot{\gamma}^2, \quad (2.5)$$



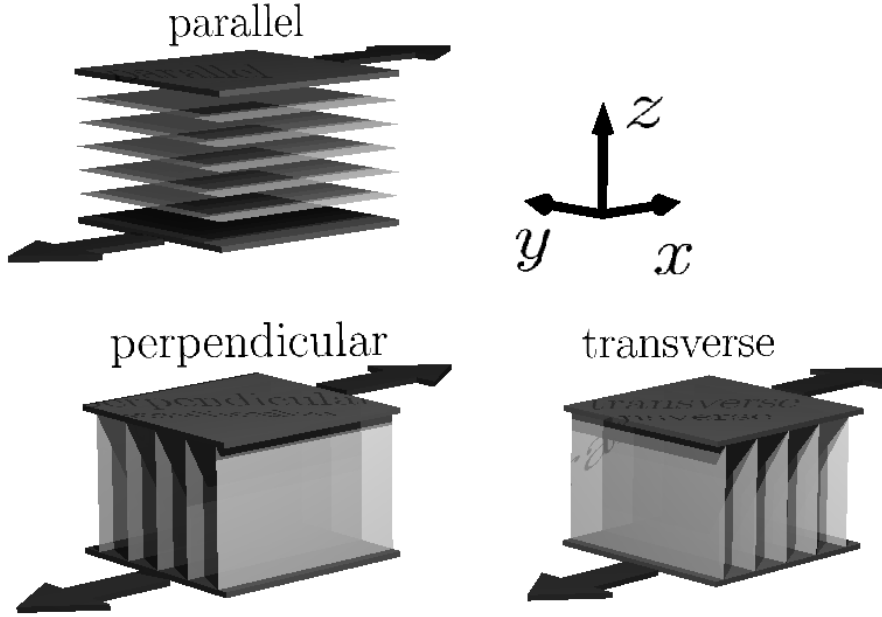


**Figure 2.2:** Three basic spatially homogeneous orientations of a layered liquid in a shear cell are possible. Note that only parallel and perpendicular orientation are found to be stable under steady shear conditions.

where  $\dot{\gamma}$  is the shear rate,  $\underline{\sigma}$  the stress tensor, and  $\nu_{ijkl}$  the viscosity tensor for a uniaxial system with the layer normal as preferred direction.<sup>2</sup> Similarly, the viscosity of a perpendicular alignment is given by  $\nu_2$ ,

$$\vec{F}_\perp = \hat{e}_z \cdot \underline{\sigma} = \dot{\gamma} \nu_2 \hat{e}_x, \quad (2.6)$$

and

$$R = \nu_{ijkl} (\nabla_j v_i) (\nabla_l v_k) = \nu_2 \dot{\gamma}^2. \quad (2.7)$$

For  $\nu_2 < \nu_3$  a simple shear flow in a perpendicular alignment causes less dissipation than in a parallel alignment. The next step is to study the stability of these alignments in the linear regime. Using the results of Oswald and Ben-Abraham [100] we can assume that the first instability will exhibit a wave vector along the neutral direction of the flow. Following the standard procedure (see Technical Note 2.1 on page 18) we find a solvability condition of the linearized equations which does not depend on the shear rate  $\dot{\gamma}$ ,

$$0 = \left\{ q^2 + \lambda_p \left[ \nu_3 (q^2 - q_z^2)^2 + 2(\nu_2 + \nu_3) q^2 q_z^2 \right] \right\} \times \\ \times (B_0 q_z^2 + K q^4) (\nu_2 q^2 + \nu_3 q_z^2), \quad (2.8)$$

<sup>2</sup>These quantities will be discussed in Chapter 3 in more detail.

**Technical Note 2.1** Linear stability analysis

Given a differential operator  $D$  (here of the type of the Navier-Stokes equations, *i.e.*, only first time derivatives but higher spatial derivatives) which acts on a set of variables  $\vec{X}$  and has a spatially homogeneous solution  $\vec{X}_0$  ( $D\vec{X}_0 = 0$ ), one can determine the region of (linear) stability of  $\vec{X}_0$  by performing a linear stability analysis. That is, one adds a small perturbation  $\vec{X}_1$  to the homogeneous solutions  $\vec{X}_0$ :  $\vec{X} = \vec{X}_0 + \vec{X}_1$  (with  $\vec{X}_1 \ll \vec{X}_0$ ) and linearizes the governing equations in the small perturbations ( $D\vec{X} = \frac{\partial}{\partial t}\vec{X}_1 + L\vec{X}_1 + \text{h.o.t.}$ ).  $\vec{X}_0$  is stable if the growth rate for all possible modes in  $\vec{X}_1$  is negative. If (for a given set of external parameters) one mode in  $\vec{X}_1$  has a positive growth rate, this mode will grow and  $\vec{X}_0$  will be unstable. In case only one mode is unstable, it is called the critical mode and the corresponding parameters are the critical parameters. In many cases it suffices to analyze the solvability conditions of  $L\vec{X}_1 = 0$ , *i.e.*, to look for zero growth rate under the assumption of a purely exponential time dependence.

We note that this analysis is only suitable to determine the onset of an instability and its most unstable mode, but does not allow to predict the structure, which will develop above threshold.

with the permeation constant  $\lambda_p$ . Consequently, a parallel alignment of smectic layers is linearly stable against undulations, even if the perpendicular alignment might be more preferable due to some thermodynamic considerations. This means that standard smectic-*A* hydrodynamics does not suffice to explain the observed reorientation phenomena. This is the main reason for the present approach, in which we show that some simple additional ingredients give an easy way to explain the destabilization of the parallel orientation by shear flow. In the following section we will develop the basic idea of our approach and fill in the details in Chapter 3.

## 2.3 Physical idea of the model – induced biaxiality in smectic-*A*

As we have seen above, standard smectic-*A* hydrodynamics does not suffice to explain the destabilization of the parallel orientation. Now we want to go beyond the standard description and show that a few changes lead directly to the observed instability.

A gedanken-experiment illustrates the basis idea. The standard view of smectic-*A* liquid crystals, as used in Sec. 1.3, includes only the smectic layering; the notions director and layer normal are equivalent in this description. But equivalently, one can say that a smectic-*A* liquid crystal consists of a nematic liquid crystal showing, additionally, a strong positional order along the director. This means that two continuous symmetries are broken in order to transform an isotropic liquid into a smectic-*A* liquid crystal. The equivalence of all directions is reduced to a uniaxial order and translational symmetry is broken along this symmetry axis. In the standard description the identity of both preferred axes is also assumed in non-equilibrium situations. This restricts the dynamic

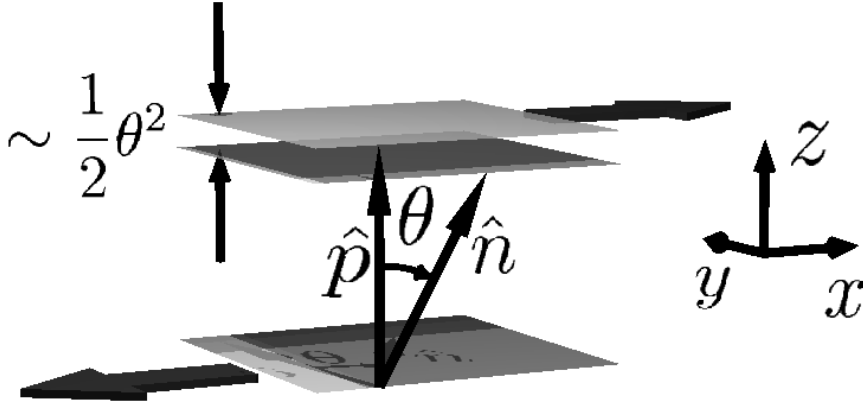


**Figure 2.3:** A finite angle  $\theta$  between  $\hat{n}$  and  $\hat{p}$  leads to a tendency of the layers to reduce their thickness. Supposing a constant number of layers in the sample, this tendency is equivalent to an effective *dilation* of the layers. For small angles between  $\hat{n}$  and  $\hat{p}$  the relative effective dilation is given by  $\theta^2/2$ .

behavior of the associated variables,<sup>3</sup> the system is fully described using only the layering. We now drop this strict assumption and allow both axes to enclose a finite (but usually small) angle in non-equilibrium situation. In thermal equilibrium, an energetic coupling ensures that both axes are parallel. Both variables differ significantly in their interaction with external fields (*e.g.*, shear or magnetic fields).

A three-dimensional stack of parallel fluid layers cannot couple directly to an applied shear flow. Neither does the layer normal: It stays unchanged as long as the flow direction lies within the layers. In contrast, it is well known from nematic hydrodynamics that the director  $\hat{n}$  experiences a torque in a shear flow. This torque leads—in the simplest case—to a flow aligning behavior of the director.

Submitted to a shear flow, the layer normal  $\hat{p}$  will stay unchanged, but the torque on the director  $\hat{n}$  due to the shear will be balanced by a torque arising from the coupling between  $\hat{n}$  and the layer normal  $\hat{p}$ . For any given shear rate, the equilibrium between these two torques will result in a finite, but usually small, angle  $\theta$  between  $\hat{n}$  and  $\hat{p}$ . Roughly speaking, we have a shear-induced smectic-*C*-like situation.<sup>4</sup> This finite angle has important consequences for the layers. Since the preferred thickness of the layers is proportional to the projection of the director on the layer normal, a finite angle between those two directions reduces the preferred layer thickness and, thus, is equivalent to an effective dilation of approximately  $\theta^2/2$  (see Fig. 2.3). If we assume a constant total sample thickness and exclude effects of defects, the system can accommodate this constraint by layer rotations. A global rotation of the layers is not possible for topological

<sup>3</sup>As discussed in the introduction, the broken rotational symmetry is associated with a director variable and the translational ordering is connected to a layer displacement variable.

<sup>4</sup>Note that this is *not* a phase transition, because the angle is only non-zero in non-equilibrium situations.

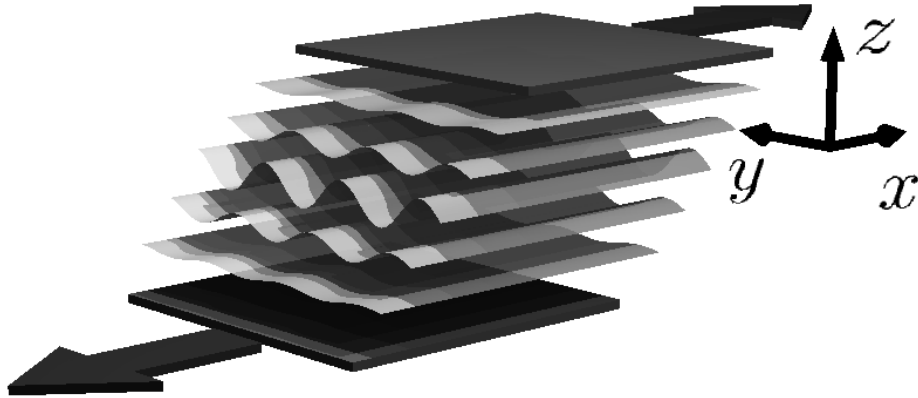


**Figure 2.4:** Above a certain threshold the effective dilation due to the director tilt will lead to undulations of the layers. Note the difference in directions: The director is tilted in the flow direction, whereas the wave vector of the undulations points along the  $y$  axis. In this configuration, there is no direct coupling between the flow and the undulations.

reasons, but they can rotate locally (as in the case of dilated smectic- $A$  liquid crystals [16, 28], see also Sec. 1.3). This local rotation of the layers leads to undulations, as shown in Fig. 2.4.

These undulations are a compromise between the uniform effective dilation (which is not favorable for the system) and the curvature of the layers due to the undulations (which costs bending energy). In the static case of dilated smectic- $A$  liquid crystals the wave vector of the undulations has no preferred direction, but this symmetry is broken if an additional shear is applied to the system. To illustrate this, the following picture might be helpful. As the interlayer diffusion is typically very small, the layers “glide” over each other like two sheets of paper. When the undulation instability sets in, the layers are more like two sheets of rippled paper. Everyday experience tells us that these sheets glide easily over one another, only if the undulation wave vector is along the neutral direction of the “shear”. More rigorously, a superposition of steady shear and dilation has been studied by Oswald and Ben-Abraham within the framework of standard smectic- $A$  hydrodynamics [100]. For this case they predict that the wave vector of the undulations will point along the neutral direction of the shear. As depicted in Fig. 2.4, we will assume that these symmetry considerations hold for our extended version of smectic- $A$  hydrodynamics as well.

## Remarks

- The mechanism we have proposed here is somewhat similar to a shear induced smectic- $C$ -like situation. Consequently, undulations should also be observed in smectic- $A$ –smectic- $C$  transitions. Indeed Johnson and Saupe [58], and later Kumar [63], reported such undulations just below the transition temperature.

- Ribotta and Durand studied the mechanical properties of smectic-*A* and smectic-*C* phases [111] and reported that compression on a smectic-*A* phase can induce a smectic-*C*-like orientation.
- Biaxial nematics also have two preferred directions. If the biaxiality of the nematic phase is due to a biaxial structure of the microscopic units (*e.g.*, molecules or vesicles) the two preferred directions enclose a fixed angle. Alternatively, it is also possible that the macroscopic biaxiality is based on a mixture of two uniaxial components (*e.g.*, disc-like and rod-like aggregates), with different symmetry axes. Pleiner and Brand [103] showed that in the latter case external fields can influence the angle between the two principal axes. This effect is somewhat similar to the induced biaxiality that is discussed in the present work.
- The only external field we considered in this chapter was a shear field. But, as we will show later, also other external fields (*e.g.*, magnetic or electric) can induce a biaxiality in smectic-*A* liquid crystals. In more complex materials, like liquid crystalline elastomers, the coupling between the deformation of the polymer network and the liquid crystalline order also leads to an induced biaxiality (see Sec. 4.2 for more details).



---

# Chapter 3

## Including the director in smectic- $A$ hydrodynamics<sup>1</sup>

### 3.1 Macroscopic hydrodynamic equations

The derivation of the macroscopic hydrodynamic equations for our system is based on irreversible thermodynamics and symmetry arguments. This method has successfully been applied in many cases to derive the macroscopic hydrodynamic equations of complex fluids (see, *e.g.*, Refs. [3, 4, 60, 75, 81, 104]). The advantage of this method is its systematic way of deducing the governing equations. Once the set of variables is given, the macroscopic hydrodynamic equations follow by applying basic symmetry arguments and thermodynamic considerations.

Let us briefly review the essential ingredients to this procedure (for more details of the method, see Ref. [104]). For a given system the macroscopic variables can be split up in three categories. i) Conservation laws lead to the following hydrodynamics variables: mass density ( $\rho$ ), linear momentum density ( $\vec{g}$ ), and energy density ( $\epsilon$ ). ii) Spontaneously broken continuous symmetries generate additional hydrodynamic variables like the nematic director  $\hat{n}$  or the layer displacement  $u$  in a smectic- $A$  phase<sup>2</sup>. iii) In some cases, non-hydrodynamic variables can show slow dynamics that can be described within this framework (*e.g.*, the strength of the order parameter [9, 75, 104]).

Using these variables, the relations, which form the starting point for the further calculations, can be constructed. These relations are: the energy density  $\epsilon$ , the dissipation function  $R$ , the Gibbs relation (as the local formulation of the second law of thermodynamics), and the Gibbs-Duhem relation (which follows from the Euler relation for homogeneous functions). To illustrate the idea of our model, we split up  $\epsilon$  and  $R$  into several parts according to the different origin of the variables:

---

<sup>1</sup>Chapters 2 to 4 are based on Refs. [2, 3, 4]

<sup>2</sup>Note that  $u$  is only the appropriate macroscopic variable as long as the smectic layers are not strongly deformed. In the case of strong deformations one must take the phase  $\varphi$  as a macroscopic variable, see *e.g.*, Ref.[79, 105].

- i) conserved quantities (index *cons*)
- ii) symmetry variables (index *sym*)
- iii) the strength of the order parameter (index *ord*)

In the spirit of our model, two order parameters have to be considered: the nematic tensorial order parameter  $Q_{ij}$  and the smectic- $A$  complex order parameter  $\Phi$ . For practical reasons we use the director  $\hat{n}$  and the modulus  $S^{(n)}$  in the uniaxial nematic case [ $Q_{ij} = \frac{3}{2}S^{(n)}(n_i n_j - \frac{1}{3}\delta_{ij})$ ] and the layer displacement  $u$  and the modulus  $S^{(s)}$  in the smectic- $A$  case [ $\Phi = S^{(s)} \exp\{iq_0(z - u)\}$ ], supposing a parallel orientation of the layers, as shown in Fig. 2.2]. For practical purposes it is useful to introduce the layer normal  $\hat{p}$ , which is connected to  $u$  via

$$\hat{p} = \frac{\nabla(z - u)}{|\nabla(z - u)|}. \quad (3.1)$$

In our further discussion, we will concentrate on the parts due to symmetry variables and the order parameters, while for terms already present in the isotropic fluid see, *e.g.*, Refs. [27, 104]. The notation introduced in the following equations is summarized in Table 3.1.

The energy density is split into four parts

$$\epsilon = \epsilon_{cons} + \epsilon_{sym} + \epsilon_{ord}^{(n)} + \epsilon_{ord}^{(s)}, \quad (3.2)$$

where  $\epsilon_{cons}$  is identical to the simple fluids' case and is discussed elsewhere [104]. The energy density is a good scalar, *i.e.*, it is even under time reversal and parity transformations and invariant under rigid rotations and translations of the whole systems. Since thermal equilibrium is the state of minimal energy, we construct our energy density as a bilinear form in the quantities which characterize the departure from this state. In gradient expansions we will only take into account the lowest non-trivial order. The nematic director does not distinguish between head and tail and, therefore, can only enter the energy density in even powers. Rotational invariance forbids terms proportional to  $\hat{n}$ , so the first term in a gradient expansion of  $\epsilon_{sym}$  is of the type  $1/2 K_{ijkl} \nabla_i n_j \nabla_k n_l$ , where  $K_{ijkl}$  is to be expanded in the irreducible fourth rank tensors for a uniaxial system. The layer displacement  $u$  changes sign under parity, so the terms including  $u$  have to be constructed such that they are even under parity. A homogeneous change of  $u$  is equivalent to a translation of the system and first transverse gradients rotate the whole system. Accordingly, the lowest order gradients which enter the energy density are  $1/2 K(\nabla_{\perp}^2 u)^2 + 1/2 B_0(\nabla_{\parallel} u)^2$ , where  $\nabla_{\perp}$  and  $\nabla_{\parallel}$  denotes the gradients perpendicular and parallel to the layer normal, respectively. Terms reflecting rotations of the whole system are forbidden in the energy density, but relative rotations of the director against the layers are allowed.<sup>3</sup> The lowest order term of these relative rotations will be proportional to the square of the angle between the director  $\hat{n}$  and the layer normal

---

<sup>3</sup>In our case this relative rotation is a slowly relaxing, non-hydrodynamic variable.



Symbol	Explicit form	Comment
$K$	$K$	Bending modulus of layers
$B_0$	$B_0$	Compressibility of layers
$B_1$	$B_1$	Coupling between the director and the layer normal
$L_0^{(n)}, L_0^{(s)}$	$L_0^{(n)}, L_0^{(s)}$	Variations of the order parameter (nematic and smectic, respectively)
$L_{1,ij}^{(n)}$	$L_{\perp}^{(n)} \delta_{ij}^{\perp} + L_{\parallel}^{(n)} n_i n_j$	Gradient terms of the order parameter (nematic)
$M_{ijk}$	$M_0(\delta_{ij}^{\perp} n_k + \delta_{ik}^{\perp} n_j)$	Cross coupling between the director and order parameter (nematic)
$L_{1,ij}^{(s)}$	$L_{\perp}^{(s)}(\delta_{ij} - p_i p_j) + L_{\parallel}^{(s)} p_i p_j$	Gradient terms of the order parameter (smectic)

**Table 3.1:** Summary of the notation. In these definitions we use the transverse Kronecker symbol  $\delta_{ij}^{\perp} = \delta_{ij} - n_i n_j$ . Due to the thermodynamic stability of the systems, the following constants and combinations of constants must be positive:  $B_0, B_1, K, L_0^{(n)}, L_0^{(s)}, L_{\perp}^{(n)}, L_{\perp}^{(s)}, L_{\parallel}^{(n)}, L_{\parallel}^{(s)}$ , and  $KL_{\parallel}^{(n)} - M_0^2$ . For the last relation we used the equivalence of  $K$  and  $K_1$ .

$\hat{p}$ ,  $1/2 B_1(\hat{n} \times \hat{p})^2$ . Note that this term will lead to a relaxing behavior and not to a hydrodynamic  $\omega(k \rightarrow 0) = 0$  one. Following these arguments the symmetry part reads,

$$\begin{aligned}
 \epsilon_{sym} = & \frac{1}{2} K_1 (\nabla \cdot \hat{n})^2 + \frac{1}{2} K_2 [\hat{n} \cdot (\nabla \times \hat{n})]^2 \\
 & + \frac{1}{2} K_3 [\hat{n} \times (\nabla \times \hat{n})]^2 \\
 & + \frac{1}{2} K (\nabla_{\perp}^2 u)^2 + \frac{1}{2} B_0 (\nabla_{\parallel} u)^2 \\
 & + \frac{1}{2} B_1 (\hat{n} \times \hat{p})^2.
 \end{aligned} \tag{3.3}$$

In the spirit of our model, we combine here the properties of a nematic liquid crystal (the first two lines) with these of a smectic-*A* liquid crystal (the third line) and couple both parts (the last line) in such a way that  $\hat{n}$  and  $\hat{p}$  are parallel in equilibrium.  $\epsilon_{sym}$  simplifies considerably by dropping higher-order terms and assuming a small angle between  $\hat{n}$  and  $\hat{p}$ . Splay deformations of the director are generally considered as higher-order corrections to dilations of the smectic layers. Twist deformations are forbidden in standard smectic-*A* hydrodynamics and must be small as long as the angle between  $\hat{n}$  and  $\hat{p}$  is small. In the

same way, the difference between the splay deformation of the director field  $K_1/2 (\nabla \cdot \hat{n})^2$  and bending of the layers  $K/2 (\nabla_{\perp}^2 u)^2$  is negligible, if  $\hat{n}$  is close to  $\hat{p}$ . Consequently, we combine splay deformations of the director and bending of the layers in a single term with a single elastic constant which we call for a moment  $K'$ :  $K_1/2 (\nabla \cdot \hat{n})^2 + K/2 (\nabla_{\perp}^2 u)^2 \approx K'/2 (\nabla_{\perp}^2 u)^2$ . Further on, we drop the prime and call the new elastic constant  $K$ . According to the discussion in Sec. 2.3 the dilation of the layers is modified by two additional effects. First the effective dilation  $(1 - \hat{n} \cdot \hat{p})$  has to be taken into account. And second, we have to expand  $\nabla_{\parallel}$  in gradients along the coordinate axes. In our geometry this leads, in lowest non-trivial order, to the replacement  $\nabla_{\parallel} u \rightarrow \nabla_z u - 1/2(\nabla_{\perp} u)^2$ . Using these approximations  $\epsilon_{sym}$  is given by

$$\begin{aligned} \epsilon_{sym} &= \frac{1}{2}K (\nabla_{\perp}^2 u)^2 \\ &+ \frac{1}{2}B_0 \left[ \nabla_z u + (1 - n_z) - \frac{1}{2} (\nabla_{\perp} u)^2 \right]^2 \\ &+ \frac{1}{2}B_1 (\hat{n} \times \hat{p})^2. \end{aligned} \quad (3.4)$$

In our model the moduli of the nematic and smectic order parameters play similar roles, so we will deal with both. Since we consider a situation beyond the phase transition regime, the equilibrium values of the order parameter are nonzero ( $S_0^{(n)}$  and  $S_0^{(s)}$ ) and only their variations  $s^{(n)}$  and  $s^{(s)}$  can enter the energy density ( $S^{(n)} = S_0^{(n)} + s^{(n)}$  and  $S^{(s)} = S_0^{(s)} + s^{(s)}$ ),

$$\begin{aligned} \epsilon_{ord}^{(n)} &= \frac{1}{2}L_0^{(n)} (s^{(n)})^2 + \frac{1}{2}L_{1,ij}^{(n)} (\nabla_i s^{(n)}) (\nabla_j s^{(n)}) \\ &+ M_{ijk} (\nabla_j n_i) (\nabla_k s^{(n)}), \end{aligned} \quad (3.5)$$

$$\epsilon_{ord}^{(s)} = \frac{1}{2}L_0^{(s)} (s^{(s)})^2 + \frac{1}{2}L_{1,ij}^{(s)} (\nabla_i s^{(s)}) (\nabla_j s^{(s)}). \quad (3.6)$$

We note that an additional term of the type  $N_{ijkl}Q_{ij}(\nabla_k \Phi)(\nabla_l \Phi^*)$ , coupling the two order parameters, is also possible. We will neglect this term in the following, because it is of third order, one order higher than the other terms in the energy density. Due to the thermodynamic stability of the system the energy density must be of positive definite form. To fulfill this condition, the following material parameters and combinations of material parameters must be positive:<sup>4</sup>  $B_0$ ,  $B_1$ ,  $K$ ,  $L_0^{(n)}$ ,  $L_0^{(s)}$ ,  $L_{\perp}^{(n)}$ ,  $L_{\perp}^{(s)}$ ,  $L_{\parallel}^{(n)}$ ,  $L_{\parallel}^{(s)}$ , and  $KL_{\parallel}^{(n)} - M_0^2$ .

Phenomenologically, the dissipation function can be written as a (Galilei invariant) positive definite quadratic form of the thermodynamic forces (see Table 3.2 for a summary of these forces).<sup>5</sup> Similar to the energy density, we split the dissipation function into

<sup>4</sup>For the last relation we used the equivalence of  $K$  and  $K_1$ .

<sup>5</sup>Since  $R$  is Galilei invariant and zero in thermal equilibrium, only gradients of the velocity  $\vec{v}$  (which is the thermodynamic conjugate to the linear momentum density  $\vec{g}$ ) enter. By similar arguments one can show that the thermodynamic conjugates to the other conserved quantities also enter  $R$  only *via* gradients (see, *e.g.*, Ref. [27]). There is no such restriction for symmetry variables.

Name	Variable	Conjugate
Mass density	$\rho$	$\mu$
Momentum density	$\vec{g}$	$\vec{v}$
Nematic director	$\hat{n}$	$\vec{h}$
Smectic layer displacement	$u$	$\Psi$
Variation of the modulus of the order parameter (either nematic or smectic)	$s^{(n)}, s^{(s)}$	$\Xi^{(n)}, \Xi^{(s)}$

**Table 3.2:** Variables and their conjugates, *i.e.*, the corresponding thermodynamic forces.

three parts.

$$R = R_{cons} + R_{sym} + R_{ord}, \quad (3.7)$$

$$R_{cons} = \frac{1}{2} \nu_{ijkl} (\nabla_j v_i) (\nabla_l v_k) + R_0, \quad (3.8)$$

$$R_{sym} = \frac{1}{2\gamma_1} h_i \delta_{ij}^\perp h_j + \frac{\lambda_p}{2} \Psi^2, \quad (3.9)$$

$$R_{ord} = \frac{1}{2} \alpha^{(n)} \Xi^{(n)2} + \frac{1}{2} \alpha^{(s)} \Xi^{(s)2}, \quad (3.10)$$

where  $R_0$  summarizes further terms also present in simple fluids (*e.g.*, thermal diffusion), which do not enter our further calculation, and (after Ref. [37])

$$\begin{aligned} \nu_{ijkl} = & \nu_2 (\delta_{jl} \delta_{ik} + \delta_{il} \delta_{jk}) \\ & + 2(\nu_1 + \nu_2 - 2\nu_3) n_i n_j n_k n_l \\ & + (\nu_3 - \nu_2) (n_j n_l \delta_{ik} + n_j n_k \delta_{il} \\ & \quad + n_i n_k \delta_{jl} + n_i n_l \delta_{jk}) \\ & + (\nu_4 - \nu_2) \delta_{ij} \delta_{kl} \\ & + (\nu_5 - \nu_4 + \nu_2) (\delta_{ij} n_k n_l + \delta_{kl} n_i n_j). \end{aligned} \quad (3.11)$$

The positivity of  $R$  requires the following parameters and combinations of parameters to be positive (see, *e.g.*, [37]):  $\gamma_1$ ,  $\lambda_p$ ,  $\alpha^{(n)}$ ,  $\alpha^{(s)}$ ,  $\nu_2$ ,  $\nu_3$ ,  $\nu_4$ ,  $2(\nu_1 + \nu_5) - \nu_4 + \nu_2$ , and  $\nu_4(2\nu_1 + \nu_2) - (\nu_5 - \nu_4)^2$ . As mentioned in Sec. 2.3 we consider a shear induced smectic- $C$ -like situation (but with a small tilt angle, *i.e.*, a weak biaxiality). We neglect this weak biaxiality in the viscosity tensor and use it in the uniaxial formulation given above (with the director  $\hat{n}$  as the preferred direction). This assumption is justified by the fact that the results presented in this work do not change significantly if we use  $\hat{p}$  instead of  $\hat{n}$  in the viscosity tensor.

Throughout our calculations, we will not assume any restriction on the viscosity constants except the usual requirements due to thermodynamic stability (see above). Later

on, we will impose the incompressibility of the fluid by assuming a constant mass density  $\rho$  of the fluid.

The set of basic equations is completed by the Gibbs-Duhem relation (the local formulation of the first law of thermodynamics) and the Gibbs relation (which follows from the Euler theorem for homogeneous functions and connects the pressure  $P$  with the other thermodynamic quantities). In our notation, these relations take the form:

$$\begin{aligned} d\epsilon &= d\epsilon_{cons} + d\epsilon_{sym} + d\epsilon_{ord}^{(n)} + d\epsilon_{ord}^{(s)} \\ &= d\epsilon_0 + \vec{v} \cdot d\vec{g} + \varphi_{ij} d\nabla_j n_i + h'_i dn_i + \psi_i d\nabla_i u \\ &\quad + \Xi'^{(n)} ds^{(n)} + \Xi''^{(n)} d\nabla_i s^{(n)} \\ &\quad + \Xi'^{(s)} ds^{(s)} + \Xi''^{(s)} d\nabla_i s^{(s)}, \end{aligned} \quad (3.12)$$

$$P = -\epsilon + \mu\rho + T\sigma + \vec{v} \cdot \vec{g}. \quad (3.13)$$

The newly defined quantities in Eq. (3.12) are connected by

$$h_i = h'_i - \nabla_j \varphi_{ij} = \frac{\delta\epsilon}{\delta n_i}, \quad (3.14)$$

$$\Psi = -\nabla_i \psi_i = \frac{\delta\epsilon}{\delta u}, \quad (3.15)$$

$$\Xi^{(n)} = \Xi'^{(n)} - \nabla_i \Xi''^{(n)} = \frac{\delta\epsilon}{\delta s^{(n)}}, \quad (3.16)$$

$$\Xi^{(s)} = \Xi'^{(s)} - \nabla_i \Xi''^{(s)} = \frac{\delta\epsilon}{\delta s^{(s)}} \quad (3.17)$$

to the thermodynamic forces (Table 3.2)

For variables which arise from conservation laws, these laws lead directly to the balance equations:

$$\frac{\partial}{\partial t} \rho + \nabla_i (v_i \rho) = 0 \quad (3.18)$$

$$\frac{\partial}{\partial t} g_i + \nabla_j (v_j g_i) + \nabla_j \sigma_{ij} = 0 \quad (3.19)$$

$$\frac{\partial}{\partial t} \epsilon + \nabla_i [v_i (\epsilon + p)] + \nabla_i j_i^\epsilon = 0 \quad (3.20)$$

$\sigma_{ij}$  denotes the stress tensor and  $j_i^\epsilon$  the energy current. Similar balance equations are valid for the other variables (associated with broken symmetries and the entropy density).

$$\frac{\partial}{\partial t} \sigma + \nabla_i (v_i \sigma) + \nabla_i j_i^\sigma = \frac{R}{T} \quad (3.21)$$

$$\frac{\partial}{\partial t} n_i + v_j \nabla_j n_i + Y_i = 0 \quad (3.22)$$

$$\frac{\partial}{\partial t} u + v_j \nabla_j u + Z = 0 \quad (3.23)$$

$$\frac{\partial}{\partial t} s^{(n)} + v_i \nabla_i s^{(n)} + X^{(n)} = 0 \quad (3.24)$$

$$\frac{\partial}{\partial t} s^{(s)} + v_i \nabla_i s^{(s)} + X^{(s)} = 0 \quad (3.25)$$

In Eqs. (3.21) to (3.25)  $\sigma$  is the entropy density,  $T$  the temperature and  $j_i^\sigma$ ,  $Y_i$ ,  $Z$ ,  $X_i^{(n)}$ , and  $X_i^{(s)}$  are the (quasi-) currents associated with  $\sigma$ ,  $n_i$ ,  $u$ ,  $s^{(n)}$ , and  $s^{(s)}$ , respectively. Note that either the entropy density or the energy density is a dependent variable and one of them can be eliminated using the Gibbs relation.

In all balance equations we split the currents and quasi-currents into two parts: a reversible and an irreversible one. By construction, the entropy production for the reversible parts is zero and only the dissipative currents cause  $R \neq 0$ . The reversible currents must show the same behavior under time reversal and parity as the time derivative of the variables and guarantee the invariance of the dynamic equations under Galilei transformations and rigid rotations. Note that the convective derivatives are also part of the reversible currents and have been set apart only for convenience. Inserting the balance equations into the Gibbs relation allows to determine the condition which the reversible currents and quasi-currents must fulfill. The exact structure of these can be determined by the above symmetry requirement (see, *e.g.*, the Technical Note 3.1 or Ref.[104]). The dissipative currents are given as partial derivatives of the (phenomenological) dissipation function  $R$ . In all currents and quasi-currents symmetry considerations including rotational and translational invariance reduce the number of phenomenological constants further. If we assume incompressibility, the balance equations read:

$$\frac{\partial}{\partial t} u + v_j \nabla_j u = v_z - \lambda_p \Psi, \quad (3.26)$$

$$\begin{aligned} \frac{\partial}{\partial t} n_i + v_j \nabla_j n_i &= \frac{1}{2} [(\lambda - 1) \delta_{ij}^\perp n_k + (\lambda + 1) \delta_{ik}^\perp n_j] \nabla_j v_k \\ &\quad - \frac{1}{\gamma_1} \delta_{ik}^\perp h_k, \end{aligned} \quad (3.27)$$

$$\nabla_i v_i = 0, \quad (3.28)$$

$$\begin{aligned} \rho \left( \frac{\partial}{\partial t} v_i + v_j \nabla_j v_i \right) &= - \nabla_j \left\{ \delta_{ij} P + \psi_j (\nabla_i u - \delta_{iz}) + \beta_{ij}^{(n)} \Xi^{(n)} + \beta_{ij}^{(s)} \Xi^{(s)} \right. \\ &\quad \left. - \frac{1}{2} [(\lambda - 1) \delta_{jk}^\perp n_i + (\lambda + 1) \delta_{ik}^\perp n_j] h_k \right\} \\ &\quad + \nabla_j (\nu_{ijkl} \nabla_l v_k), \end{aligned} \quad (3.29)$$

$$\frac{\partial}{\partial t} s^{(n)} + v_j \nabla_j s^{(n)} = - \beta_{ij}^{(n)} \nabla_j v_i - \alpha^{(n)} \Xi^{(n)}, \quad (3.30)$$

$$\frac{\partial}{\partial t} s^{(s)} + v_j \nabla_j s^{(s)} = - \beta_{ij}^{(s)} \nabla_j v_i - \alpha^{(s)} \Xi^{(s)}. \quad (3.31)$$

For the reversible parts of the equations some coupling constants have been introduced. Due to rotational invariance, the flow-alignment tensor takes the form

$$\lambda_{ijk} = \frac{1}{2} [(\lambda - 1) \delta_{ij}^\perp n_k + (\lambda + 1) \delta_{ik}^\perp n_j], \quad (3.32)$$

with the flow-alignment parameter  $\lambda$  (and using  $\delta_{ij}^\perp = \delta_{ij} - n_i n_j$ ) and the coupling

**Technical Note 3.1** Reversible currents

After inserting the balance equations in the Gibbs relation, we find that the reversible parts of the (quasi-) currents (denoted with the upper index  $R$ ) have to fulfill the condition

$$\begin{aligned} \nabla_j \left[ j_j^{\epsilon R} + p v_j - v_i \sigma_{ij}^R - \varphi_{ij} Y_i^R - \Xi_j^{(n)} X^{(n)R} - \Xi_j^{(s)} X^{(s)R} \right] \\ = -\sigma_{ji}'' \nabla_i v_j + h_i Y_i^R + \Xi^{(n)} X^{(n)R} + \Xi^{(s)} X^{(s)R} + \psi_i \nabla_i Z^R, \end{aligned}$$

where we used the definitions

$$\begin{aligned} h_i &= h_i' - \nabla_j \varphi_{ij} = \frac{\delta \epsilon}{\delta n_i}, \\ \Xi^{(n)} &= \Xi'^{(n)} - \nabla_i \Xi_i''^{(n)} = \frac{\delta \epsilon}{\delta s^{(n)}}, \\ \Xi^{(s)} &= \Xi'^{(s)} - \nabla_i \Xi_i''^{(s)} = \frac{\delta \epsilon}{\delta s^{(s)}}, \\ \sigma_{ji}'' &= \sigma_{ji} - \varphi_{kj} \nabla_i n_k - \psi_j \nabla_i u - \Xi_j''^{(n)} \nabla_i s^{(n)} - \Xi_j''^{(s)} \nabla_i s^{(s)} - \delta_{ij} P \end{aligned}$$

The additional terms on the right hand side of  $\sigma_{ji}''$  are the counter terms to the transport contributions. In Chapter 3 we will keep only those terms which have a non-vanishing contribution in linear order. But all terms will be taken into account in the weakly non-linear analysis in Chapter 6. Note that the differentials in the Gibbs-Duhem relation [see Eq. (3.12)] are total differentials and not partial differentials.

For the construction of the reversible currents, it is useful to collect first the properties of all quantities under time reversal  $\epsilon_T$  and parity  $\epsilon_P$  transformations (in the following table even transformations are denoted with 1 and odd with -1).

	$\rho$	$\mu$	$\vec{g}$	$\vec{v}$	$\epsilon$	$\hat{n}$	$\vec{h}$	$u$	$\Psi$	$s^{(n)}, s^{(s)}$	$\Xi^{(n)}, \Xi^{(s)}$
$\epsilon_T$	1	1	-1	-1	1	1	1	1	1	1	1
$\epsilon_P$	1	1	-1	-1	1	1	1	-1	-1	1	1

The reversible currents must show the same behavior under time reversal and parity as the time derivative of the variables and guarantee the invariance of the dynamic equations under Galilei transformations and rigid rotations. Using the above table, we write the reversible currents as follows:

$$\begin{aligned} \sigma_{ji}'' &= -\frac{1}{2} \lambda_{kji} h_k + \beta_{ij}^{(n)} \Xi^{(n)} + \beta_{ij}^{(s)} \Xi^{(s)} - \delta_{iz} \psi_j \\ Y_i^R &= -\frac{1}{2} \lambda_{ijk} \nabla_j v_k \\ Z^R &= -v_z \end{aligned}$$

**Technical Note 3.1** Reversible currents (continued)

$$\begin{aligned} X^{(n)R} &= \beta_{ij}^{(n)} \nabla_i v_j \\ X^{(s)R} &= \beta_{ij}^{(s)} \nabla_i v_j \end{aligned}$$

As a consequence of the first equation in this Technical Note these (quasi-) currents fulfill automatically the Onsager reciprocal relations.

between flow and order parameter for a uniaxial system is of the form

$$\beta_{ij}^{(n)} = \beta_{\perp}^{(n)} \delta_{ij}^{\perp} + \beta_{\parallel}^{(n)} n_i n_j, \quad (3.33)$$

$$\beta_{ij}^{(s)} = \beta_{\perp}^{(s)} (\delta_{ij} - p_i p_j) + \beta_{\parallel}^{(s)} p_i p_j. \quad (3.34)$$

Furthermore, there is a reversible coupling between the layer displacement and the velocity field in Eq. (3.26). But its coupling constant has to be unity due to the Galilei invariance of the equations.

The transverse Kronecker symbols  $\delta_{ij}^{\perp}$  in Eqs. (3.27), (3.29), and (3.32) guarantee the normalization of  $\hat{n}$ . This implies that only two of the components in Eq. (3.27) are independent. We expect  $\hat{n}$  and  $\hat{p}$  to enclose a small, but not infinitesimally small, angle. For this reason it turned out to be useful to ensure the normalization of the director by expressing it with two angular variables  $\theta$  and  $\phi$ ,

$$n_x = \sin \theta \cos \phi, \quad (3.35)$$

$$n_y = \sin \theta \sin \phi, \quad (3.36)$$

$$n_z = \cos \theta, \quad (3.37)$$

Consequently, Eq. (3.27) has to be replaced using angular variables. Denoting the right-hand side of Eq. (3.27) with  $Y_i$ , the hydrodynamic equations for  $\theta$  and  $\phi$  read

$$\begin{aligned} \frac{\partial}{\partial t} \theta + v_j \nabla_j \theta &= Y_x \cos \theta \cos \phi + Y_y \cos \theta \sin \phi \\ &\quad - Y_z \sin \theta, \end{aligned} \quad (3.38)$$

$$\frac{\partial}{\partial t} \phi + v_j \nabla_j \phi = -Y_x \frac{\sin \phi}{\sin \theta} + Y_y \frac{\cos \phi}{\sin \theta}. \quad (3.39)$$

Since the variations of  $u$  (and  $\hat{p}$ ) are infinitesimally small perturbations to the parallel orientation depicted in Fig. 2.2, we can ensure the normalization of  $\hat{p}$  by using

$$p_x = 0, \quad (3.40)$$

$$p_y = -\nabla_y u, \quad (3.41)$$

$$p_z = \sqrt{1 - p_y^2}. \quad (3.42)$$

In our first model [3], we have used a slightly different way of normalization of  $\hat{n}$  and  $\hat{p}$ . We will discuss the relation to the present procedure in Appendix B.

The set of macroscopic hydrodynamic equations we now deal with (3.26), (3.28) – (3.31), (3.38), and (3.39) follows directly from the energy density and the dissipation function without any further assumptions. We only use symmetry arguments and thermodynamic considerations.

To solve these equations we need suitable boundary conditions. In the following we will assume that the boundaries have no orienting effect on the director, *i.e.*, the homeotropic alignment of the director is only due to the layering and the coupling between the layer normal  $\hat{p}$  and the director  $\hat{n}$ . So no special boundary conditions have to be imposed on  $\theta$  and  $\phi$ . Any variation of the layer displacement must vanish at the boundaries,

$$u\left(\pm\frac{1}{2}d\right) = 0. \quad (3.43)$$

For the velocity field the situation is a little more complex. We assume no-slip boundary conditions, *i.e.*, the velocity of the fluid and the velocity of the plate are the same at the surface of the plates. It is convenient to split the velocity field into two parts: a linear shear profile  $\vec{v}_0 = \dot{\gamma}z\hat{e}_x$ , which fulfills the boundary conditions, and a correction  $\vec{v}_1$  to  $\vec{v}_0$  ( $\vec{v} = \vec{v}_0 + \vec{v}_1$ ). The boundary condition for  $\vec{v}_1$  then reads,

$$\vec{v}_1\left(\pm\frac{1}{2}d\right) = 0. \quad (3.44)$$

This condition simplifies further due to the following considerations. From Eq. (3.26) it follows that the  $z$  component of  $\vec{v}_1$  is suppressed by a factor of  $\lambda_p$  (which is typically extremely small [26, 100]). Following the arguments of Sec. 2.3 we can assume that  $\vec{v}_1$  depends only on  $y$  and  $z$  and thus conclude with Eq. (3.28) that the  $y$  component of  $\vec{v}_1$  is also suppressed by  $\lambda_p$ . For this reason, one can assume that  $v_{1,y}$  and  $v_{1,z}$  are negligible and the only relevant boundary condition for the velocity field is

$$v_{1,x}\left(\pm\frac{1}{2}d\right) = 0. \quad (3.45)$$

The validity of this assumption is nicely illustrated by our results. Figure 3.4 shows that  $v_y$  and  $v_z$  are indeed suppressed by  $\lambda_p$ .

## 3.2 Solution techniques

The aim now is twofold: Finding a spatially homogeneous solution of the governing equations (for a given shear rate) and investigating the stability of this solution. In this section we will describe some technical details of the general procedure and give the results starting in Sec. 3.3.

We write the solution as a vector  $\vec{X} = (\theta, \phi, u, v_x, v_y, v_z, P, s^{(n,s)})$  consisting of the angular variables of the director, the layer displacement, the velocity field, the pressure, and the strength of the (nematic or smectic) order parameter. For a spatially homogeneous



Quantity	$z$ symmetry	Quantity	$z$ symmetry
$u$	Even	$v_x$	Even
$\theta$	Odd	$v_y$	Odd
$\phi$	Even	$v_z$	Even
$P$	Odd	$s^{(n)}, s^{(s)}$	Odd

**Table 3.3:** If the symmetry under inversion of  $z$  is given for one component of  $\vec{X}_1$ , the symmetry of all other components follows directly from the linearized set of equations. Here we give the  $z$  symmetry of all components for the case that  $u$  is an even function of  $z$ .

situation the equations simplify significantly and the desired solution  $\vec{X}_0$  can directly be found (see Sec. 3.3). To determine the region of stability of  $\vec{X}_0$  we perform a linear stability analysis and follow the procedure described in the Technical Note 2.1 on page 18. In short, the solution of the equation  $\mathbb{L} \vec{X}_1 = \frac{\partial}{\partial t} \vec{X}_1$  (with  $\vec{X}_1 \ll \vec{X}_0$ ) is analyzed. Here  $\mathbb{L}$  denotes the operator for the linearized set of the governing equations. The ansatz for the unknown quantities must fulfill the boundary conditions [see the discussion following Eq. (3.43) on page 32] and follow the symmetry scheme given by Table 3.3. Assuming an exponential time dependence and harmonic spatial dependence of  $\vec{X}_1$ ,

$$X_{1,i} \sim \exp[(i\omega + \tau^{-1})t] \begin{Bmatrix} \cos(qy) \\ \sin(qy) \end{Bmatrix} \begin{Bmatrix} \cos(q_z z) \\ \sin(q_z z) \end{Bmatrix}, \quad (3.46)$$

fulfills all requirements (with an oscillation rate  $\omega$ , a growth rate  $\tau^{-1}$ , and a wave vector  $\vec{q} = q\hat{e}_y + q_z\hat{e}_z$ ). In this ansatz we follow our discussion from Sec. 2.3, where we argued that the undulations with the lowest threshold have a wave vector along the vorticity direction of the flow ( $\vec{q} \cdot \hat{e}_x = 0$ ). After inserting the above ansatz in the linearized set of (partial differential) equations, a set of coupled linear equations is obtained to determine  $\tau^{-1}$  and  $\omega$ . From the standard smectic- $A$  hydrodynamics it is known that shear does not destabilize the layers. Since our extended formulation of the smectic- $A$  hydrodynamics is equivalent to the standard smectic  $A$  hydrodynamics for vanishing external fields (*e.g.*, shear rate), the layers are stable for low enough shear rates, *i.e.*,  $\tau^{-1} < 0$  for small shear rates. So  $\tau^{-1} = 0$  marks the set of external parameters (shear rate) and material parameters above which  $\vec{X}_1$  grows. Typically we hold the material parameters fixed and the only external parameter is the shear rate. The solvability condition of the corresponding set of linear equations gives a relation between the shear rate [or tilt angle  $\theta_0$ , which is directly connected to the shear rate, see Eq. (3.49) below], the oscillation rate  $\omega$ , and the wave vector  $q$ . For every given  $q$  a specific shear rate (tilt angle  $\theta_0$ ) and oscillation rate can be determined which separates the stable region (below) from the unstable region (above). This defines the so called curve of marginal stability (or neutral curve)  $\theta_0(q)$  and the associated oscillation rate  $\omega(q)$ . In general, the solvability condition, *i.e.*, the determinant of the linear set of equations, is an equation with real and imaginary part. These two conditions determine  $\theta_0(q)$  and  $\omega(q)$ . In the case of vanishing oscillation rate, only the real part of the solvability condition is left, the imaginary part vanishes. If, for any given set of external parameters, the tilt angle  $\theta_0$  lies above the curve

Quantity	Prefactor	Quantity	Prefactor
$B_1$	$B_1^{-1}$	$B_0$	$B_1^{-1}$
$q_z$	$q_z^{-1}$	$K$	$q_z^2/B_1$
$\gamma_1$	$\gamma_1^{-1}$	$L_0^{(n)}, L_0^{(s)}$	$(B_1 q_z^2)^{-1}$
$L_{\parallel}^{(n)}, L_{\parallel}^{(s)}, L_{\perp}^{(n)}, L_{\perp}^{(s)}, M_0$	$B_1^{-1}$	$\nu_i$	$\gamma_1^{-1}$
$\alpha^{(n)}, \alpha^{(s)}$	$(\gamma_1 q_z^2)^{-1}$	$q_y$	$q_z^{-1}$
$\beta_{\parallel}^{(n)}, \beta_{\parallel}^{(s)}, \beta_{\perp}^{(n)}, \beta_{\perp}^{(s)}$	1	$\lambda$	1
$\rho$	$B_1/(\gamma_1^2 q_z)$	$\lambda_p$	$\gamma_1 q_z^2$

**Table 3.4:** Definition of the dimensionless quantities  $x'$  for all physical quantities  $x$ . We give the prefactor  $a$  of the definition  $x' = ax$ .

of marginal stability for at least one value of  $q$ , the spatial homogeneous state is unstable and undulations grow. The smallest shear rate (tilt angle) for which undulations can grow is called the critical shear rate (tilt angle). We point out that this linear analysis is only valid near the point where the first instability sets in. Without further investigations no prediction of the spatial structure of the developing instability can be made. Also, the nature of the bifurcation (backward or forward) must be determined by nonlinear investigations.

For practical reasons we used dimensionless units in our numerical calculations. The invariance of the governing equations under rescaling time, length, and mass allows us to choose three parameters in these equations to be equal to unity. We will set

$$B_1 = 1, \gamma_1 = 1, \text{ and } \frac{\pi}{d} = q_z = 1 \quad (3.47)$$

and measure all other quantities in the units defined by this choice, see Table 3.4 for a complete list. Nevertheless, we will keep these quantities explicitly in our analytical work.

To extract concrete predictions for experimental parameters from our calculations is a nontrivial task, because neither the energetic constant  $B_1$  nor the rotational viscosity  $\gamma_1$  are used for the hydrodynamic description of the smectic- $A$  phase (but play an important role in our model). Therefore, we here rely on measurements in the vicinity of the nematic–smectic- $A$  phase transition. Measurements on low molecular weight liquid crystals made by Litster [74] in the vicinity of this transition indicate that  $B_1$  is approximately one order of magnitude less than  $B_0$ . As for  $\gamma_1$  we could not find any measurements that would allow an estimate of its value in the smectic- $A$  phase. In the nematic phase  $\gamma_1$  increases drastically towards the nematic–smectic- $A$  transition (see, *e.g.*, Ref. [43]). In the Technocal Note 3.2 on page 37 we will motivate the numerical values used in this work. Numerical simulations on a molecular scale are also a promising

approach to determine these constants [117]. In Chapter 5 we will show that it is possible to extract all necessary dimensionless constants from molecular dynamics simulations and to give a quantitative comparison between this analytic theory and the simulations.

The rest of this chapter is organized as follows. First we discuss the spatially homogeneous solution in Sec. 3.3. Due to the complexity of the full set of governing equations, we then start our analysis with a minimal set of variables ( $\theta$ ,  $\phi$ , and  $u$ ) and suppress the coupling to the other variables (see Sec. 3.4.1). Step by step, the other variables will be taken into account in Secs. 3.4.2 and 3.4.3. The general picture of the instability will turn out to be already present in the minimal model, but many interesting details will be added throughout the next sections. First we assume a stationary instability (*i.e.*, we let  $\omega = 0$ ); later on we discuss the possibility for an oscillatory instability and have a look at some special features of the system (Chapter 4).

### 3.3 Spatially homogeneous state

The starting point of our further analysis is the unperturbed shear state. To find this state, we begin with a number of assumptions and show afterwards that the resulting state fulfills the governing equations. The anchoring of the director is done *via* the coupling to the layering, therefore, we look for a solution in which the director is constant throughout the sample ( $\theta_0(x, y, z) = \theta_0$  and  $\phi_0(x, y, z) = \phi_0$ ). For the same reason,  $s_0^{(n)}$  and  $s_0^{(s)}$  should be constants. Since there is no direct interaction between the layering and the shear profile,  $u_0 = 0$  is a good first choice. Introducing these ansätze into our generalized form of the Navier-Stokes equation (3.29) we find that a linear shear profile

$$\vec{v}_0 = \dot{\gamma} z \hat{e}_x \quad (3.48)$$

is a solution to this equation.<sup>6</sup> Using the relations we have up to now, Eqs. (3.26) and (3.28) are also satisfied. For the director and the strength of the order parameters, the reversible cross couplings to the velocity field do not vanish and must be balanced by dissipative (diagonal) currents. Writing Eq. (3.27) in angular variables shows that only  $\theta_0$  depends on the shear rate  $\dot{\gamma}$ , whereas  $\phi_0 = 0$  solves the corresponding equation. The shear induced director tilt is given by the solution to

$$\left( \frac{\lambda + 1}{2} - \lambda \sin^2(\theta_0) \right) \dot{\gamma} = \frac{B_1}{\gamma_1} \sin(\theta_0) \cos(\theta_0) + \frac{B_0}{\gamma_1} \sin(\theta_0) [1 - \cos(\theta_0)]. \quad (3.49)$$

Expanding this expression for small  $\theta_0$  we find

$$\theta_0 = \dot{\gamma} \frac{\gamma_1}{B_1} \frac{\lambda + 1}{2} + O(\theta_0^3), \quad (3.50)$$

---

<sup>6</sup>This gives now a clear-cut motivation for our—at first sight—purely technical splitting of  $\vec{v}$  in the discussion around Eq. (3.44)

which shows that  $\theta_0$  starts as a linear function of the shear rate. Combining Eqs. (3.48) and (3.49) with the reversible currents in Eqs. (3.30) and (3.31), we see that the reversible quasi-current  $\beta_{ij}^{(n)} \nabla_j v_i$  for the nematic order parameter is non-zero, because  $\beta_{ij}^{(n)}$  depends on  $\hat{n}$  and, therefore, on  $\theta_0$ . In contrast, the reversible quasi-current for the smectic order parameter  $\beta_{ij}^{(s)} \nabla_j v_i$  is zero, since  $\beta_{ij}^{(s)}$  depends on the (unchanged)  $\hat{p}$ . Consequently,  $s_0^{(n)}$  is given by

$$\alpha^{(n)} L_0 s_0^{(n)} = -(\beta_{\parallel}^{(n)} - \beta_{\perp}^{(n)}) \sin(\theta_0) \cos(\theta_0) \dot{\gamma}, \quad (3.51)$$

but  $s_0^{(s)}$  is zero—the shear profile modifies only the strength of the nematic order parameter.

In contrast to the director tilt, the lowest-order correction to the nematic order parameter is quadratic in the shear rate (tilt angle),

$$s_0^{(n)} = -\frac{2}{\lambda + 1} \frac{B_1}{\gamma_1} \frac{\beta_{\parallel}^{(n)} - \beta_{\perp}^{(n)}}{\alpha^{(n)} L_0} \theta_0^2 + O(\theta_0^4). \quad (3.52)$$

The spatially homogeneous state constructed so far solves all governing equations. Therefore we consider in the following perturbations around this state.

We are not aware of any experimental data, which would allow a direct comparison with these results. In Chapter 5, we will show that the results of molecular dynamic simulations of the model systems are in quantitative agreement with the analytic predictions.

## 3.4 Stationary instability

### 3.4.1 Minimal set of variables

We start our theoretical considerations by using a minimal set of variables. As we will show, already this minimal set exhibits the central features of the instability. In the following section we will take into account all liquid crystalline variables, *i.e.*, the layer displacement  $u$  and the director angles  $\phi$  and  $\theta$ , but neglect all couplings of these variables to other quantities describing the system, namely, the velocity field and the moduli of the nematic and smectic order parameters. Nevertheless we keep the spatially homogeneous director tilt of Eq. (3.49). Within these approximations the equations to

**Technical Note 3.2** Typical values of the material parameters

For low molecular weight liquid crystals a number of dimensionless material parameters can be estimated. Our estimates are based on measurements on 4-*n*-octyloxy-4'-cyanobiphenyl (8OCB, see, *e.g.*, Refs. [26, 43, 56, 74, 136]). The precision of the values given below varies: The elastic constants  $B_0$  and  $K$  have been measured in many smectic-*A* liquid crystals, their order of magnitude is clear.  $B_1$  has been determined in the smectic-*A*–nematic transition region by Litster *et al.*. The rotational viscosity  $\gamma_1$  is only known in the nematic phase and increases steeply towards the smectic-*A*–nematic transition. Within the nematic phase it is of the order of the other viscosities  $\nu_i$ . The flow alignment parameter  $\lambda$  in the nematic phase is typically of order of unity. There are some indications that  $\lambda$  decreases in the transition region to the nematic–smectic-*A* transition [83], but, again, nothing is known about its value in the smectic-*A* phase. We will assume  $\nu_i/\gamma_1$  and  $\lambda$  to have similar values in both phases. To our knowledge, none of the material parameters connected with the strength of the order parameter has been measured up to now. For our estimates of these parameters see the discussion of Fig. 3.7 on page 46.

	cgs	SI
$B_0$	$\sim 3 \cdot 10^7 \text{ erg cm}^{-3}$	$\sim 3 \cdot 10^6 \text{ J m}^{-3}$
$B_1$	$\sim 10^6 \text{ erg cm}^{-3}$	$\sim 10^5 \text{ J m}^{-3}$
$K$	$\sim 10^{-6} \text{ dyn}$	$\sim 10^{-11} \text{ N}$
$\nu_i$	$\sim 0.2 \text{ Poise}$	$\sim 0.02 \text{ Pa s}$
$\gamma_1$	$\gtrsim 0.05 \text{ Poise}$	$\gtrsim 0.005 \text{ Pa s}$
$\lambda$	1	1
$\lambda_p$	$\sim 10^{-14} \text{ cm}^2 \text{ Poise}^{-1}$	$\sim 10^{-17} \text{ m}^2 \text{ Pa}^{-1} \text{ s}^{-1}$
$q_z$	$\sim 3 \cdot 10^2 \text{ cm}^{-1}$	$\sim 3 \cdot 10^4 \text{ m}^{-1}$

These values lead to the dimensionless parameters summarized in the following table.

$B_0 B_1^{-1}$	$K q_z^2 B_1^{-1}$	$\nu_i \gamma_1^{-1}$	$\lambda_p \gamma_1 q_z^2$
$\sim 30$	$\sim 10^{-7}$	$\lesssim 0.4$	$\sim 5 \cdot 10^{-10}$

solve are,

$$\begin{aligned}
 0 = & A_\theta \left\{ 2\dot{\gamma}\lambda \sin(\theta_0) \cos(\theta_0) \right. \\
 & + \frac{B_0}{\gamma_1} [\sin^2(\theta_0) - \cos^2(\theta_0) + \cos(\theta_0)] \\
 & \left. - \frac{B_1}{\gamma_1} [\sin^2(\theta_0) - \cos^2(\theta_0)] \right\} \\
 & - A_u \frac{B_0}{\gamma_1} \sin(\theta_0) q_z,
 \end{aligned} \tag{3.53}$$

$$0 = A_\phi \frac{1}{2} \dot{\gamma} (\lambda + 1) - A_u \frac{B_1}{\gamma_1} q, \tag{3.54}$$

$$\begin{aligned}
 0 = & A_\theta \lambda_p B_0 \sin(\theta_0) q_z \\
 & + A_\phi \lambda_p B_1 q \sin(\theta_0) \cos(\theta_0) \\
 & - A_u \lambda_p \left[ - B_0 q^2 (1 - \cos(\theta_0)) \right. \\
 & \left. + B_1 q^2 \cos^2(\theta_0) + K q^4 + B_0 q_z^2. \right]
 \end{aligned} \tag{3.55}$$

Here we inserted an ansatz of the type (3.46) and use  $A_x$  for the linear amplitude of a variable  $x$ . One can solve these equations either by expanding them in a power series of  $\theta_0$  (expecting to get a closed result for the critical values) or numerically. It turns out that such an expansion has to include at least terms up to the order  $\theta_0^5$  to get physically meaningful analytic results. These analytic approximations are rather long and complicated. For this reason the closed expressions have no advantage over the purely numerical solutions and we do not give the analytical approximations explicitly. We will present and discuss our findings using the minimal set of variables in the following section, in direct comparison to the results of the full set of equations.

### 3.4.2 Coupling to the velocity field

Neglecting the coupling between velocity field and nematic director and vice versa is a rather crude approximations since it is well known, that this coupling plays an important role in nematic hydrodynamics [26, 104]. So the natural next step is to include this coupling and to perform a linear stability analysis of Eqs. (3.26) – (3.29), (3.38), (3.39). In this case, the standard procedures lead to a system of seven coupled linear differential equations. Following the discussion after Eq. (3.43) these equations can be solved by an ansatz of the type given in Eq. (3.46). This reduces the system of equations to seven coupled linear equations which are easily solved using standard numerical tools (such as singular value decomposition and inverse iteration to find the eigenvectors). Due to the complexity of the equations, we used Maple to determine the final set of linear equations. The key ingredients of this Maple script are given in Appendix C.

Figure 3.1 gives a comparison of typical neutral curves for the first approach (see Ap-

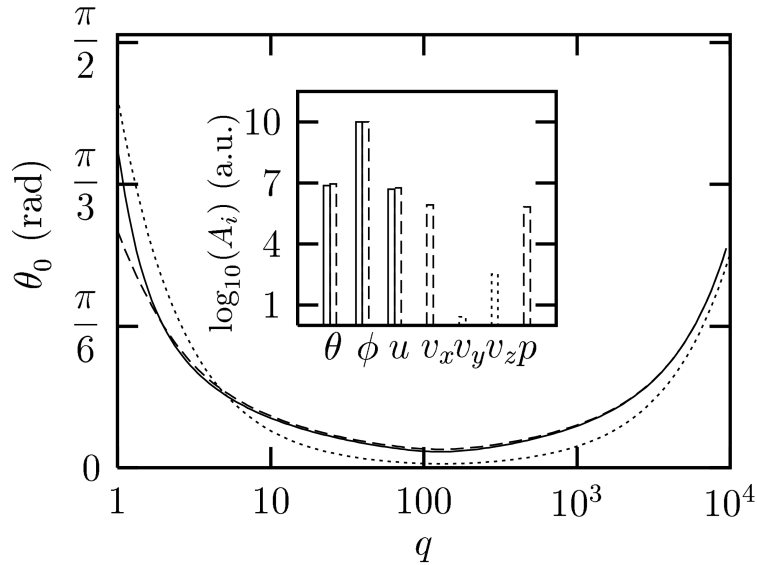


**Figure 3.1:** Here a comparison of the neutral curves using our first approach (....., see Appendix B for details), the minimal set of variables (——) and including the velocity field (---) is depicted. The overall behavior does not change, but the critical values are altered due to the coupling with the velocity field. For this plot we used (in the dimensionless units discussed in Sec. 3.2)  $B_0 = 30$ ,  $K = 10^{-7}$ ,  $\lambda = 0.7$ ,  $\nu_1 = \nu_2 = \nu_3 = \nu_4 = \nu_5 = 0.4$ , and  $\lambda_p = 10^{-6}$ . The inset shows the linear amplitudes  $A_i$  (where  $i$  stands for  $\theta$ ,  $\phi$ , etc.) at onset. We omitted the amplitudes of the first approach, because they are quite similar to the minimal set of variables. Since the logarithm of the amplitudes is shown, amplitudes with different sign are shown with a different line style. Using the minimal set (left bars) all amplitudes have the same sign (——). Including the velocity field (right bars) some amplitudes are positive (---), others negative (.....). Note that we use in this and all following plots the dimensionless units defined by Eq. (3.47).

pendix B for details), the minimal model, and calculations including the velocity field.<sup>7</sup> The overall shape of the neutral curve is not changed in these various approaches but a shift of the critical tilt angle is already visible.<sup>8</sup> The inset shows the relative amplitudes of the linear solutions at onset (using a logarithmic scale). For  $\theta$ ,  $\phi$ , and  $u$  the left bars correspond to the minimal model and the right bars to the extended version. The amplitude for the first approach are not shown, because they are quite similar to the minimal set of variables. Note that amplitudes with a different sign are shown with a different line style in the histograms (see the figure caption for details). Comparing the amplitudes of the velocity components, clearly  $A_{v_x}$  is several orders of magnitude larger than  $A_{v_y}$  and  $A_{v_z}$ , justifying our earlier approximation [see discussion to Eqs. (3.44) and (3.45) on page 32]. We will come back to this point in the discussion of Fig. 3.4.

Let us have a closer look at the differences between the minimal and the extended set

<sup>7</sup>Due to a typographical error in Ref. [4] the following curves vary slightly from the curves in Ref. [4]. We emphasize that none of the major results in this reference have changed.

<sup>8</sup>Note that the critical wave vector stays almost unchanged.

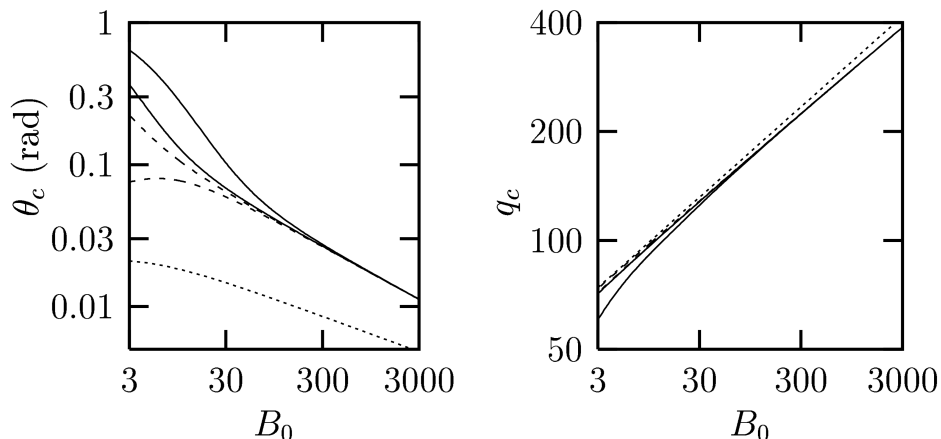


**Figure 3.2:** The minimal set and the version including the velocity field agree for large values of  $B_0$  and differ only for small  $B_0$ . Our first approach of Appendix B (.....) systematically underestimates the critical tilt angle but gives a good approximation for the critical wave vector. The solid lines (—) show results including the velocity field, the dashed lines (- - -) correspond to the minimal set of variables. When two curves are shown for the critical tilt angle,  $\lambda = 1.3$  corresponds to the upper curve and  $\lambda = 0.7$  was used for the lower curve (at small  $B_0$ ). In the plot of the critical wave vector  $\lambda = 0.7$  corresponds to the upper curves.

of equations and follow these differences along some paths in parameter space. As mentioned in Sec. 3.2, we can omit some of the physical parameters by using dimensionless parameters. In Figs. 3.2 – 3.6 we show the dependence of the critical values of the tilt angle and wave vector on the dimensionless parameters [as defined in Eq. (3.47)]. For all these figures we used the same basic set of parameters:  $B_0 = 30$ ,  $K = 10^{-7}$ ,  $\lambda = 0.7$ ,  $\nu_1 = \nu_2 = \nu_3 = \nu_4 = \nu_5 = 0.4$ , and  $\lambda_p = 5 \cdot 10^{-10}$ . These values are estimates for a typical thermotropic low molecular weight liquid crystal, see Technical Note 3.2 on page 37 for details. As far as  $B_1$  and  $\gamma_1$  are concerned, see also the discussion following Eq. (3.47) on page 34. As a function of the flow alignment parameter  $\lambda$ , the critical values can show a strong variation between the ranges  $\lambda < 1$  and  $\lambda > 1$  (see Fig. 3.6 for more details). Therefore we discuss in addition the situation for  $\lambda = 1.3$  to indicate the range of possible values.

Considering the critical values as a function of the compression modulus  $B_0$  results in a rather simple situation (Fig. 3.2). For small values of  $B_0$  a significant influence of the coupling between the director and velocity field is apparent, which also shows a strong dependence on  $\lambda$ . For large  $B_0$  these differences vanish and the solution of the minimal set and the set including the velocity converge into one single curve. Our first approach differs essentially in the critical tilt angle which is systematically underestimated by approximately a factor 2. In contrast the critical wave vector of the first approach is in good agreement with the other versions.

At this point a comparison to dilated smectic- $A$  is instructive. It is well known [16, 28] that in a dilated smectic- $A$  the critical wave vector and the critical dilation show a power



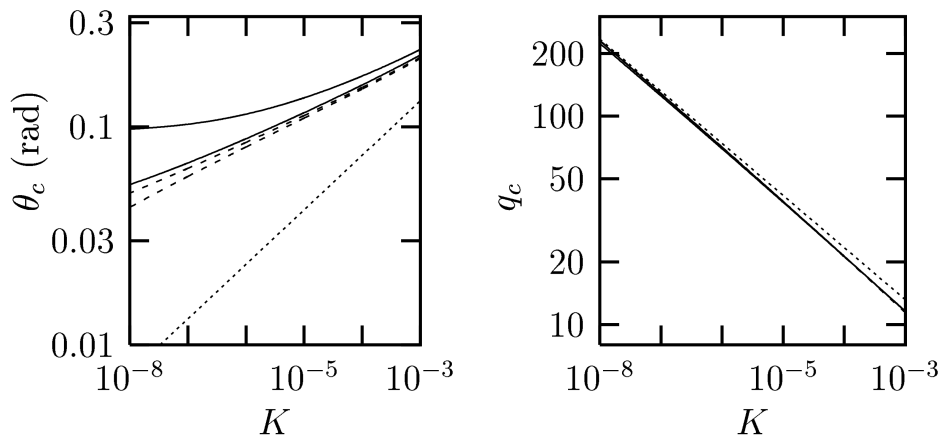


**Figure 3.3:** Plotting the critical values as a function of the bending modulus  $K$  shows a convergence of the curves, which is, nevertheless, not as pronounced as in the case of Fig. 3.2. The influence of  $\lambda$  on the critical tilt angle is significant ( $\lambda = 1.3$  in the upper curves and  $\lambda = 0.7$  in the lower ones). Again the solid lines (—) show results including the velocity field, the dashed lines (- - -) correspond to the minimal set of variables, and the dotted lines (.....) depict the outcome of the first approach. Note that the wave vectors of the minimal set and of the calculations including the velocity field are indistinguishable within the resolution of the plot.

law behavior as a function of  $B_0$  with exponents  $1/4$  and  $-1/2$ , respectively. In the limit of large  $B_0$  we found the same exponents already in our earlier analysis [3]. If we fit power laws to our results for  $B_0 > 10^2$  we find the exponents equal to  $\approx 0.24$  and  $\approx -0.38$  for  $q_c$  and  $\theta_c$ , respectively (note that the dilation in our model is  $\approx \frac{1}{2}\theta_c^2$ ). For our first approach it is evident from the analytic results [see Eqs. (B.8) and (B.9)] that  $q_c \sim B_0^{1/4}$  and  $\theta_c \sim B_0^{-1/4}$ , where the latter relation holds only for large  $B_0$ .

A similar, but less pronounced, situation is apparent, when plotting the critical values as a function of the bending modulus (see Fig. 3.3). The curves tend to converge for large  $K$ , but there remains a difference between the minimal set of variables and the calculations including the the velocity field. Again, the critical tilt angle of the first approach is typically a factor 2 smaller than in the other calculations. Fitting the  $K$  dependence with power laws (here for  $K > 10^{-4}$ ) only the critical wave number exhibits an exponent close to the values expected from dilated smectic- $A$  ( $\approx -0.26$  vs.  $-\frac{1}{4}$ ).

Form the discussion to Figs. 3.2 and 3.3, we can conclude that the critical wave vector is rather robust against variations in the number of free variables. But for a good estimate of the critical tilt angle it is desirable to have a set of equations which is as complete as possible. This is especially true if  $B_0$  and  $B_1$  differ by less than a factor of  $10^2$ . Therefore, the critical tilt angle (or shear rate) is the better parameter for an experimental test of our model.

In contrast to the cases discussed above, the permeation constant  $\lambda_p$  has no strong influence on the critical values. For dimensionless values  $\lambda_p < 10^{-6}$  the critical values do not change at all with  $\lambda_p$ . If we allow  $\lambda_p \gtrsim 10^{-5}$ , variations within a factor of two

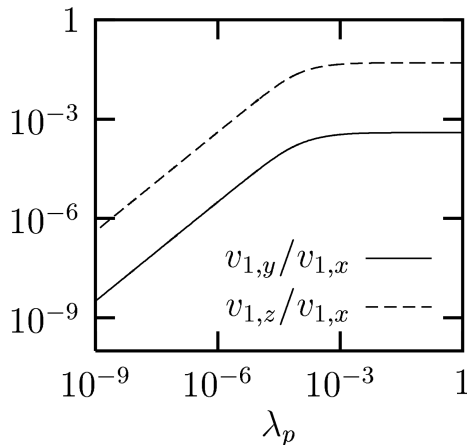


**Figure 3.4:** In all our calculations  $v_{1,x}$  is the dominating component of  $\vec{v}_1$ . This graph demonstrates that the other components are suppressed by  $\lambda_p$  (making them almost negligible).

are possible. The permeation constant is known to be very small. In our dimensionless units we expect it to be of the order of  $\sim 5 \cdot 10^{-10}$  for low molecular weight thermotropic liquid crystals. For this reason it is a good approximation to neglect its influence on the critical values. In Sec. 3.1 we have emphasized that the  $y$  and  $z$  components of the velocity field are suppressed *via*  $\lambda_p$ . These qualitative arguments are clearly confirmed by our numerical results: In all our calculations  $v_{1,x}$  is the dominating component of  $\vec{v}_1$ , especially, the ratio  $v_{1,y}/v_{1,x}$  is of the order of  $\lambda_p$  over the whole range of physically relevant values of  $\lambda_p$  (see Fig. 3.4). This fact nicely supports our argument that we can neglect the boundary condition for  $v_{1,y}$ , because  $v_{1,y}$  vanishes anyway. For  $v_{1,z}$  the suppression is less pronounced (by a factor of  $q/q_z$ ), but it is also much smaller than  $v_{1,x}$ .

Out of the five viscosities only two ( $\nu_2$  and  $\nu_3$ ) show a significant influence on the critical values. In Fig. 3.5 we present the dependence of  $\theta_c$  and  $q_c$  on an assumed isotropic viscosity (upper row) and on these two viscosity coefficients (middle and lower row). Since the flow alignment parameter  $\lambda$  has a remarkable influence on these curves we have chosen four different values of  $\lambda$  in this figure, namely,  $\lambda = 0.7$ ,  $\lambda = 1.3$ ,  $\lambda = 2$ , and  $\lambda = 3.5$ . Note that the curves where only  $\nu_2$  is varied are already in good agreement to the curves corresponding to an isotropic viscosity tensor. In this parameter range the coefficient  $\nu_2$  dominates the behavior. Note that the influence of  $\nu_3$  on the critical values is already much smaller than that of  $\nu_2$ . We left out the equivalent graphs for the other viscosity coefficients, because they have almost no effect on the critical values. In Sec. 2.2 we have shown that an anisotropic viscosity tensor in standard smectic-A hydrodynamics does not suffice to reorient the layers. As an annex to this discussion we can now conclude that an appropriate anisotropy in  $\nu_{ijkl}$  facilitates the reorientation in our extended description. The critical tilt angle is lowered when the viscosity coefficient  $\nu_2$  (which governs the apparent viscosity of the perpendicular orientation) is smaller than  $\nu_3$  (which gives the apparent viscosity of the parallel orientation).

Up to now, the dependences of the critical values on the material parameters were smooth curves with no pronounced structure. In this respect the situation is completely different for the case of the flow alignment parameter  $\lambda$ . As shown in Fig. 3.6, there is a clear

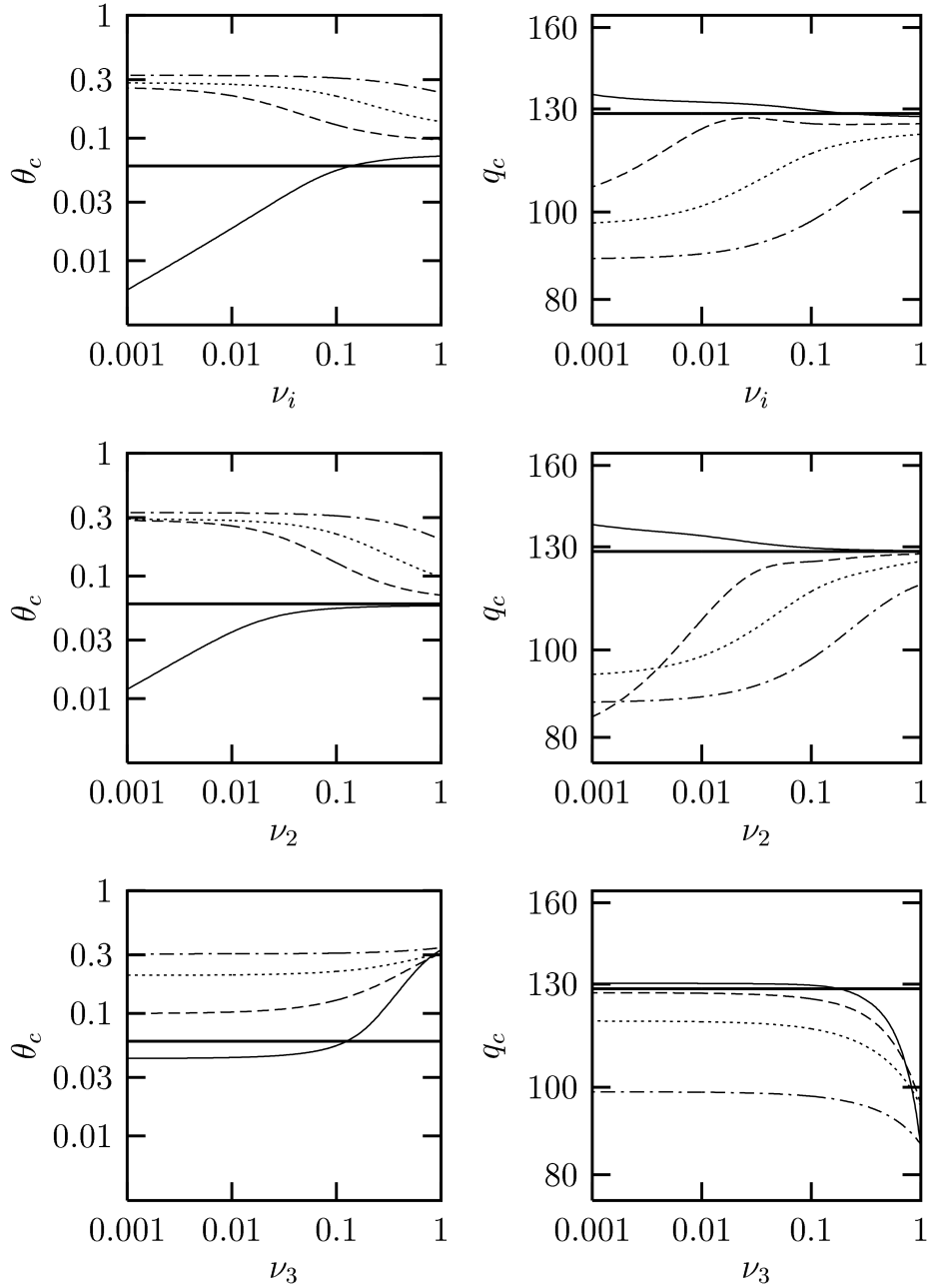


**Figure 3.5:** Only the viscosities  $\nu_2$  and  $\nu_3$  influence the critical parameters significantly. The upper row depicts the dependence on a isotropic variation of the viscosity. In the middle and lower row we present the variation with  $\nu_2$  and  $\nu_3$  setting the other viscosities to  $\nu_i = 0.1$ . Here the thick solid lines ( ——— ) represent the minimal set of variables. For the full set of variables we have chosen four different values of  $\lambda$ : the solid curves ( ——— ) with  $\lambda = 0.7$ , the dashed curves ( - - - ) with  $\lambda = 1.3$ , the dotted curves ( ..... ) with  $\lambda = 2$ , and the dot-dashed curves ( - . - ) with  $\lambda = 3.5$ . Note the similarities between the curves for small ( ——— ) and large  $\lambda$  ( - . - ) in the upper and middle row. In these regimes  $\nu_2$  is the dominating viscosity.

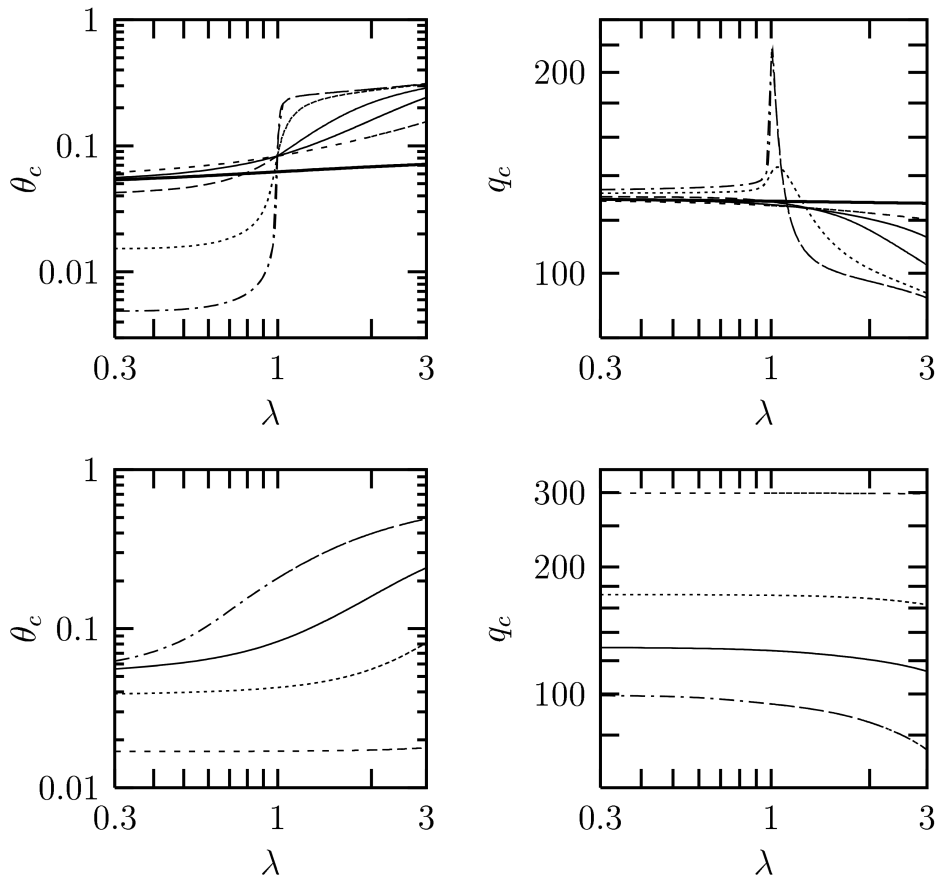


**Figure 3.6:** Plotting the critical values as functions of the flow alignment parameter  $\lambda$  reveals an interesting structure for  $\lambda \approx 1$ . In the upper row we plot this dependence for a set of (isotropic) viscosities ranging from  $\nu_i = 10$  (short dashed line,  $---$ ) down to  $\nu_i = 10^{-3}$  (dot-dashed line,  $-\cdot-$ ). The thick solid line (  $\text{—}$  ) reveals that this dependence on  $\lambda$  is absent in the minimal model. The lower row illustrates the behavior for varying layer compressibility  $B_0$  with  $B_0 = 10$  for the dot-dashed curve (  $-\cdot-$  ) and  $B_0 = 1000$  for the dashed curve (  $---$  ). In all plots the solid lines (  $\text{—}$  ) give the behavior for the typical values we deduced in the Technical Note 3.2 on page 37. For an interpretation of this behavior see the text.

change in behavior for  $\lambda \approx 1$ . The critical tilt angle is increased for values of  $\lambda$  larger than unity and the critical wave vector may exhibit a maximum at  $\lambda \approx 1$ . Figure 3.6 illustrates how this structure depends on the viscosities (assuming all five viscosities to be equal) and on the elastic constants of the layers. In the first row we follow this behavior for viscosities varying from  $\nu_i = 10$  down to  $\nu_i = 10^{-3}$ . Clearly, the influence of  $\lambda$  is more pronounced the lower the viscosities are. Both elastic constants of the layers, the compressibility  $B_0$  and the bending modulus  $K$  (in our dimensionless units  $B_1 = 1$ ), have, in general, a similar influence on the shape of the graphs: The smaller the elastic constants are, the more pronounced the structure becomes. For this reason we just give the plot for  $B_0$  (second row in Fig. 3.6) and omit the plot for  $K$ .

These dependences on the system parameters give some important hints for an interpretation of Fig. 3.6. The currents and quasi-currents for the velocity field and the director consist of two parts [see Eqs. (3.27) and (3.29)]: a diagonal one (coupling, *e.g.*, the components of  $\vec{v}$  among each other) and an off-diagonal one (coupling the director to the velocity field). The former ones are proportional to the elastic constants or to the viscosity tensor, whereas the latter one is a function of the flow alignment parameter. So reducing either the elastic constants or the viscosities increases the influence of the cross-coupling terms in these equations. The influence of the flow alignment term is strongest when it is dominating in the currents and quasi-currents. The next step in the interpretation of the shape of the curves is to have a closer look at the structure of the cross-coupling term. The flow alignment tensor  $\lambda_{ijk} = \frac{1}{2} [(\lambda - 1)\delta_{ij}^\perp n_k + (\lambda + 1)\delta_{ik}^\perp n_j]$  obviously changes its behavior for  $\lambda = 1$ , because the first part changes its sign. For example, the  $\phi$  component of the director is coupled to the  $x$  and  $z$  component of the velocity field by the terms  $(\lambda - 1)/2 \partial_y v_x$  and  $(\lambda - 1)/2 \cot(\theta_0) \partial_y v_z$ . The monitored structure in the plots cannot be attributed to one single cross-coupling term, but the given examples demonstrate that something should happen in this parameter range.

### 3.4.3 Including the order parameters

In the preceding paragraphs we investigated undulations assuming a constant modulus of the order parameters  $S^{(n)} = S_0^{(n)} + s_0^{(n)}$  and  $S^{(s)} = S_0^{(s)} + s_0^{(s)}$ . In general, one would expect that the undulations in the other observable quantities should couple to some extent to the order parameter. In the formulation of the free energy (see Sec. 3.1) we have assumed that  $S^{(n)}$  and  $S^{(s)}$  vary only slightly around  $S_0^{(n)}$  and  $S_0^{(s)}$ , consequently, only the lowest order terms in  $s^{(n)}$  and  $s^{(s)}$  contribute to the free energy. For the spatially homogeneous state we had [see Eqs. (3.51) and (3.52)] a correction to the nematic  $S^{(n)}$  proportional to the square of the shear rate ( $\theta_0 \sim \dot{\gamma}$  for low  $\dot{\gamma}$ ),

$$s_0^{(n)} = - \frac{2}{\lambda + 1} \frac{B_1}{\gamma_1} \frac{\beta_{\parallel}^{(n)} - \beta_{\perp}^{(n)}}{\alpha^{(n)} L_0} \theta_0^2 + O(\theta_0^4).$$

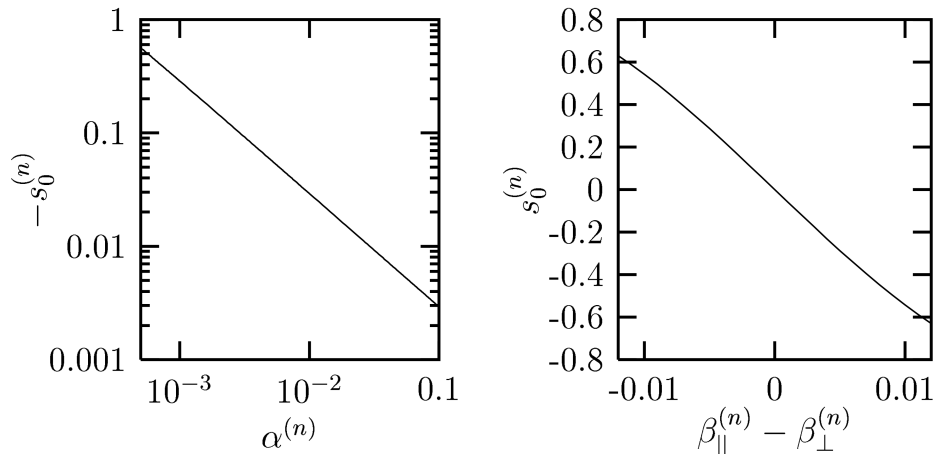


**Figure 3.7:** Evaluating Eqs. (3.52) and (3.56) at onset gives an important restriction on the range of possible parameter values (here the cases of  $\alpha^{(n)}$  and  $\beta_{\parallel}^{(n)} - \beta_{\perp}^{(n)}$ , where  $\beta_{\parallel}^{(n)} - \beta_{\perp}^{(n)} = 5 \cdot 10^{-3}$  and  $\alpha^{(n)} = 10^{-3}$ , respectively). Note that the critical  $\theta_0$  is a function of the material parameters.

As a consequence,  $s_0^{(n)}$  must be small compared to  $S_0^{(n)}$  (which is by construction limited to the range  $0 \leq S_0^{(n)} \leq 1$ ). Thus a reasonable restriction is

$$|s_0^{(n)}| \lesssim 0.5. \quad (3.56)$$

As shown in Fig. 3.7, evaluating this relation at the onset of the instability reduces significantly the physically reasonable range for some parameters. This restriction applies only for the nematic material parameters and, in general, nothing can be said about the corresponding smectic parameters. We will, however, take the smectic parameters in the same range as the nematic ones. In our picture the nematic order is a necessary requirement for the smectic order, so we expect the strength of both order parameters to be strongly coupled.

If not indicated otherwise we used  $L_0^{(n)} = L_0^{(s)} = 0.1$ ,  $L_{\perp}^{(n)} = L_{\perp}^{(s)} = 0.01$ ,  $L_{\parallel}^{(n)} - L_{\perp}^{(n)} = L_{\parallel}^{(s)} - L_{\perp}^{(s)} = 0.005$ ,  $M_0 = 10^{-4}$ ,  $\beta_{\perp}^{(n)} = \beta_{\perp}^{(s)} = 0.01$ ,  $\beta_{\parallel}^{(n)} - \beta_{\perp}^{(n)} = \beta_{\parallel}^{(s)} - \beta_{\perp}^{(s)} = 0.005$ ,  $\alpha^{(n)} = \alpha^{(s)} = 0.001$  for the plots of this section (along with parameter set specified in the preceding section).

The ansatz for  $s_1^{(n)}$  and  $s_1^{(s)}$  following Eq. (3.46) reads

$$s_1^{(n)} = A_s^{(n)} \exp[(i\omega + \tau^{-1})t] \sin(q_z z) \cos(qy), \quad (3.57)$$

$$s_1^{(s)} = A_s^{(s)} \exp[(i\omega + \tau^{-1})t] \sin(q_z z) \cos(qy). \quad (3.58)$$

The modulations of  $S^{(n)}$  and  $S^{(s)}$  in the linear analysis are maximum at the boundaries and in phase with the layer displacement  $u$ . The sign of the amplitudes  $A_s^{(n)}$  and  $A_s^{(s)}$  depend on the coupling to the velocity field (only the anisotropic part  $\beta_{\parallel}^{(n)} - \beta_{\perp}^{(n)}$  is relevant) and on the coupling to the director undulations (*via*  $M_{ijk}$ , only for the nematic

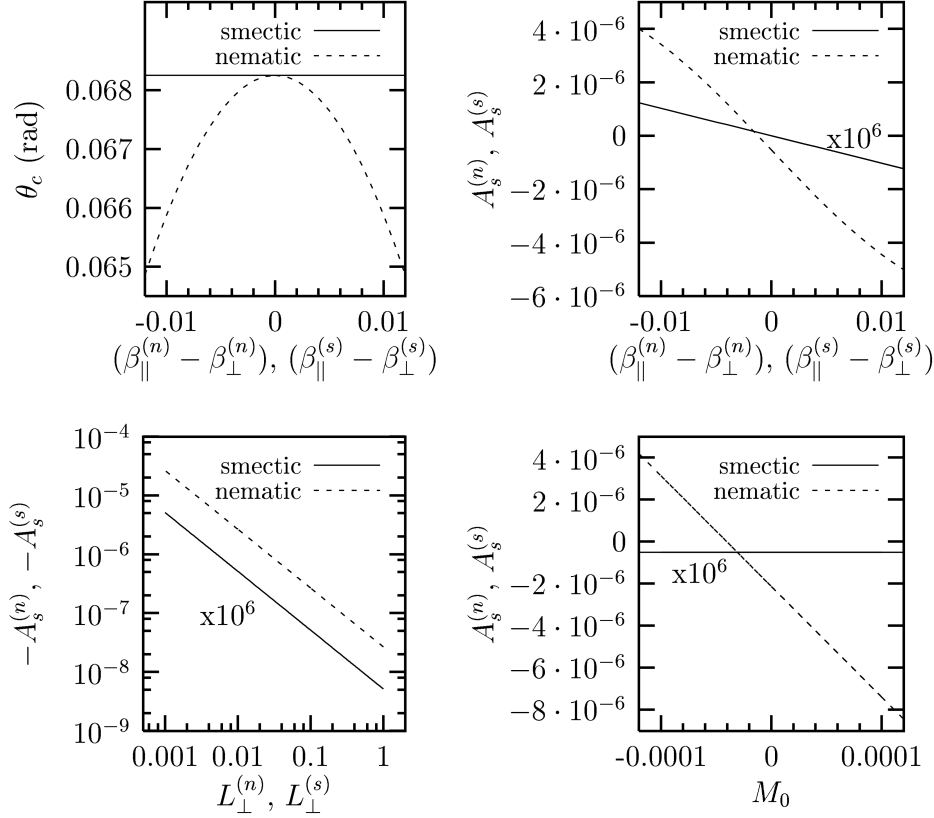


**Figure 3.8:** Out of the material parameters connected with the order parameter, only  $\beta_{\parallel}^{(n)} - \beta_{\perp}^{(n)}$  has a measurable effect on the critical values (but only on the critical tilt angle). Some more parameters can influence the amplitudes of the order parameter undulation, namely,  $L_{\perp}^{(n)}$ ,  $L_{\perp}^{(s)}$ , and  $M_0$  (the latter one is only present in the case of the nematic order parameter). All amplitudes have been normalized such that  $A_{\phi} = 1$ . Note that the smectic  $A_s^{(s)}$  is typically much smaller than its nematic equivalent. For this reason we multiplied its value in all plots by  $10^6$ .

amplitudes  $A_s^{(n)}$ ). If one assumes that shear reduces (and does not increase) the modulus of the order parameter, the nematic contribution  $\beta_{\parallel}^{(n)} - \beta_{\perp}^{(n)}$  is positive [Eqs. (3.51) and (3.52)]; once again nothing can be said about the smectic value for  $\beta_{\parallel}^{(s)} - \beta_{\perp}^{(s)}$ .

In general, the critical values are not at all or only very slightly influenced by the coupling to the modulus of the order parameter. Figure 3.8 summarizes the parameters with the largest influence on  $A_s^{(n)}$  and  $A_s^{(s)}$ . In almost all investigated cases the modulation of the nematic order is much larger than that of the smectic order. Whether the order is reduced or increased in regions where the layers are compressed depends in the phenomenological constants  $\beta_{\parallel}^{(n)} - \beta_{\perp}^{(n)}$ ,  $\beta_{\parallel}^{(s)} - \beta_{\perp}^{(s)}$ , and  $M_0$ , which have not been measured up to now.

The above results reveal some interesting features. As shown in Table 3.3, the modulations of the order parameter change sign under inversion of the  $z$  axis. Considering the boundary condition (*i.e.*, taking our ansatz), this leads to the fact that the effect

on the degree of the order is maximum near the boundaries. Whether the strength of the order is reduced in regions where the layers are dilated or compressed depends strongly on the balance between the two cross coupling terms acting on  $s^{(n)}$ :  $\beta_{ij}^{(n)} \nabla_i v_j$  and  $M_{ijk} \nabla_i n_j \nabla_k s^{(n)}$ . If the anisotropic part of  $\beta_{ij}$  is large ( $\beta_{\parallel} - \beta_{\perp} \gtrsim 0.002$ ) and positive (as discussed above), the strength of the nematic order parameter is reduced where the layers are dilated. But if the anisotropy of  $\beta_{ij}$  is small ( $\beta_{\parallel} - \beta_{\perp} \lesssim 0.001$ ), a negative  $M_0$  will invert the situation: The strength of the order is reduced in compressed regions. Since the probability for the formation of defects is higher in places where the order parameter is lower, we have identified areas where the creation of defects is facilitated. At this point one can speculate that these regions of reduced order parameters might lead to a breaking of the layers (in the compressed regions) or an introduction of new layers (in dilated regions) and thus the undulation amplitude may grow further. In Fig. 3.9 we show a possible picture in the case when compression reduces the strength of the order. Interestingly, experiments in block copolymers by Laurer *et al.* [69] show a defect structure close to the boundaries which is consistent with this picture.



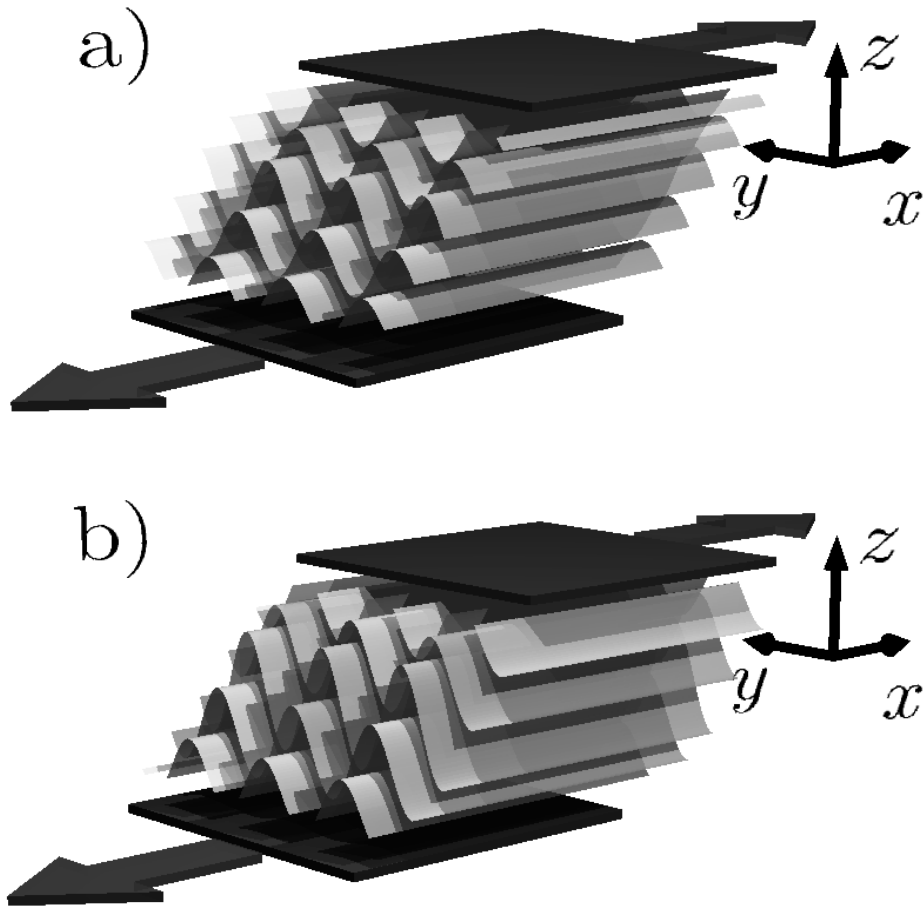


**Figure 3.9:** Since the strength of the order is reduced most near the boundaries, one can speculate that the layers are perforated predominantly in this region (see part a)) and allow an increasing undulation amplitude through the formation of defects close to the boundaries.



---

# Chapter 4

## Linear Analysis: Discussion of the results<sup>1</sup>

### 4.1 Oscillatory instability

All our arguments in the previous sections were based on the assumption that the undulations set in as a stationary instability. That is, the oscillation rate  $\omega$  in our ansatz Eq. (3.46) vanishes at onset. In this section we will discuss the situation for nonzero  $\omega$  and find that our previous assumption was justified. In our linear analysis enters now (for the first time in this work) the mass density of the system, which we will choose to be equal to unity,  $\rho = 1$ . Note that any other density will renormalize the frequency and will not change the results of this section.

The search for a possible oscillatory instability is slightly different from the procedure used in the stationary case. The solvability condition of the linearized set of equations determines both the neutral curve and the frequency along this curve. When searching for such a solution we scanned approximately the same parameter space as used for Figs. 3.2 – 3.4. Since the frequency tends to zero when the oscillatory neutral curve gets close to the stationary one, we concentrated on the frequency range  $0 \leq \omega \leq 2$  and checked in some cases for higher frequencies.

It turned out that only in cases when the director field is very weakly coupled to the layering a neutral curve for an oscillatory instability is possible. This weak coupling manifests itself in small  $B_1$  and  $\gamma_1$ , which is, in our set of dimensionless variables, equivalent to large  $B_0$  and  $\nu_i$ . Oscillatory neutral curves were only found for  $B_0 \gtrsim 100$  or  $\nu_i \gtrsim 1$ . In all investigated cases an oscillatory neutral curve is either absent or lies above the neutral curve for a stationary instability. When an oscillatory neutral curve is possible, it ends in the points where it meets the stationary neutral curve (see Fig. 4.1). The corresponding frequency approaches zero in the end points of the oscillatory neutral curve. If we ignore for the moment the stationary neutral curve and consider only the

---

<sup>1</sup>Chapters 2 to 4 are based on Refs. [2, 3, 4]

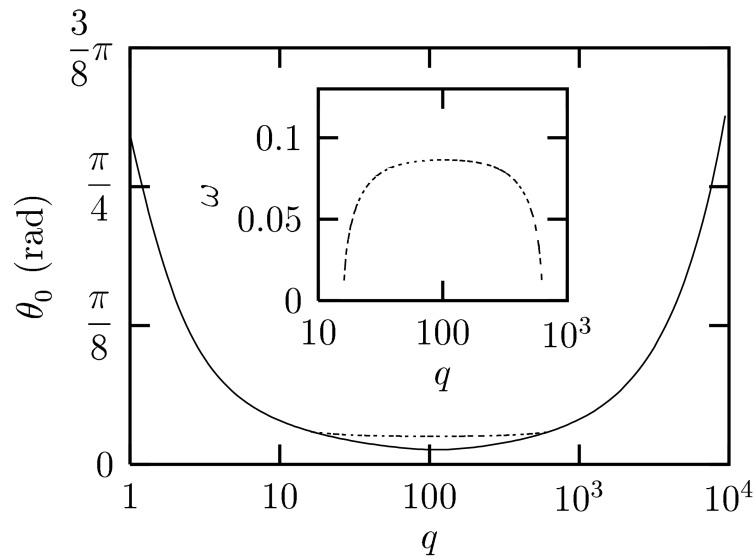


**Figure 4.1:** In most parts of the scanned parameter space no possibility for an oscillatory instability was found. If the director field is only very weakly coupled to the layering (in this plot we used  $B_0 = 200$  and  $\nu_i = 0.4$ ) a neutral curve for an oscillatory instability ( - - - ) appears above the stationary neutral curve ( ——— ). Note that the critical wave vectors are close to each other for both oscillatory and stationary instability. The inset shows the frequency along the neutral curve.

oscillatory instability, the corresponding critical values are found to be rather close to the stationary ones and to approach them the weaker the coupling between the director and the layers becomes. To summarize, an oscillatory instability was not found to be possible at threshold in all investigated cases and seems to be extremely unlikely to occur within a linear theory.

## 4.2 Effect of other external fields

In the remarks to Chapter 2 on page 20, we have pointed out that a shear field is only one possibility among others to induce a biaxiality in a smectic- $A$ -like system. In this section we will explore the influence of other fields on smectic- $A$  liquid crystals in our extended description, namely, a magnetic field. The purpose of this section is to demonstrate the similarities to the effects of a shear field.

In Sec. 1.3, we have shown that nematic and smectic- $A$  liquid crystals show characteristic instabilities under the influence of a magnetic field. If the magnetic anisotropy is positive, the nematic director tilts towards the field direction in a Freedericksz transition and the smectic layers start to undulate in a Helfrich-Hurault instability. For a typical low molecular weight liquid crystal, the critical field for a Freedericksz transition is much smaller than that for the Helfrich-Hurault instability.

To include the effect of a magnetic field in our extended model it suffices to couple only

the director to the external field and the neglect a Helfrich-Hurault type instability at much higher fields. Therefore, we have to extend our energy density by the magnetic term<sup>2</sup>

$$\epsilon_{mag} = -\frac{1}{2}\chi_a \left( \hat{n} \cdot \vec{H} \right)^2 \quad (\text{cgs}), \quad (4.1a)$$

$$\epsilon_{mag} = -\frac{1}{2}\mu_0\chi_a \left( \hat{n} \cdot \vec{H} \right)^2 \quad (\text{SI}), \quad (4.1b)$$

with the anisotropic part of the magnetic susceptibility  $\chi_a$  (which is typically *positive*, see, *e.g.*, Ref. [26]) and the magnetic field strength  $\vec{H}$ . Generally this term will lead to a spatially homogeneous torque on the director. In our model the homeotropic alignment of the director is only due to its coupling to the layer normal  $\hat{p}$ . Consequently we expect a spatially homogeneous tilt of the director which is given by the balance between the terms of the energy density which reflect the torques on the director. When we consider a situation where only the director is influenced by the field, the field induced tilt angle is given as the solution to the equations

$$\frac{\partial}{\partial \theta} \left[ -\frac{1}{2}\chi_a \left( \hat{n} \cdot \vec{H} \right)^2 + \frac{1}{2}B_1(\hat{n} \times \hat{p})^2 + \frac{1}{2}B_0(1 - \cos \theta)^2 \right] = 0 \quad (\text{cgs}), \quad (4.2a)$$

$$\frac{\partial}{\partial \theta} \left[ -\frac{1}{2}\mu_0\chi_a \left( \hat{n} \cdot \vec{H} \right)^2 + \frac{1}{2}B_1(\hat{n} \times \hat{p})^2 + \frac{1}{2}B_0(1 - \cos \theta)^2 \right] = 0 \quad (\text{SI}). \quad (4.2b)$$

For small  $\theta$ , the term proportional to  $B_0$  is of higher order than the other terms in these equations. We will drop it for this reason in the following considerations. If the external magnetic field encloses some angle  $\theta_h$  with the layer normal  $\hat{p}$ , the magnetically induced director tilt  $\theta_0$  is given by

$$\tan 2\theta_0 = \frac{\chi_a H^2 \sin 2\theta_h}{B_1 + \chi_a H^2 \cos 2\theta_h} \quad (\text{cgs}), \quad (4.3a)$$

$$\tan 2\theta_0 = \frac{\mu_0\chi_a H^2 \sin 2\theta_h}{B_1 + \mu_0\chi_a H^2 \cos 2\theta_h} \quad (\text{SI}), \quad (4.3b)$$

with  $|\vec{H}| = H$ . For small values of the characteristic ratio  $h_B = \chi_a H^2/B_1$  in cgs-units (or  $h_B = \mu_0\chi_a H^2/B_1$  in SI-units) the field induced director tilt is maximum for an angle of  $45^\circ$  between the layer normal and the external field (see Fig. 4.2). To estimate reasonable values of the characteristic ratio we set the magnetic field to the critical field for the Helfrich-Hurault instability for a typical low molecular weight liquid crystal with a sample thickness of  $100 \mu\text{m}$  (see Sec. 1.3.2 and Ref. [26] for details). Table 4.1 summarizes the results.<sup>3</sup> From these typical values we conclude that for all low molecular

<sup>2</sup>Differently to the previous chapters the following relations differ slightly depending on the system of units used (SI or cgs). For this reason we give both possibilities.

<sup>3</sup>The fundamental relation between magnetic induction  $\vec{B}$ , magnetic field  $\vec{H}$  and magnetization  $\vec{M}$  reads in cgs-units  $\vec{B} = \vec{H} + 4\pi\vec{M}$  and in SI-units  $\vec{B} = \mu_0(\vec{H} + \vec{M})$ . In the case of linear materials laws  $\vec{M} = \underline{\chi}^{\text{cgs}} \cdot \vec{H}$  and  $\vec{M} = \underline{\chi}^{\text{SI}} \cdot \vec{H}$ , these relations lead to  $4\pi\chi_a^{\text{cgs}} = \chi_a^{\text{SI}}$ .

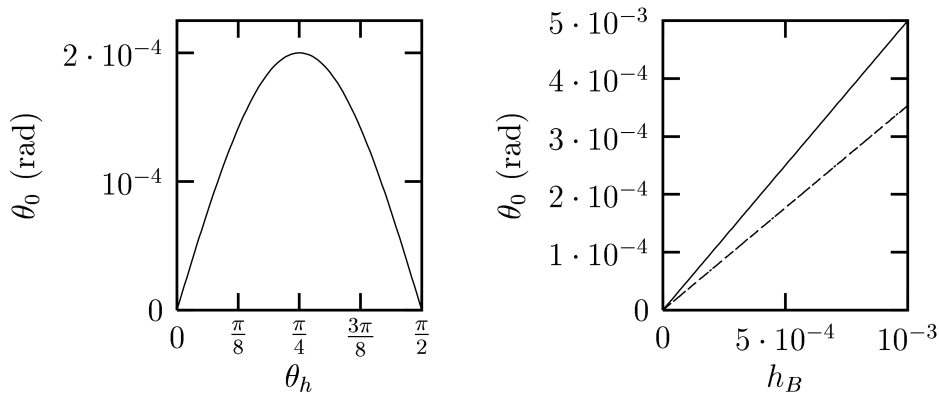


**Figure 4.2:** The field induced director tilt is maximum for fields which enclose an angle of about  $45^\circ$  with the layer normal. In the left plot we illustrate the dependence of the tilt angle on the angle between  $\vec{H}$  and  $\hat{p}$  (for  $h_B = 4 \cdot 10^{-3}$ ). Note that the curve is fully described by the linearized equations. The right plot depicts the influence of the characteristic ratio for various angles [solid line (—):  $\theta_h = \pi/8$ , dashed line (---):  $\theta_h = \pi/4$ , dotted line (.....):  $\theta_h = 3\pi/8$ ]. For the value of  $h_B$  used in this plot  $\theta_h = \pi/8$  and  $\theta_h = 3\pi/8$  result in identical curves.

	cgs	SI
$H_c$	$2 \cdot 10^5$ Oe	$2 \cdot 10^7$ A m $^{-1}$
$\chi_a$	$10^{-7}$	$10^{-6}$
$h_B$	$\sim 4 \cdot 10^{-3}$	$\sim 4 \cdot 10^{-3}$
$\theta_0^{\max}$	$\sim 2 \cdot 10^{-3}$ rad	$\sim 2 \cdot 10^{-3}$ rad

**Table 4.1:** Typical values for the parameters entering the field induced director tilt

weight liquid crystals we can replace Eqs. (4.3a) and (4.3b) by their linearized versions:

$$\theta_0 = \frac{\chi_a H^2}{2B_1} \sin 2\theta_h \quad (\text{cgs}), \quad (4.4a)$$

$$\theta_0 = \frac{\mu_0 \chi_a H^2}{2B_1} \sin 2\theta_h \quad (\text{SI}). \quad (4.4b)$$

### Remark

The typical tilt angle derived above might seem small. Nevertheless, we believe that it should be measurable for the following reasons. First, the typical anisotropy of the refractive index of low molecular weight liquid crystals is rather large ( $\Delta n \sim 0.1$ ). And secondly, birefringence measurements can detect even very small values of  $\Delta n$  (in Ref. [82] Martinoty and Bader report measurements of  $\Delta n \sim 10^{-7}$ ). For a field of  $H = 60$  kOe we expect  $\theta_0 \sim 2 \cdot 10^{-4}$ , or  $\Delta n \sim 2 \cdot 10^{-5}$ , which is in the measurable regime.

### 4.3 Comparison to experiments

In the previous chapters we have shown that the inclusion of the director of the underlying nematic order in the description of a smectic-*A*-like system leads to some important features. In general, the behavior of the director under external fields differs from the behavior of the layer normal. In this work we only discussed the effect of a velocity gradient in detail. But, as we have shown in the previous section, similar effects also result under the influence of other external fields. The key results of our theoretical treatment are a tilt of the director, which is proportional to the shear rate, and an undulation instability which sets in above a threshold value of the tilt angle (or equivalently the shear rate).

Both predictions are in agreement with experimental observations. In the case of the shear induced director tilt, we know of no experiment which would allow a direct comparison to our theory. Since the director tilt creates a tendency of the layers to reduce their thickness (if they are allowed to do so), some works on the dependences of the layer thickness allow for an indirect comparison to our theory. For side-chain liquid crystalline polymers Noirez [93] observed a shear dependence of the layer thickness under steady shear conditions. In the parallel orientation the layer thickness is reduced by several percent with increasing shear. A detailed interpretation of this experiment might include effects beyond the present model, but clearly the observed effect is in agreement with our theory. Polis *et al.* [107] investigated the dependence of the layer thickness at constant shear rates for shear deformations up to 75%. Later Qiao *et al.* [108] considered a similar situation (also in diblock copolymers) with deformations up to 60%. In both studies, the authors found a decreasing layer spacing with increasing shear rate and increasing strain. But in these two experiments the layer spacing *vs.* strain curves do not reach a plateau so a direct comparison to our model is not possible. Nevertheless, both experimental results are clearly compatible with our prediction.

To our knowledge, two groups have investigated the destabilization of a parallel alignment in detail. Both studies were performed in lyotropic systems in which the final state are multi-lamellar vesicles. First investigations were done by Schmidt and coworkers [85] and later Richtering and coworkers performed a detailed study on the transition [88, 142]. Using a number of different experimental techniques Richtering and coworkers identified several states within the transition from parallel lamellae to multi-lamellar vesicles. The first state after the destabilization of the parallel orientation is a two dimensional structure which shows no variation along the flow direction. They identify these structures to be either multi-lamellar cylinders or undulating lamellae. The characteristic length of these structures (diameter of the multi-lamellar cylinders) is found to be  $\approx 7 \mu\text{m}$ .

In addition to the obvious qualitative agreement of these experimental results, we now make a semi-quantitative comparison to our theoretical results. For this purpose we make a number of assumptions about the material parameters. As we have shown in Sec. 3.4, the different approaches cause only small variations in the critical wave number. For this estimate it suffices to use the critical wave number obtained in our earlier work [see Eq. (B.5)]. For lyotropic liquid crystals it is known [51, 87] that the elastic constants

can be approximately expressed by

$$K = \frac{\kappa}{l} \quad (4.5)$$

and

$$B = \frac{9}{64} \pi^2 \frac{(k_B T)^2}{\kappa} \frac{l}{(l - \delta)^4}, \quad (4.6)$$

where  $\kappa = \alpha_\kappa k_B T$  is the bending modulus of a single bilayer,  $l$  the layer spacing,  $\delta$  the bilayer thickness,  $k_B$  the Boltzmann constant,  $T$  the temperature and  $\alpha_\kappa$  a dimensionless number of order of unity. With these relations we can estimate the critical wave vector for a sample of thickness  $d$  using Eq. (B.5):

$$q_c^2 \approx \frac{3\pi^2}{8\alpha_\kappa d} \frac{l}{(l - \delta)^2}. \quad (4.7)$$

The parameters of the experiment by Zipfel *et al.* [142] are:  $d = 1$  mm,  $\delta = 2.65$  nm,  $l = 6.3$  nm, and  $\alpha_\kappa = 1.8$  [124, 142]. On this basis we estimate the critical wavelength to be of the order of

$$\lambda_c \approx 6.4 \mu\text{m} \quad (4.8)$$

Zipfel *et al.* [142] observed a vesicle diameter of  $7 \mu\text{m}$ , which is clearly compatible with our calculation. We note that this estimate supposes that the experiments are done in the hydrodynamic regime.

After the destabilization of the parallel orientation the experiments of Richtering and coworkers show a variety of further effects which are beyond the scope of the present approach and pose a number of interesting questions. So further investigations on these points are desirable.

To conclude, the presented model is compatible with the experimental results in lyotropic systems and block copolymers. But for many systems the material parameters entering in the theoretical approach are not known, or can only be estimated. For this reason a detailed comparison between theory and experiment is not feasible yet at the present state.



---

## Chapter 5

# Comparison between the analytic theory and molecular dynamics simulations<sup>1</sup>

Besides the direct comparison to experimental data, there is a second possibility to test the prediction of our theoretical approach: comparison to molecular dynamics simulations of a model system. In this chapter we will explore the possibilities of such a comparison and give the main results.

### 5.1 Molecular dynamics simulations: basics

As an introduction to this chapter we will review the basic ideas of molecular dynamics simulations. For a more detailed description of the method we refer the reader to the general literature about molecular dynamics simulations like books by Frenkel and Smit [40] and Allen and Tildesley [1] or the original works in which the simulation model system has been developed [46, 47, 86, 116, 118].

The basic idea of molecular dynamics simulations is to model a physical system by a number of distinct particles  $N$  which typically interact within the limits of classical mechanics.<sup>2</sup> For all particles the positions and the velocity vectors are known, and macroscopic quantities can be calculated by a suitable averaging of the microscopic quantities. Depending on the initial conditions the averaged quantities only represent reliable macroscopic quantities after a certain equilibration time of the system. The

---

<sup>1</sup>This chapter is based on the results of a collaboration with simulation physicists from the Max-Planck-Institute for Polymer Research in Mainz (MPIP). Besides the author, Thomas Soddemann and Hongxia Guo (both simulation physicists) were strongly involved in this collaboration. The simulations presented in this chapter were performed at the MPIP. The results of this chapter will be published in Ref. [117].

<sup>2</sup>If wanted the inclusion of quantum mechanical effects is also possible, see, *e.g.*, [7, 12]. For the present simulations there is no need to include quantum mechanical effects.

evolution of the microscopic quantities is given by the integration of Newton's second law.<sup>3</sup>

$$m_i \frac{d^2}{dt^2} \vec{r}_i = \sum_{j \neq i} \vec{F}_{ij}^C = -\nabla \sum_{j \neq i} U_{ij}, \quad (5.1)$$

where  $m_i$  are the particle masses,  $\vec{F}_{ij}^C$  are the interaction forces (between particle  $i$  and  $j$ ),  $U_{ij}$  the corresponding interaction potential and the sum goes over all particles  $j \neq i$ . As can be seen in Eq. (5.1), only two body interaction are taken into account, three and more body interactions are neglected.

The notion "particle" does not necessarily mean an atom or molecule, it also can correspond to a group of atoms. For example, polymer chains are often described by chains of several particles which each represent several monomer units of the polymer chain [33, 44]. The choice of the simulation "particles" depends on the length and time scales of interest: Taking every atom as a "particle" gives insight in short length scales of  $\sim 1 \text{ \AA}$  but only short times can be simulated. For longer simulated times a coarse grained model has to be used. This means several atoms in a molecule (*e.g.*, in a polymer chain) are treated as one "particle". And the interactions of these particles are some effective interactions which are often deduced phenomenologically.

To get simulation results which represent the bulk properties of the model system, it is essential to have a *large* number of particles. Due to this large number of particles numerical efficiency is most important in the implementation of the simulation. Out of the large variety of methods in this area we only pick out those which are of importance in the simulations used in this chapter. Namely, we will comment on the integration scheme, the thermostating of the system, the implementation of the shear on the simulated system and the model system used to mimic layered liquids.

### 5.1.1 Integration scheme

One major issue in performing simulations is the interest to have long simulated times. For computational efficiency the second order Eq. (5.1) is split into two first order equations by introducing the linear momenta of the particles as additional free variables. The integration of these equations consists of two parts: the force calculation and the actual integration. The force calculation is typically the most time consuming part since it involves the calculation of the particle distances. The integration of the equation of motion is done using the Verlet integration scheme or its variants [40, 122]. For the simulation we use in this chapter the integration scheme is based on the so-called velocity Verlet algorithm (a leap-frog variant of the original algorithm).<sup>4</sup> In this algorithm, first, the particle momenta  $\vec{p}_i$  are calculated at half the time step, using the forces

---

<sup>3</sup>Note that this equation of motion contains only conservative forces, because it is valid on the microscopic scale of a single particle.

<sup>4</sup>Due to the coupling to a heat bath this scheme will be modified in the next section, we present it here to give a better comparison.

$\vec{F}_i = \sum_{j \neq i} \vec{F}_{ij}$  at the original time.

$$\vec{p}_i(t + \Delta t/2) = \vec{p}_i(t) + \frac{\Delta t}{2} \vec{F}_i(t) \quad (5.2a)$$

These are then used to successively calculate the new particle positions  $\vec{r}_i$  and the new forces  $\vec{F}_i$ .

$$\vec{r}_i(t + \Delta t) = \vec{r}_i(t) + \frac{\Delta t}{m_i} \vec{p}_i(t + \Delta t/2) + \frac{(\Delta t)^2}{2m_i} \vec{F}_i(t) \quad (5.2b)$$

$$\vec{F}_i(t + \Delta t) = \vec{F}_i(\{r_i(t + \Delta t)\}, \{\vec{p}_i(t + \Delta t/2)\}) \quad (5.2c)$$

And finally the momenta are updated to the next time step.

$$\vec{p}_i(t + \Delta t) = \vec{p}_i(t + \Delta t/2) + \frac{\Delta t}{2} \vec{F}_i(t + \Delta t) \quad (5.2d)$$

This integration scheme is not particularly accurate in time, but it shows little long term drift in the total energy (although short term energy conservation is only fair) and conserves time reversibility.

### 5.1.2 Coupling to a heat bath

The integration scheme described above belongs, thermodynamically speaking, to the micro-canonical ensemble, where the particle number  $N$ , the volume of the system  $V$  and its energy  $E$  are kept constant. For practical reasons one would prefer to perform the simulations in the canonical ensemble, *i.e.*, to keep  $N$ ,  $V$  and the temperature  $T$  constant. This can be achieved by coupling the simulated system to a heat bath. The simplest way to couple the system to a heat bath is to add (phenomenological) viscous damping and stochastic driving terms to the equation of motion (5.1). The strength of these terms must be related to each other by the fluctuation dissipation theorem. In static situations one can compute the temperature of the simulated system using the absolute particle velocities [44]. But this is *not* possible for situations with non-vanishing macroscopic velocities like in shear cells.<sup>5</sup>

A suitable thermostat was first constructed for colloidal suspension with hydrodynamic interactions [54, 61] in a simulation technique called dissipative particle dynamics (DPD). The DPD thermostat has the main advantage that the additional forces are calculated from the particle distances  $\vec{r}_{ij} = \vec{r}_i - \vec{r}_j$  and relative velocities  $\vec{v}_{ij} = \vec{v}_i - \vec{v}_j$  and not from the absolute particle positions  $\vec{r}_i$  and velocities  $\vec{v}_i$ . For this reason the DPD thermostat is Galilei invariant and conserves linear and angular momentum. Later Español and Warren [32] and Groot and Warren [45] have related the DPD method to the dissipation fluctuation theorem and explored some applications.

---

<sup>5</sup>The notion “macroscopic” in this chapter stands for an average over many particles. At the end of this chapter we will show that the simulated system shows indeed many features which can be described by a macroscopic hydrodynamic theory.

To implement the DPD thermostat one adds to the particle-particle interaction in Eq. (5.1) a dissipative damping and a stochastic driving [32, 45]:

$$\vec{F}_i = \sum_{j \neq i} \left( \vec{F}_{ij}^C + \vec{F}_{ij}^D + \vec{F}_{ij}^R \right), \quad (5.3)$$

with the microscopic conservative particle-particle interactions  $F_{ij}^C$  (see above), the dissipative damping  $F_{ij}^D$  and the stochastic driving  $F_{ij}^R$ . The latter two are of the form

$$F_{ij}^D = -\Gamma \omega_D(r_{ij}) (\hat{e}_{ij} \cdot \vec{v}_{ij}) \hat{e}_{ij}, \quad (5.4)$$

$$F_{ij}^R = \zeta \omega_R(r_{ij}) \vartheta_{ij} \hat{e}_{ij}, \quad (5.5)$$

with the strength of the dissipative and stochastic force  $\Gamma$  and  $\zeta$ , respectively, the weight functions  $\omega_D(r)$  and  $\omega_R(r)$ , the unit vector of the relative coordinate  $\hat{e}_{ij} = \vec{r}_{ij}/|\vec{r}_{ij}|$ , and the Gaussian noise term  $\vartheta_{ij} = \vartheta_{ji}$ . To fulfill the fluctuation dissipation theorem, the weight functions and the strength of the forces must be related [32]. Typically one uses

$$\omega_D(r) = [\omega_R(r)]^2 = \begin{cases} (r_c - r) & r < r_c \\ 0 & r \geq r_c \end{cases} \quad (5.6)$$

$$\zeta^2 = 2\Gamma k_B T, \quad (5.7)$$

with the range of the forces  $r_c$  and the Boltzmann constant  $k_B$ . Since the forces now depend on the velocities, the integration scheme given in Eqs. (5.2) has to be modified, a suitable version is [1, 45]:

$$\vec{r}_i(t + \Delta t) = \vec{r}_i(t) + \frac{\Delta t}{m_i} \vec{p}_i(t) + \frac{1}{2} (\Delta t)^2 F_i(t) \quad (5.8a)$$

$$\vec{p}_i(t + \Delta t) = \vec{p}_i(t) + \Lambda \Delta t \vec{F}_i(t) \quad (5.8b)$$

$$\vec{F}_i(t + \Delta t) = \vec{F}_i(\{r_i(t + \Delta t)\}, \{\vec{p}_i(t + \Delta t)\}) \quad (5.8c)$$

$$\vec{p}_i(t + \Delta t) = \vec{p}_i(t) + \frac{\Delta t}{2} [\vec{F}_i(t) + \vec{F}_i(t + \Delta t)]. \quad (5.8d)$$

Note that this integration scheme with  $\Lambda = 1/2$  is equivalent to Eqs. (5.2). One can empirically adjust  $\Lambda$  to allow for somewhat larger time steps. In the present case the time step was limited by the hard core part of the particle-particle interaction, so  $\Lambda = 1/2$  is a good choice.

### 5.1.3 Shear algorithm

Shear can be applied to a simulation system by various ways. For the present simulations, one key requirement for the shear algorithm was, that it does not predefine the shear profile, *i.e.*, the actual shear profile is a result of the simulation and may vary with time and space (*e.g.*, due to defects). Besides this physical requirement one must ensure that the shear algorithm conserves the global linear momentum of the system. An algorithm which fulfills these requirements has been constructed by Müller-Plathe [86].

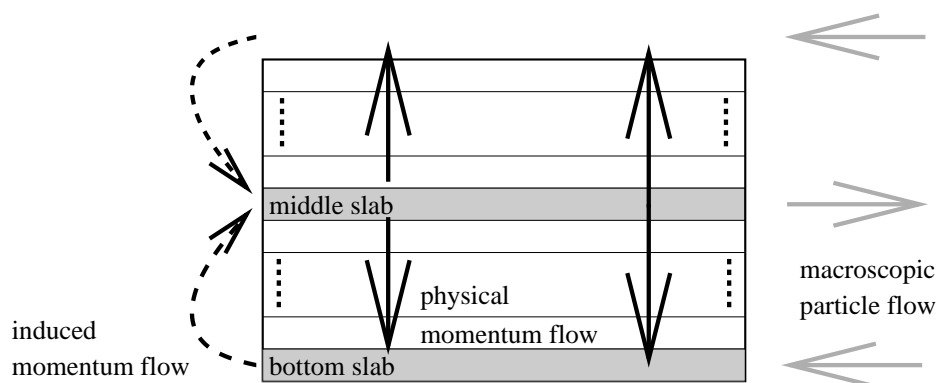


**Figure 5.1:** Summary of Müller-Plathe’s shear algorithm. See text for details.

In Fig. 5.1 we present a summary of Müller-Plates algorithm. It starts with a simulation box with no macroscopic flow. Then the box is divided into a number of slabs. The aim of the algorithm is to create a macroscopic flow in the bottom and top slab in one direction and in the middle slab in the other direction (gray arrows).<sup>6</sup> The macroscopic flow is induced by a non-physical move in the simulation. One looks in the middle and bottom slab for the particles which move most against the intended direction and exchanges their momenta in the flow direction (dashed arrows). Due to this move the middle slab and the bottom slab get an additional momentum in the intended flow direction. This momentum exchange can be repeated periodically until the desired shear rate is achieved. This algorithm leads to a back-flow of momentum through the system (black arrows), from which the viscosity can be measured directly. Obviously, this method of applying shear does not prefer any particular shear profile. As Soddemann [116] has shown both linear and non-linear flow profiles are possible.

#### 5.1.4 Model system

For the simulation of layered liquids Soddemann *et al.* [116, 118] introduced the following model. In a number of publications this model has been proven to show many interesting features [46, 47, 118].<sup>7</sup>

As in most MD simulations all particles exhibit a hard core which provides an effective excluded volume. A convenient choice for this is a Lennard-Jones (LJ) potential that is

<sup>6</sup>Due to the periodic boundary conditions, the top and bottom slab must move in the same direction. Consequently, the upper half and the lower half of the simulation box must be analyzed separately. One could overcome this inconvenience by using shifted periodic (“Lee-Edwards”) boundary conditions.

<sup>7</sup>The original model [118] was constructed with dimeric molecules. However, later [46, 47] tetrameric molecules were used to reduce the inter-layer diffusion.

truncated at the minimum, and shifted:<sup>8</sup>

$$U_{LJ} = \begin{cases} 4\epsilon \left[ \left(\frac{\sigma}{r}\right)^{12} - \left(\frac{\sigma}{r}\right)^6 + \frac{1}{4} \right] & r \leq 2^{1/6}\sigma \\ 0 & r \geq 2^{1/6}\sigma \end{cases} \quad (5.9)$$

The parameters  $\epsilon$  and  $\sigma$  give the scales for energy and length. Without loss of generality they can be chose to unity in this system.

From polymer simulations it is known that it is computationally efficient to link the dimers *via* an-harmonic FENE (“finitely extendible nonlinear elastic”) springs with spring constant  $k$  and maximum extension  $R_0$ :

$$U_{FENE} = \begin{cases} -\frac{1}{2}kR_0^2 \ln \left[ 1 - \left(\frac{r}{R_0}\right)^2 \right] & r < R_0 \\ \infty & r \geq R_0 \end{cases} . \quad (5.10)$$

The parameters for the FENE potential are chosen to be  $k = 5$  and  $R_0 = 2.0$ . These parameters ensure that the particle-particle distance is similar between bonded and non-bonded particles.<sup>9</sup>

In order to be able to enhance the bias toward phase separation like particles have in addition to their hard core interaction an attractive tail in their potential. This attractive tail is known to drive phase separation and various ordered structures such as the lamellar phase can be observed for different kinds of model amphiphiles. Like particle interaction are simulated by adding a cosine wave to a hard core Lennard Jones which is given by

$$U_{LJcos} = \begin{cases} 4 \left[ \left(\frac{1}{r}\right)^{12} - \left(\frac{1}{r}\right)^6 + \frac{1}{4} \right] - \Pi & r \leq 2^{1/6} \\ \frac{1}{2}\Pi [\cos(\alpha r^2 + \beta) - 1] & 2^{1/6} \leq r \leq 1.5 \\ 0 & r \geq 1.5, \end{cases} \quad (5.11)$$

where  $\alpha$  and  $\beta$  are determined as the solutions of the linear set of equations

$$2^{1/3}\alpha + \beta = \pi, \quad (5.12)$$

$$2.25\alpha + \beta = 2\pi, \quad (5.13)$$

*i.e.*,  $\alpha = 3.1730728678$  and  $\beta = -0.85622864544$ . The parameter  $\Pi$  measures the depth of the attractive tail. Since the strength of the thermal noise (see above) is typically

---

<sup>8</sup>The dimensionless units in the simulation (“Lennard-Jones” units) are not directly related to the units used in the analytic work so far. They are chosen for numerical efficiency. Later in this chapter we will make the connection to the analytic work.

<sup>9</sup>This detail allows Monte Carlo type simulation for the investigation of phase transitions in the simulated system [118].

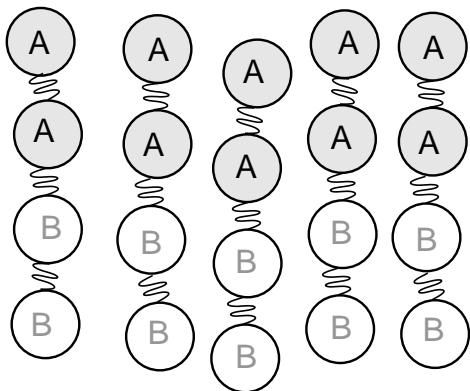


**Figure 5.2:** A sketch of the simulated tetrameric molecules. All spheres are of equal size, have the same mass and are connected by the same spring. See text for more details.

kept constant in the simulations,  $\Pi$  can be interpreted as the inverse temperature of the simulated system.

With this set of potentials a dense system of  $A_2B_2$  tetramers is simulated *via* the molecular dynamics method in the  $NVT$  ensemble (using the DPD thermostat described above). The A and B beads of one molecule are connected with a FENE spring analog to previous studies on dimer systems [116, 118]. The attraction according to Eq. (5.11) acts only between like monomers which are not connected with a spring. These tetramers serve as a coarse grained, mesoscopic model of diblock copolymers or small surfactants.

## 5.2 Results of the molecular dynamics simulations

As initial configuration 36864 molecules have been prepared and equilibrated in a lamellar phase in a parallel orientation. This tetrameric system is, with the exception of the molecular size, similar to the systems discussed in Refs. [47, 116]. Similarly to the dimeric system [116, 118], this system exhibits a first order transition from a disordered to a lamellar phase at a potential depth of  $\Pi = 0.78$ . No other phase has been found in this system. For the simulations used in this chapter, a potential depth of  $\Pi = 1.1$  was applied, *i.e.*, all simulations were done in the smectic- $A$  phase of the system. Note that this smectic- $A$  phase is a bilayer phase, like the lamellar phase of block copolymers. The transition into the smectic- $A$  phase in this model system seems to be driven by the packing of the molecules as well as the attractive and repulsive interactions between the different parts in the molecules.

The orientation of the exerted shear flow is sketched in Fig. 5.3 where the arrows indicate the direction of maximum flow. Note that due to the periodic boundary conditions the bottom and its periodic image above the top are equal, while the middle is moving in the opposite direction. Both, the upper and the lower half of the simulated system correspond on their own to the system considered in the analytic theory developed in the previous chapters and applied to the simulated system in Sec. 5.3. The flow direction lies along the  $x$  axis and the shear gradient points along the  $z$  axis.

Starting with the system at rest, the shear rate  $\dot{\gamma}$  was successively increased in steps with a maximum step of  $\Delta\dot{\gamma} = 0.002$  up to a maximal shear rate of  $\dot{\gamma} = 0.025$ . The

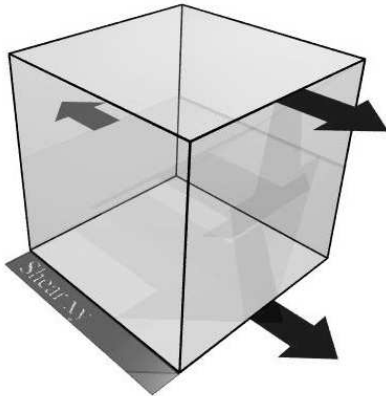


**Figure 5.3:** Orientation of the shear flow in the simulation. The maximum flow directions are sketched by the arrows. The shear at the bottom is equal to the periodic image above the top of the box. The middle slab is moving in opposite direction. As in the analytic part (see Fig. 2.1 on page 16), the  $x$  axis is along the flow direction, the  $y$  axis along the neutral direction and the  $z$  axis along the shear gradient of the flow.

steady state configuration of one shear rate was always used as the initial configurations for the next step. In all steady state situations, the shear profile turns out to be linear, *i.e.*, the shear rate  $\dot{\gamma}$  is constant throughout the simulation box.

Figure 5.4 shows the shear rate  $\dot{\gamma}$  as a function of the director tilt angle  $\theta_0$ . We exchanged the axes due to practical reasons: A fit to Eq. (3.49) is much easier to perform, if one considers  $\dot{\gamma}(\theta_0)$  instead of  $\theta_0(\dot{\gamma})$ . Differently to the standard description of smectic-A liquid crystals, but in agreement to the extended description developed in this work, the tilting angle increases with increasing shear rate. A more detailed discussion will be given in the next section. We note that up to a shear rate of  $\dot{\gamma} = 0.01$  the simulated system shows an unperturbed parallel alignment of the layers and the direction tilt is the only response of the system to the applied shear.

The situation changes for shear rates larger than  $\dot{\gamma} = 0.01$ : The simulation results show undulating lamellae, where the wave vector of the undulations points along the vorticity direction of the flow. Figure 5.5 shows a simulation snapshot of the system at a strain rate of  $\dot{\gamma} = 0.015$  which clearly exhibits a system with undulations in vorticity direction (left to right). Once formed, these undulations show no time dependence and their amplitude does not vary along the  $z$  axis. A simple measure of the undulation amplitude is the director component in the  $y$  direction  $n_y$  (parallel to the wave vector of the undulations). As a function of  $y$   $n_y$  follows the undulations of the layers. For this reason the amplitude of the undulations in  $n_y$  is taken as a measure for the amplitude of the layer undulations.<sup>10</sup> Fig. 5.6 shows the amplitude of  $n_y$  undulations as a function of the shear rate. At a strain rate of  $\dot{\gamma} = 0.011$  the amplitude increases until the layers reorient at  $\dot{\gamma} > 0.025$  into a perpendicular orientation.

Additionally to the above describe shear “experiment”, also a dilation “experiment” was performed. The major aim of this second experiment was to have an independent way of measuring the material parameters of the system. To dilate the system, its size in the  $z$

<sup>10</sup>A direct measure of the layer displacement would be numerically much more demanding, since the raw data available are the coordinates of all particles. From these coordinates one first would have to identify the layers.



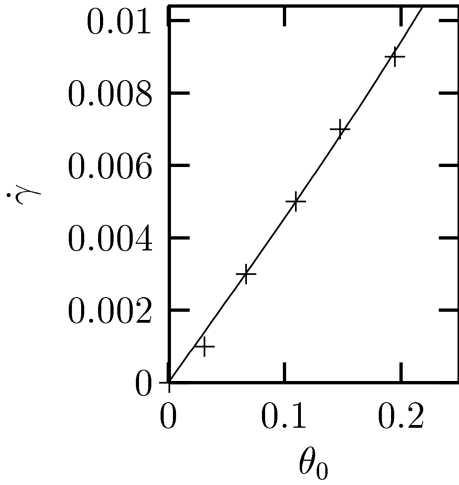


**Figure 5.4:** Strain rate as a function of the tilt angle. This peculiar form of presenting the data has been chosen in order to facilitate a direct comparison with the theory, especially Eq. (3.49). The solid line is a fit of this equation to the data (see Sec. 5.3 for more details).

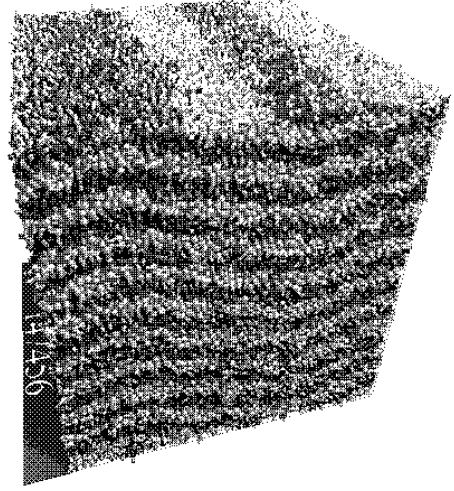


**Figure 5.5:** Undulations in the simulated model system. At a strain rate of  $\dot{\gamma} = 0.015$ , clearly, undulations have developed. As predicted in the theory, undulations in the vorticity direction are present. Note that the undulation amplitudes do not change along the  $z$  axis.

direction was increased, while the lateral dimensions were kept constant. At low dilation no effect of the stretching is observable, beyond a certain percentage of elongation of the simulation box undulations of the layers set in. The undulation amplitude can be measured in the same way as in the case of shear and the results are shown in Fig. 5.7. For low stretching the measured undulation amplitude is due to thermal noise. For  $\varepsilon \gtrsim 1.9\%$  undulations appear. The amplitude of the undulations increases until roughly 3% dilation. Beyond 3% the layers of the non-isochoric dilated system become unstable and break apart.

## 5.3 Comparison analytic theory *vs.* simulations

### 5.3.1 Details of the analytic approach

We use the analytic theory described in Chapter 3 with some small modifications, which are due to the fact that the simulated system treats the boundaries in a different way than a typical experiment. The simulation algorithm uses periodic boundary conditions and allows particles to move through the upper and lower boundary, so there is no need for the undulation amplitude to vanish at the upper and lower boundaries of the simulation box. We assume this amplitude to be constant throughout the sample. As can be seen from Fig. 5.5, this is in good agreement to the simulation results. Only the

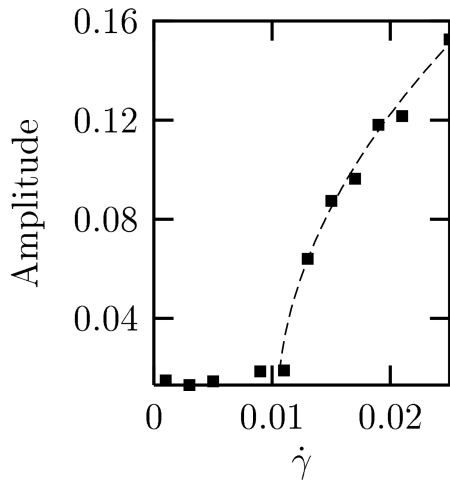


**Figure 5.6:** Amplitude of undulations due to shear. The amplitude of the undulations  $A$  is given as a function of the strain rate  $\dot{\gamma}$ . At a shear rate of  $\dot{\gamma} \approx 0.01$  undulations set in. The amplitude of these undulations grows continuously with increasing shear rate. The dashed line shows a fit to data points starting at  $\dot{\gamma} > 0.01$  and assuming a square root dependence of the amplitude above the undulation onset.

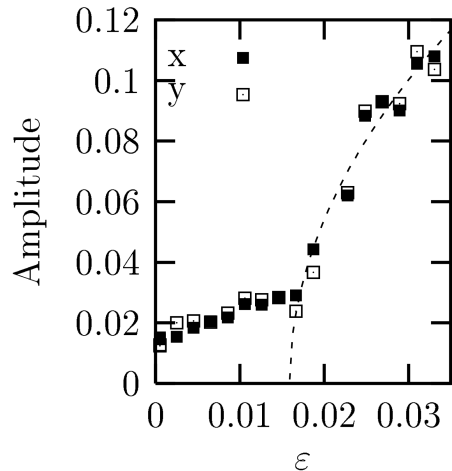


**Figure 5.7:** Amplitude of undulation as a function of the dilation  $\epsilon$ . For small  $\epsilon$  the amplitude is essentially due to the noise in the system. This changes at  $\epsilon \approx 0.019$ . The system starts to respond with undulations and the amplitude increases continuously until the layers break apart at values  $> 3\%$ . The dashed line (---) shows a fit to the data points assuming a square root dependence of the amplitude above onset (see text for a detailed discussion).

average of the flow component of the velocity field is controlled in the simulations. So we fix only the average  $v_x$  at the upper and lower boundary.

For the spatially homogeneous state the analysis is identical to Sec. 3.3.<sup>11</sup> The linear shear profile

$$\vec{v}_0 = \dot{\gamma} z \hat{e}_x \quad (3.48)$$

still solves Eq. (3.29) under the assumption that the boundaries have no orienting effect on the director. Under an applied shear, the director tilts in the flow-direction according to

$$\left( \frac{\lambda + 1}{2} - \lambda \sin^2(\theta_0) \right) \dot{\gamma} = \frac{B_1}{\gamma_1} \sin(\theta_0) \cos(\theta_0) + \frac{B_0}{\gamma_1} \sin(\theta_0) [1 - \cos(\theta_0)], \quad (3.49)$$

which takes for small shear rates the linearized form

<sup>11</sup>Here we only review the results and refer the reader to Chapter 3 for more details.

$$\theta_0 = \dot{\gamma} \frac{\gamma_1}{B_1} \frac{\lambda + 1}{2} + O(\theta_0^3). \quad (3.50)$$

For a better comparison it is useful to consider the evolution of the director after a step like start of the steady shear.

$$\dot{\gamma}(t) = \begin{cases} 0 & t < 0 \\ \dot{\gamma}_1 & t \geq 0, \end{cases} \quad (5.14)$$

with a constant  $\dot{\gamma}_1$ . Further we assume  $\dot{\gamma}_1$  to be small. So we can linearize Eq. (3.38) in the same way as for Eq. (3.50). Under these conditions the director tilt [in the limit of Eq. (3.50)] approaches its stationary value with a characteristic time  $\tau_1 = \gamma_1/B_1$ :

$$\theta(t) = \dot{\gamma} \frac{\gamma_1(\lambda + 1)}{2B_1} \left[ 1 - \exp\left(-t \frac{B_1}{\gamma_1}\right) \right]. \quad (5.15)$$

Following our linear stability analysis in Chapter 3 and making use of the boundary conditions discussed above, we proceed with an ansatz of the type

$$X_{1,i} \sim \begin{cases} \cos(q_s y) \\ \sin(q_s y) \end{cases}, \quad (5.16)$$

with the wave vector  $q_s$ .

The absence of a  $x$  and  $z$  dependence in this ansatz allows to reduce the number of unknown quantities. From the continuity equation (3.28) it follows directly that  $v_y$  must vanish. Similarly, the perturbations of the director tilt  $\theta_1$  and the pressure  $p_1$  can be shown to be equal to zero. Consequently, the full set of unknown quantities consists only of the director's azimuthal angle  $\phi_1$ , the layer displacement  $u_1$ , the velocity component along the shear flow  $v_{x,1}$  and along the unperturbed layer normal  $v_{z,1}$ . Furthermore, the set of governing equations can be reduced, because the permeation constant  $\lambda_p$  is typically very small (if not negligible).<sup>12</sup> Following Eq. (3.26),  $v_{z,1}$  is also small compared to  $u_1$  and can be neglected.

These arguments leave us with a minimal set of unknown quantities consisting of  $\phi_1$ ,  $u_1$  and  $v_{x,1}$ . As we show below, the results obtained with this minimal set differ only slightly from the result using the complete set (*i.e.*, including  $v_z$ ) discussed above.

The reduction in the number of unknown quantities causes also a significant reduction in the number of material parameters necessary for a detailed comparison between analytic theory and molecular dynamics simulations. To describe the onset of the instability, the set of material parameters consists of the material constants in the free energy  $B_0$ ,  $B_1$  and  $K$ , the flow alignment parameter  $\lambda$  and the viscosity constants  $\gamma_1$ ,  $\nu_2$  and  $\nu_3$ .

---

<sup>12</sup>At this point we cannot give a quantitative estimate of  $\lambda_p$  but it must be small because the inter-layer diffusion in the simulated system is several orders of magnitude slower than the intra-layer diffusion of the tetramers.

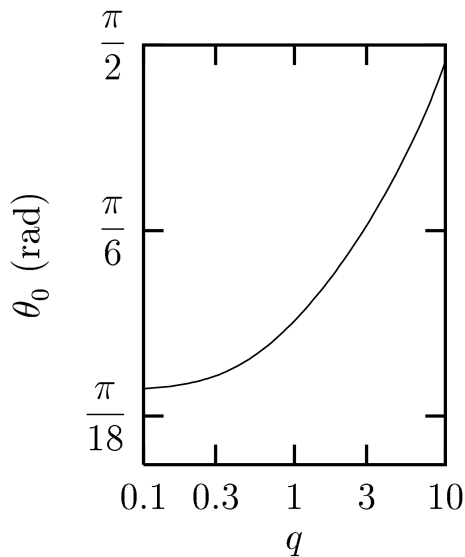


**Figure 5.8:** A typical neutral curve when using the boundary conditions for the simulated system. Clearly there is no intrinsic length scale associated with a minimum in the neutral curve. For this plot we used (in dimensionless units)  $B_0 = 10$ ,  $K = 0.085$ ,  $\lambda = 1$ ,  $\nu_i = 1$ , and  $\lambda_p = 0.001$ . The wave vector is rescaled such that  $q = 1$  corresponds to a wave length of the lateral box size.

In contrast to the undulation instability in an experimental system with rigid boundaries, in the simulated system there is no intrinsic hydrodynamic length scale (see Fig. 5.8). The only length scales present is given by the lateral size of the simulation box ( $L_x = L_y = L$ ), *i.e.*, the critical wave vector is always  $q_s = 1$  in dimensionless units (in Lennard-Jones units it would be  $q_s = 2\pi/L$ ).

In Figs. 5.9 to 5.11 we present the critical tilt angle above which the undulations set in as a function of the various material parameters. For a better comparison with the simulations we used typical values for the system of Sec. 5.3.2. If not specified otherwise the parameters were (in dimensionless units)  $B_0/B_1 = 6$ ,  $\frac{K}{B_1} \left(\frac{2\pi}{L}\right)^2 = 0.08$ ,  $\lambda = 0.8$ ,  $\nu_i/\gamma_1 = 0.05$  and  $\lambda_p/\gamma_1 = 10^{-3}$ . We do not present the corresponding plots for  $\nu_i$  and  $\lambda_p$ , because the critical tilt angle does not depend on these parameters over a wide range of the parameter values. In all plots the solid line corresponds to the full set of variables (as discussed above) and the dashed and dotted lines represent calculations when  $v_z$  is neglected (with the full viscosity tensor—dashed—and keeping only  $\nu_2$ —dotted).

To complete our theoretical part let us briefly come back to dilated smectic-*A* without shear. We follow the analysis of [16] and [28] (see also Sec. 1.3.1), but modify it with respect to the simulation boundary conditions, *i.e.*, we use an ansatz of the type (5.16). The neutral curve in this case is given by

$$\varepsilon = q^2 \frac{K}{B_0}. \quad (5.17)$$

where  $\varepsilon$  is the relative dilation. Since  $q$  is known in the simulated system we can directly conclude that the critical dilation is

$$\varepsilon_c = \left(\frac{2\pi}{L}\right)^2 \frac{K}{B_0}. \quad (5.18)$$

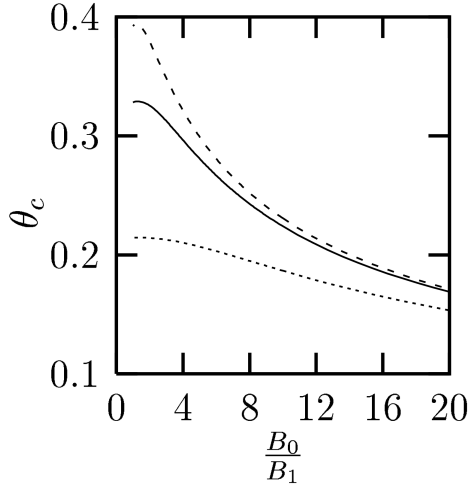


**Figure 5.9:** Critical tilt angle versus the dimensionless compression modulus of the layers (see text for further comments).

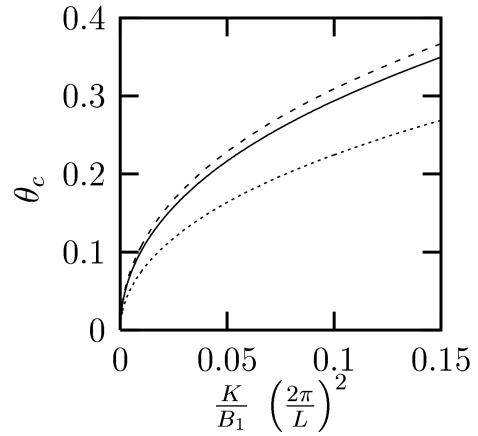


**Figure 5.10:** Critical tilt angle versus the dimensionless bending modulus of the layers.

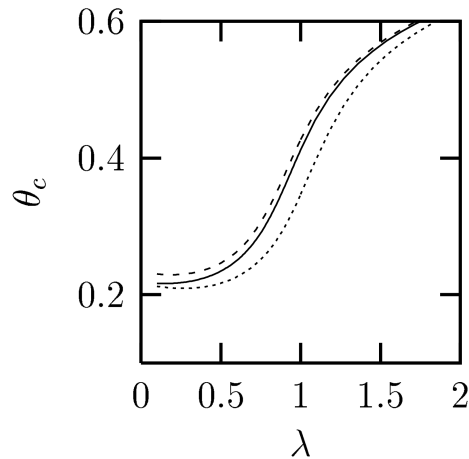


**Figure 5.11:** In the relevant parameter range the critical tilt angle increases with  $\lambda$ .

### 5.3.2 Comparison

The simulation results of Sec. 5.2 are quite obviously very similar to the picture developed using the analytic theory. The most outstanding similarities are the presence of the director tilt and the onset of an undulation instability above a threshold value for the shear rate. In this section we will present a more detailed comparison between the results of Secs. 5.2 and 5.3.1. With the performed simulations we are able to determine almost all the dimensionless parameters of the system without making use of the onset of the undulation instability. This in turn enables a check of the set of parameters by comparing the observed (simulated) undulation threshold to the threshold predicted by the analytic theory (using the material parameters).

We start our discussion with the stationary and dynamic behavior of the director tilt below the onset of undulations. In the analytical part we showed that the time depen-

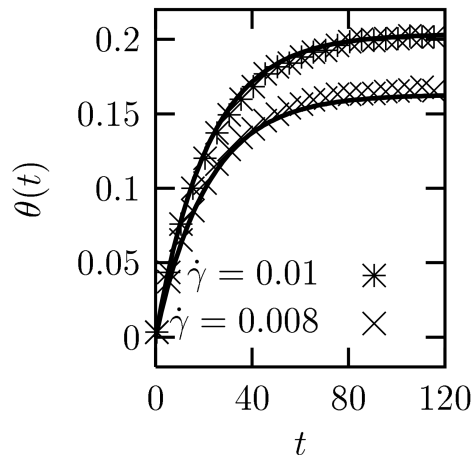


**Figure 5.12:** Time evolution of the director tilt after a step like start of the shear for two different final shear rates (0.010 and 0.012 in Lennard-Jones units). The lines show the fit to the data using Eq. (5.15). For some points also error bars are shown to give an impression of the statistical error.

dence of the director tilt after a step-like start of the shear will approach its stationary value within a characteristic time given by  $\tau_1 = \gamma_1/B_1$  [see Eq. (5.15)]. Fig. 5.12 gives a comparison of the time evolution of the director tilt after a step-like start of the shear for different shear rates<sup>13</sup>. Since Eq. (5.15) is only valid for small  $\theta$  we must restrict our analysis of the numerical data to small shear rates. Both shear rates used lead to the same values for  $B_1/\gamma_1$  and  $\lambda$ , namely,

$$\frac{B_1}{\gamma_1} = 0.045 \pm 0.004, \quad (5.19)$$

$$\lambda = 0.88 \pm 0.1. \quad (5.20)$$

In principle most of the parameters could be derived from a fit of Eq. (3.49) to the data plotted in Fig. 5.4, where we show the stationary response of the director tilt as a function of shear rate. But it turns out that such a fit is rather imprecise. Instead, we use the previously derived flow alignment parameter to reduce the uncertainty in the fit. The value for  $B_1/\gamma_1$  in this fit is consistent with the results to Fig. 5.12. Following this procedure we can derive the last undetermined parameter of Eq. (3.49)

$$\frac{B_0}{\gamma_1} = 0.22 \pm 0.14 \quad (5.21)$$

With the results for  $B_0/\gamma_1$  and  $B_1/\gamma_1$  at hand we can provide now an estimate for the ratio  $B_0/B_1$ .

$$\frac{B_0}{B_1} = 5.3 \pm 3.4 \quad (5.22)$$

Let us turn for a moment to the simulations of the dilated system where no shear is present. Those show an onset of the undulation instability at a dilation of about 2%.

<sup>13</sup>Note, that the time needed to establish the linear shear profile apparently is negligible in comparison to the characteristic time for the director tilt

Assuming a square root dependence of the amplitude beyond onset we get (see dashed line in Fig. 5.7)

$$\varepsilon_c = 1.6 \pm 0.2\% \quad (5.23)$$

Inserting this value along with the estimate from above for  $B_0/\gamma_1$  in Eq. (5.18) we obtain

$$\frac{K}{B_1} \left( \frac{2\pi}{L} \right)^2 = 0.085 \pm 0.055. \quad (5.24)$$

Besides the renormalized viscosities  $\nu_i/\gamma_1$  all relevant parameters are now determined. The analytical theory predicts only a slight influence of the viscosities on the onset as long as  $\nu_i/\gamma_1 \gtrsim 0.05$ . If we assume this relation to hold, the predicted threshold value for the undulation instability is

$$\theta_c \gtrsim 0.18. \quad (5.25)$$

For a good estimate of the critical shear rate we assume a square root dependence of the undulations amplitude and, thus, find a simulated critical shear rate of

$$\dot{\gamma}_{c,\text{sim}} = 0.0103 \pm 0.0007. \quad (5.26)$$

Transforming this simulated threshold value with Eq. (3.49) and the above parameters, we find the simulated critical tilt angle to be

$$\theta_{c,\text{sim}} = 0.18 \pm 0.02 \quad (5.27)$$

Thus, we can conclude that, within the error bars, the analytic theory is in qualitative as well as reasonable quantitative agreement with the simulation results in the range of validity of the linear theory.

### 5.3.3 Concluding remarks

The simulation of this model system for layered liquids shows, above a critical shear rate, an undulation instability, which arises spontaneously. The analytic theory tests for the stability of the spatially homogenous state against undulations and also finds a critical shear rate. Despite the differences in the approaches, both methods (molecular dynamics simulations and analytic theory) are in good qualitative and reasonable quantitative agreement in the range of validity of both methods. At low shear rates we observe a director tilt in the simulations which corresponds to analytical predictions. Increasing the shear rate above a critical value leads (in the simulations and in the analytic theory) to a undulation instability of the layers. Using a number of further simulations on the same system, we can determine an (almost complete) set of material parameters for the simulated system independent of the threshold value of the tilt angle. Inserting these parameters in the analytical calculations we can show that both methods are in good agreement within the error bars. For many purposes, we conclude that the accessible size of the simulated systems is now in the range covered by continuum approaches (as, *e.g.*, hydrodynamic theory) and the comparison between both kinds of approaches may have stimulating effects for both fields.





---

# Chapter 6

## Weakly non-linear analysis

The linear stability analysis discussed in the previous chapters determines only the onset of the instability in the deterministic system described by the governing equations. Without further investigations nothing can be said about the state into which the system will evolve at higher shear rates than the critical one. To analyze the situation near the critical point of the instability a weakly non-linear analysis has to be performed.

### 6.1 General procedure

In this section we present a brief review of the method for more details of the underlying procedure see, *e.g.*, Refs. [10, 21, 22, 34, 89, 115]. The basic aim of a weakly nonlinear analysis is to explore the parameter space near the onset of an instability. As shown in the Technical Note 2.1 a linear stability analysis ignores all nonlinear parts of the governing equations. In a linear stability analysis first the spatially homogeneous state  $\vec{X}_0$  is determined and then the governing equations are linearized in small deviation  $\vec{X}_1$  from this state. This allows to deduce the range of stability of the spatially homogeneous state. At the onset of the instability exactly one mode, characterized by a wave vector  $\vec{q}_c$  has a vanishing growth rate  $\tau^{-1} = 0$ . For all other modes the growth rate is negative.<sup>1</sup> If the control parameter, the tilt angle  $\theta_0$ , is slightly above its critical value, a band of wave vectors around the critical one is unstable. The effect of these additional wave vectors can be summarized in an additional envelope function  $A$ . The system studied has a preferred direction parallel to the vorticity direction [see, *e.g.*, Sec. 2.3 and our ansatz in Eq. (3.46)]. Since the critical wave vector is parallel to this direction, we must also consider for one-dimensional spatial variations a band of wave vectors parallel to the critical one.

---

<sup>1</sup>In our case the critical wave vector points along the vorticity direction. But in systems with no preferred in-plane direction all wave vectors with the same magnitude are equivalent. Consequently, the unstable mode at onset is only characterized by its magnitude  $q$ . The analysis of interactions between different wave vectors having the same magnitude needs also a weakly nonlinear analysis.

Typically  $A$  follows an equation of the type<sup>2</sup>

$$\tau_0 \frac{\partial}{\partial t} A = \eta^2 A + \xi_0^2 \frac{\partial^2 A}{\partial x^2} - g|A|^2 A, \quad (6.1)$$

where  $\eta$  is a small parameter measuring the distance to the critical point

$$\theta_0 = \theta_c(1 + \eta^2) \quad (6.2)$$

and  $\tau_0$  and  $\xi_0$  are the characteristic time and length scales. *A priori* it is not clear that there is no term proportional to  $\eta$  in the expansion of  $\theta_0$  in Eq. (6.2). Later we will show that such a term must vanish in our system. The characteristic scales follow directly from the properties of the neutral curve  $\theta(q)$  and the growth rate  $\tau^{-1}$  [17, 22]:

$$\tau_0^{-1} = \theta_c \left. \frac{\partial \tau^{-1}}{\partial \theta} \right|_{\theta=\theta_c} \quad (6.3)$$

$$\xi_0^2 = \frac{1}{2\theta_c} \left. \frac{\partial^2 \theta(q)}{\partial q^2} \right|_{q=q_c} \quad (6.4)$$

Since the major aim of this chapter is to deduce the nature of the bifurcation (see Technical Note 6.1), we do not present the dependences of  $\tau_0^{-1}$  and  $\xi_0^2$  on the material parameters. To determine the non-linear coefficient  $g$  we follow the standard procedure (see, *e.g.*, Refs. [17, 22]) and expand the unknown quantities in the small parameter  $\eta$

$$\vec{X} = \vec{X}_0 + \eta A \vec{X}_1 + (\eta A)^2 \vec{X}_2 + \dots, \quad (6.5)$$

with the spatially homogeneous solution  $\vec{X}_0$ , the linear solution  $\vec{X}_1$ , and higher order corrections  $\vec{X}_2$ , *etc.*

At this point it is convenient to split the differential operator  $D$  (which represents the governing equations) into several parts

$$D = L_0 + \delta L_2 + N_2 + N_3 + \text{h.o.t.} \quad (6.6)$$

Here  $L_0$  is the linear operator as used in the linear stability analysis but with  $\theta_0 = \theta_c$  and  $\delta L_2$  contains only the parts of  $L_0$  proportional to  $\theta_0$  with the replacement  $\theta_0 \rightarrow \theta_c \eta^2$ .

Inserting these ansätze into the governing equations leads to a hierarchy of equations which has to be solved successively.

$$\eta^1 : \partial_t \vec{X}_1 = L_0 \vec{X}_1 \quad (6.7a)$$

$$\eta^2 : \partial_t \vec{X}_2 = L_0 \vec{X}_2 + N_2(\vec{X}_1 | \vec{X}_1) \quad (6.7b)$$

$$\eta^3 : \partial_t \vec{X}_3 = L_0 \vec{X}_3 + \delta L_2 \vec{X}_1 + N_2(\vec{X}_1 | \vec{X}_2) + N_2(\vec{X}_2 | \vec{X}_1) + N_3(\vec{X}_1 | \vec{X}_1 | \vec{X}_1) \quad (6.7c)$$

...

---

<sup>2</sup>This equation is often called envelope equation. A more general formulation would also include a second order term in  $A$ . We will show later that this term vanishes in our case.

**Technical Note 6.1** Properties of the amplitude equation

In Eq. (6.2) we have assumed implicitly that we only consider situations with control parameters  $\theta_0$  larger than the critical one. In this Technical Note we consider a more general situation with

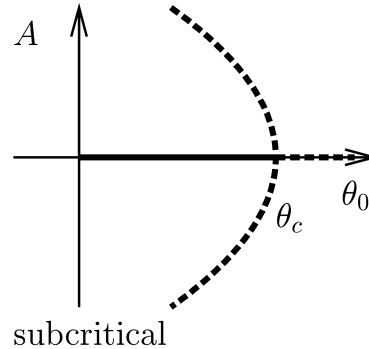
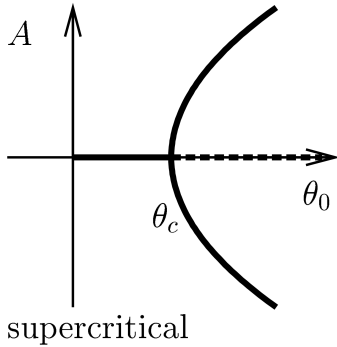
$$\theta_0 = \theta_c(1 \pm \eta^2).$$

The corresponding amplitude equation

$$\tau_0 \frac{\partial}{\partial t} A = \pm \eta^2 A + \xi_0^2 \frac{\partial^2 A}{\partial x^2} - g|A|^2 A,$$

has spatially homogeneous solutions in the following cases [22]:

- Supercritical bifurcation:  $\theta_0 = \theta_c(1 + \eta^2)$  and  $g > 0$
- Subcritical bifurcation:  $\theta_0 = \theta_c(1 - \eta^2)$  and  $g < 0$



In a supercritical bifurcation (left)  $|A| = 0$  is stable for control parameters smaller than the critical one. Above  $\theta_c$  the amplitude increases with a square root dependence and  $|A| = 0$  is unstable. In a subcritical bifurcation (right) there is an unstable branch with non-zero  $A$  for  $\theta_0 < \theta_c$  and a stable one for  $|A| = 0$ . At the critical point,  $|A| = 0$  becomes unstable and the amplitude typically jumps to a finite value which has to be determined using higher order terms (*e.g.*, quintic) in the amplitude equation.

If one knows the sign of  $g$ , the nature of the bifurcation (sub- or supercritical) is clear.

The first equation in this hierarchy of equations is the linear equation already analyzed. We now use the linear results to construct the higher order solutions. In each step of the iteration, we first check the solvability of the equation, using the Fredholm theorem,<sup>3</sup> and then compute the next correction to the linear solution.

The Fredholm theorem requires that the solution of the adjoint linear problem  $\vec{X}^+$  is perpendicular to the inhomogeneity (in our case the sum of all terms on the right hand side of our hierarchy of equations, except the  $L_0$  term). Using a suitable scalar product we can compute the adjoint differential operator *via* integration by parts.

$$\langle \vec{X}^+ | L_0 \vec{X}_1 \rangle = \langle L_0^+ \vec{X}^+ | \vec{X}_1 \rangle \quad (6.8)$$

This integration by parts leads to a number of surface terms. To determine the boundary conditions of the adjoint problem, we insert the boundary conditions of the direct problem into these surface terms. Forcing the remainder to vanish leads to the boundary conditions for the adjoint problem [78]. In the present case we used the scalar product

$$\langle \vec{Y} | \vec{Z} \rangle = \int_{-d/2}^{d/2} dz \int_{-\pi/q}^{\pi/q} dy \vec{Y} \cdot \vec{Z}.$$

We found that the adjoint linear problem can be constructed from the transposed linear problem by multiplying each of the spatial derivatives by  $-1$  ( $\nabla_i \rightarrow -\nabla_i$ ). The boundary conditions and the symmetry properties of the adjoint linear solutions are the same as for the linear problem.

## 6.2 Iterative solution

Due to the complexity of the governing equations, the actual calculations are performed with a Maple program, which we describe in Appendix C. For the evaluations of the solvability condition (which arises due to the Fredholm theorem) we first have to construct the solution to the adjoint problem. This can be done in the same way as shown in Sec. 3.4, since it turns out that both, the symmetry properties and the boundary conditions are the same for the linear problem and its adjoint problem.

The first two orders in  $\eta$  [ $O(\eta^0)$  and  $O(\eta^1)$ ] of the hierarchy of equations lead to the spatially homogeneous state and the linear problem, which we analyzed in the previous chapters. In order  $\eta^2$  the solvability condition reads

$$\langle \vec{X}^+ | \mathbf{N}_2(\vec{X}_1 | \vec{X}_1) \rangle = 0. \quad (6.9)$$

We find that the nonlinear term in the inhomogeneity is perpendicular to the solution of the linear adjoint problem. The non-linear term  $\mathbf{N}_2(\vec{X}_1 | \vec{X}_1)$  contains only lateral

---

<sup>3</sup>An early version of this theorem was published by Fredholm in Ref.[39].

**Technical Note 6.2** Absence of  $\theta^{(1)}$

In this Technical Note we investigate the consequences of a linear term in the expansion of  $\theta_0$ .

$$\theta_0 = \theta_c + \theta^{(1)}\eta + \dots$$

The additional  $\theta^{(1)}$  term leads directly to the new term  $\delta L_1$  in the expansion of  $D$

$$D = L_0 + \delta L_1 + \delta L_2 + N_2 + N_3 + \text{h.o.t.},$$

where  $\delta L_1$  is proportional to  $\theta^{(1)}$ . The term  $\delta L_1$  contributes to the equation in order  $\eta^2$  and the corresponding solvability condition reads

$$\left\langle \vec{X}^+ \left| \delta L_1 \vec{X}_1 + N_2(\vec{X}_1 | \vec{X}_1) \right. \right\rangle = 0.$$

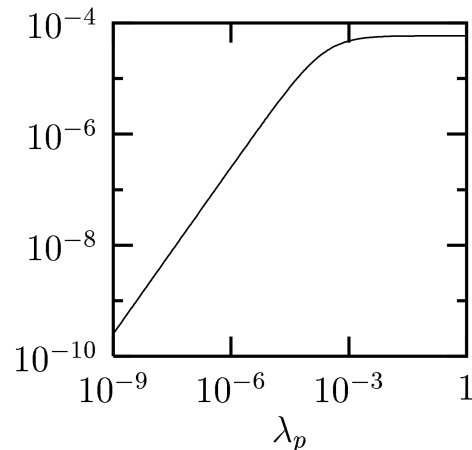
As discussed in Sec. 6.2,  $\left\langle \vec{X}^+ \left| N_2(\vec{X}_1 | \vec{X}_1) \right. \right\rangle$  vanishes. In general,  $\left\langle \vec{X}^+ \left| \delta L_1 \vec{X}_1 \right. \right\rangle$  takes some non-zero value which is proportional to  $\theta^{(1)}$ , because  $\vec{X}^+$  and  $\vec{X}_1$  have the same spatial dependences. So the only way to fulfill the solvability condition of the equation in order  $\eta^2$  is to choose  $\theta^{(1)} = 0$ , *i.e.*, to suppress the linear term in the expansion of  $\theta_0$ .

spatial dependences including  $q = 0$  and  $q = 2q_c$ , whereas  $\vec{X}^+$  has only plane waves with  $q = q_c$ ; for this reason the integral (6.9) vanishes for symmetry reasons. This orthogonality has important consequences: i) There is no quadratic term in  $A$  in the amplitude equation. ii) No linear term in the expansion of  $\theta_0$  is possible (see Technical Note 6.2 for details). With these results, the inhomogeneous solution in second order can directly be calculated making use of the structure of the nonlinear term  $N_2(\vec{X}_1 | \vec{X}_1)$ . The ansatz for  $\vec{X}_2$  follows directly from the spatial dependences of  $N_2(\vec{X}_1 | \vec{X}_1)$  (see also Appendix C). For example the lateral ansatz is

$$X_{2,i} \sim \left\{ \begin{array}{l} D_i \sin(qy) \cos(qy) \\ E_i^1 \sin^2(qy) + E_i^2 \cos^2(qy) \end{array} \right\}, \quad (6.10)$$

where the unknown constants  $D_i$ ,  $E_i^1$ , and  $E_i^2$  are determined through the solution of Eq. (6.7b). A similar ansatz is chosen for the dependence of  $X_{2,i}$  on  $z$ . Note that the  $z$  symmetry properties of  $\vec{X}_2$  are opposite to the ones summarized in Tab. 3.3 for  $\vec{X}_1$ . *A priori* this solution does not satisfy the boundary conditions and one must add a homogeneous solution of  $L_0$  with the same symmetry properties as the inhomogeneous solution to fulfill the boundary conditions. In our case, however, the boundary conditions are fulfilled for all variables, with the exception of  $v_{y,2}$ . Similarly to the discussion of the boundary conditions at the end of Sec. 3.1, we now allow the smallest velocity component,  $v_{y,2}$ , to violate the boundary conditions, because its relative amplitude is negligible compared to the leading component of the velocity field,  $v_{x,2}$ , (see Fig. 6.1).

**Figure 6.1:** Similarly to the linear case, the  $y$  component of the velocity field is strongly suppressed by the permeation constant. Here we show the amplitude of  $v_{y,2}$  divided by the amplitude of  $v_{x,2}$ . Clearly,  $v_{y,2}$  is negligible in the relevant range of  $\lambda_p$ , consequently, we can also neglect the boundary condition for this component of the velocity field.



The solvability condition in order  $\eta^3$

$$\left\langle \vec{X}^+ \left| \delta \mathbf{L}_2 \vec{X}_1 + \mathbf{N}_2(\vec{X}_2 | \vec{X}_1) + \mathbf{N}_2(\vec{X}_1 | \vec{X}_2) + \mathbf{N}_3(\vec{X}_1 | \vec{X}_1 | \vec{X}_1) \right. \right\rangle = 0 \quad (6.11)$$

leads to a nontrivial equation for the amplitude function  $A$  of the instability. We find a relation of the form

$$r_a \eta^2 A + g^* |A|^2 A = 0, \quad (6.12)$$

with the definitions

$$g^* = \left\langle \vec{X}^+ \left| \mathbf{N}_2(\vec{X}_1 | \vec{X}_2) + \mathbf{N}_2(\vec{X}_2 | \vec{X}_1) + \mathbf{N}_3(\vec{X}_1 | \vec{X}_1 | \vec{X}_1) \right. \right\rangle, \quad (6.13)$$

$$r_a = \left\langle \vec{X}^+ \left| \delta \mathbf{L}_2 \vec{X}_1 \right. \right\rangle. \quad (6.14)$$

Obviously, the constants  $r_a$  and  $g^*$  depend on the normalization of the adjoint solution  $\vec{X}^+$ . This short coming can be eliminated if we divide Eq. (6.12) by  $r_a$  and define

$$g = -\frac{g^*}{r_a}. \quad (6.15)$$

Note that this definition is consistent with the definitions of  $\tau_0$  and  $\xi_0^2$  given in the previous section [17, 22, 34]. We now have determined all constants entering the amplitude equation (6.1). In the following discussion we concentrated on the nature of the bifurcation, *i.e.*, the value of  $g$ .

In Figs. 6.2 and 6.3 we explore the parameter space around the typical values estimated in the Technical Note 3.2.

As a rule of thumb, we can conclude that the bifurcation is forward (supercritical) for all typical values. In some areas the bifurcation becomes backwards (subcritical), but this coincides in all investigated cases with unrealistically high critical tilt angles. A comparison to the results in Chapter 3 shows that a backward bifurcation is only possible in cases with  $\theta_c \gtrsim 0.5$  rad.

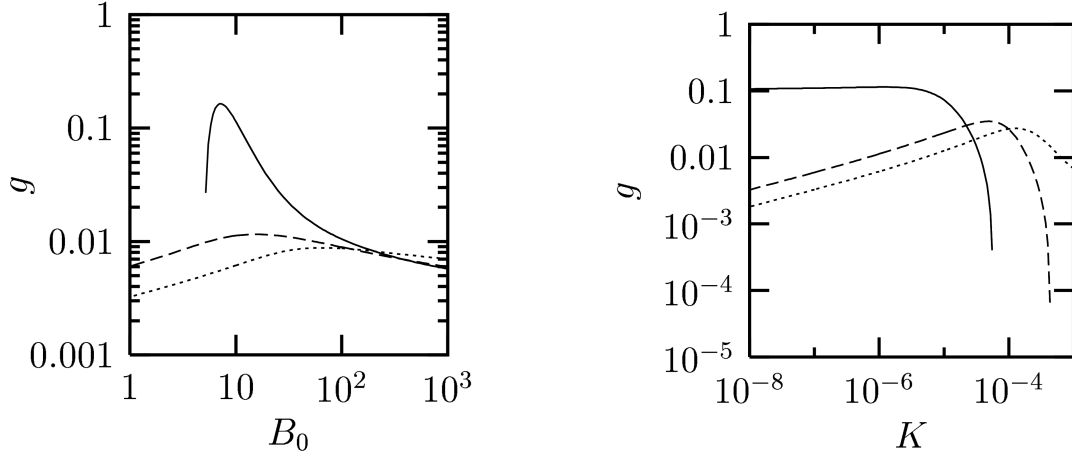


**Figure 6.2:** For typical values of the material parameters, the bifurcation is forward (supercritical). Here we present the dependence of  $g$  on the compression modulus of the layers  $B_0$  and the bending modulus  $K$  for various values of  $\lambda$ :  $\lambda = 1.1$  for solid lines ( — ),  $\lambda = 0.7$  for dashed lines ( - - - ) and  $\lambda = 0.1$  for dotted lines ( ..... ). The curves end at points where  $g$  changes sign. Note that in these cases the critical tilt angle is always very high (typically  $\theta_c \gtrsim 0.5$  rad).

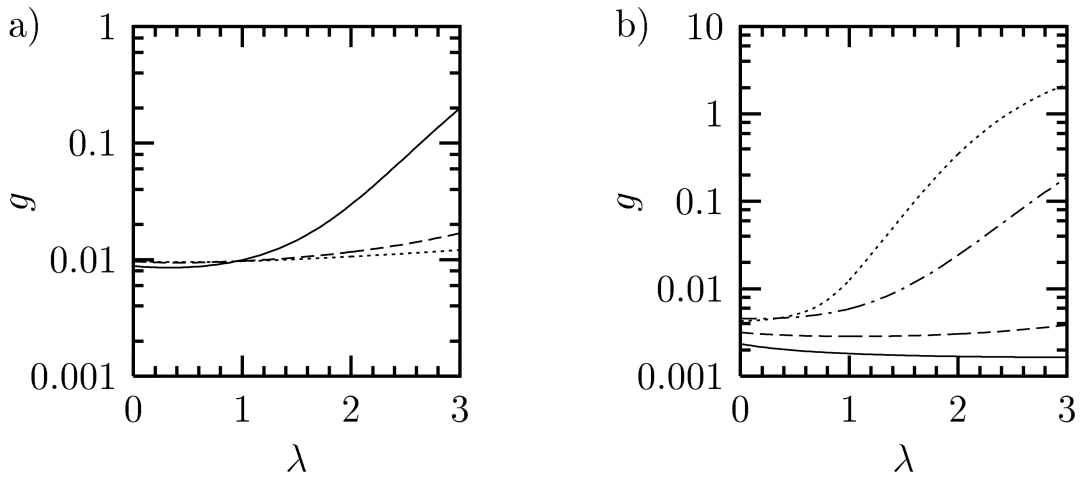


**Figure 6.3:** As a function of  $\lambda$  we observe a forward bifurcation in all investigated cases. In part a) the dependence of  $g$  for several values of the (isotropic) viscosity is shown. The solid line ( — ) corresponds to  $\nu_i = 0.1$ , the dashed line ( - - - ) to  $\nu_i = 1$  and the dotted line ( ..... ) to  $\nu_i = 10$ . Part b) shows the variations with the compression modulus of the layers:  $B_0 = 10^4$  for the solid line ( — ),  $B_0 = 10^3$  for the dashed line ( - - - ),  $B_0 = 100$  for the dot-dashed line ( - . - ) and  $B_0 = 30$  for the dotted line ( ..... ).

At this point a qualitative comparison to the molecular dynamics simulations mentioned in the previous chapter is instructive. These simulations show a square root dependence of the undulation amplitude as a function of the shear rate. Although the boundary conditions in the simulated system are slightly different, this simulated results are compatible with the weakly non-linear analysis given above.

The picture which can be drawn from the above results is the following. Under an applied shear a layered liquid in its parallel orientation shows flat layers if the shear rate is below the critical shear rate. Above the critical shear rate finite amplitude undulations (of the layers as well as of the strength of the order parameter) develop, where the amplitude is determined by Eq. (6.12).



---

# Chapter 7

## Summary and conclusions

In this thesis, we have shown that the inclusion of a nematic degree of freedom in the macroscopic hydrodynamic description of smectic-*A*-like liquids leads to a number of interesting results. While the director and the layer normal are coupled such that they are parallel in equilibrium, in non-equilibrium situations, the director needs not be parallel to the smectic layer normal. This is in contrast to standard smectic-*A* hydrodynamics. Using irreversible thermodynamics and symmetry arguments, we derived a complete set of macroscopic hydrodynamic equations for the director variables, the layer displacement, the velocity field, and the moduli of the nematic and smectic order parameters.

As external fields, we investigated simple shear with the smectic layers parallel to the planes of constant velocity, (“parallel” orientation) and a magnetic field at an arbitrary orientation to the layers. In spatially homogeneous situations, shear and magnetic fields lead to similar results. The external field exerts a torque on the director that must be balanced by the coupling to the layer normal. In the limit of small angles, balancing these torques leads, in the steady state, to a shear-induced director tilt proportional to the shear rate, or, to a magnetic field-induced director tilt proportional to the square of the magnitude of the field.

Recent experiments find that the parallel orientation of smectic-*A*-like liquids (low molecular weight thermotropic liquid crystals, lyotropic lamellar phases, liquid crystalline polymers, block copolymers) is destabilized by an applied shear. After destabilization, two typical scenarios are observed in a steady state situation: i) The layers are oriented perpendicular to the vorticity direction of the flow, *i.e.*, they lie in the plane spanned by the velocity and the gradient direction (“perpendicular” orientation). ii) Closed multi-lamellar vesicles (“onions”) form. A number of experiments indicate that the onset of this reorientation is controlled by the applied shear rate.

In contrast to standard smectic-*A* hydrodynamics where shear in the parallel orientation has no effect on the layers, this destabilizing effect comes out naturally from our extended smectic-*A* hydrodynamics. The argumentation goes along the following lines. The preferred thickness of a smectic layer is directly connected to the projection of the averaged molecular axes on the layer normal, or, in terms of our model, the thickness

is proportional to the projection of the director on the layer normal. If the director is tilted, this projection is shorter. This decrease of the projection is equivalent to an effective dilation, because the actual layer thickness is larger than the preferred layer thickness. Similar to the case of low molecular weight smectic-*A* liquid crystals under a dilative strain, this effective dilation leads to an undulation instability.

To investigate the stability of the parallel alignment, we performed a linear and weakly non-linear analysis of the governing equations. The initial state is the above described spatially homogeneous director tilt with the smectic layers in the parallel orientation. Using a linear stability analysis we first determined the region in the parameter space, where the spatially homogeneous state is linearly stable. In addition we deduced the nature of the bifurcation using a weakly non-linear analysis. The linear stability analysis showed an undulation instability which sets in above a critical tilt angle (or equivalently, a critical shear rate). This critical tilt angle turned out to depend strongly on the material parameters. For a typical low molecular weight thermotropic liquid crystal, we estimated the critical tilt angle to be on the order of a few degrees. The linear stability analysis also revealed that the nematic and smectic order is modulated close to the boundaries. Since the probability for the formation of defects is larger in regions with a decreased modulus of the order parameter, these variations in the modulus of the order parameter open the way for a destabilization of the layered structure. We note that a detailed investigation of this point is beyond the scope of the present work. Finally, we could exclude an oscillatory instability for all physically reasonable regions in parameter space.

A comparison of our results to experiments on layered liquids showed good qualitative agreement. Recent experiments on lyotropic lamellar phases revealed that the destabilization of the parallel alignment develops *via* an intermediate state of undulating lamellae or parallel multi-lamellar cylinders. For one of these lyotropic systems, enough material parameters have been measured to allow semi-quantitative comparisons. The diameter of the observed objects is comparable to the critical wavelength predicted by the analytic theory.

A more detailed comparison to an independent approach was undertaken in a collaboration with simulation physicists from the Max-Planck-Institute for Polymer Research in Mainz. In a molecular dynamics simulation, a model layered liquid consisting of chains of four particles ( $A_2B_2$ ) was considered. The four particles are connected with springs. The interaction potential of particles not connected by springs is attractive for like particles and repulsive for particles of a different nature. The simulation demonstrated the two main predictions of our analytic theory: The director tilts in the flow direction and, above a critical shear rate, the layers show stationary undulations with a wave vector in the vorticity direction. Besides this good qualitative agreement, a reasonable quantitative agreement for the critical shear rate was found.

Using a weakly non-linear analysis, we investigated the properties of the undulation instability near onset. We have shown that the bifurcation is supercritical for most physically relevant regions in the parameter space.

---

We have developed in this thesis an extended smectic-*A* hydrodynamics in which the director is no longer rigidly coupled to the layer normal but can deviate from it in non-equilibrium situations. This extended smectic-*A* hydrodynamics allows a straightforward interpretation of shear experiments on lamellar phases. The predictions of our model are in good qualitative and reasonable quantitative agreement with experiments and molecular dynamics simulations.



---

# Appendix A

## Frozen-in magnetic order in uniaxial gels<sup>1</sup>

During the work on the reorientation phenomena in layered liquids, the author had the possibility to work experimentally on the preparation and characterization of magnetic gels. Although this is a work on a different topic than the rest of thesis we present here the results for completeness.

### A.1 Introduction

The study of intelligent gels and elastomers is a rapidly growing field of soft condensed matter physics. Examples include polyelectrolyte gels with interesting mechano-chemical properties [97, 98, 99] and liquid crystalline elastomers [35, 92], which are discussed for applications as actuators and components of artificial muscles. In chemical gels a network of covalent bonds gives rise to a nonzero static shear modulus.

The field of isotropic magnetic gels, reacting to applied field gradients, has been pioneered by Zrinyi's group [144] (compare also Ref. [143] for an early review) and since a number of investigations of magnetic gels has been published (compare, *e.g.*, Refs. [5, 6]).

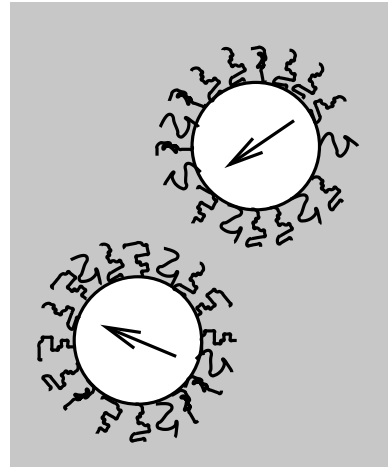
Here we describe the preparation of a ferrofluid-based uniaxial magnetic gel with frozen-in magnetic order (see Fig. A.1 for a schematic picture of a ferrofluid). Most of the previous work [144, 143] concentrated on isotropic magnetic gels. Up to now no work on the mechanical characteristics of oriented magnetic gels appears to exist.

Due to the frozen-in magnetic order, the magnetic gels described here show a substantial response to a homogeneous magnetic field. In addition, we present time and frequency dependent measurements of the shear modulus  $G'$ . We show that the time-dependence can be fitted to a stretched exponential.

---

<sup>1</sup>This work has been done in the framework of a PROCOPE collaboration with the group of P. Martinoty at the Université Louis Pasteur (Strasbourg, France). The author was involved in the experiments during an extended stay in Strasbourg in spring 2002. This appendix is based on Ref. [20].

**Figure A.1:** A ferrofluid (or magnetic fluid) is a colloidal suspension of small magnetic mono-domain particles in a carrier fluid. The particle diameter is typically  $\sim 10$  nm. In these small magnetic particles the wall energy is too high to develop more than one magnetic domain. To avoid an agglomeration of the magnetic particles, they are coated. The coating compatibilizes the magnetic particles with the surrounding fluid and guarantees a minimal distance between two particles. At this minimal distance the magnetic interaction energy is of the order of the thermal energy. For this reason these particles do not aggregate. Similarly any sedimentation is hindered by thermal agitation. The carrier fluid may be either an organic or a polar solvent (see, *e.g.*, Ref. [112] for more details).



This appendix is organized as follows. In Sect. A.2 we describe the preparation and the experimental set-ups. In Sect. A.3 we present the results of our magnetic, optical and mechanical measurements, which we discuss in Sects. A.4 and A.5.

## A.2 Experimental part

### A.2.1 Preparation of the samples

The magnetic fluid (M-300 from Sigma-Hi-Chemical, Japan) is introduced into a 7.5 wt.-% aqueous solution of poly(vinyl-alcohol) (PVA) (degree of hydrolyzation of 98 – 99 %, average molecular weight 31,000 – 50,000 g/mol, from Aldrich Chemical Company). The crosslinking reaction is made with glutardialdehyd (50 wt.-% aqueous solution from Aldrich, referred to as GA) at a  $\text{pH} \approx 1.5$  (through addition of HCl 37 % from Riedel-de Haën). We used all compounds without further purification.

It turns out that the best way to prepare a gel with about 14 vol.-% magnetic fluid (or a volume fraction of the solid particles of  $\Phi \approx 0.5$  vol.-% in the final gel) is a two step process with the following typical recipe. In tube A 600  $\mu\text{l}$  of the PVA solution are mixed with 48  $\mu\text{l}$  HCl and in tube B we start with 300  $\mu\text{l}$  magnetic fluid and add successively 1.5 ml PVA solution and 14  $\mu\text{l}$  GA. After the contents in both tubes is well mixed we add half of the contents of tube A to tube B. This procedure is chosen such that the crosslinking reaction starts when A and B are mixed. For the mechanical measurements 8  $\mu\text{l}$  of the pre-gel are placed in a piezo-rheometer and surrounded by a Newtonian low viscosity silicone oil (E7 from Haake), to conserve the water content in the sample. We note that the properties of the resulting magnetic gel are especially sensitive to the concentrations of HCl and GA.

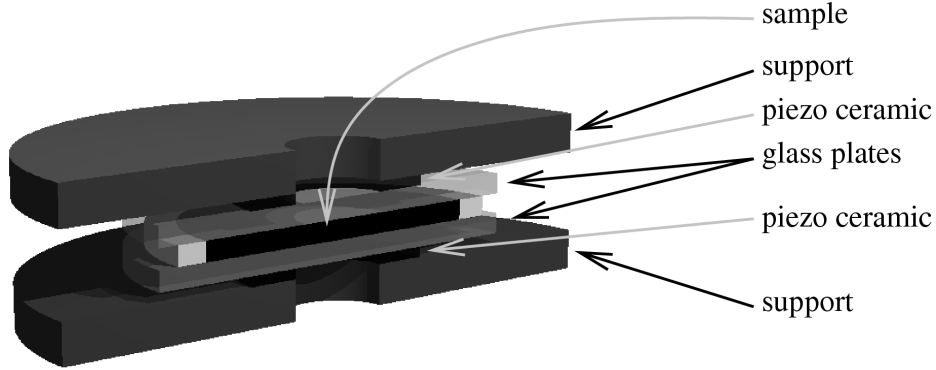


**Figure A.2:** A schematic picture of the piezo-rheometer cell used in the experiments. The cell is similar to the one described in Refs. [131, 137].

## A.2.2 Measurements

For the mechanical measurements we use a piezo-rheometer similar to the one described in Refs. [131, 137] (see Fig. A.2 for a schematic picture). The principle of the set-up consists in applying a very small shear strain  $\epsilon$  ( $\lesssim 10^{-4}$ ) to the sample by means of a piezo-ceramic and measuring the amplitude and phase of the transmitted shear stress  $\sigma$  using a second piezo-ceramic. The small shear deformation applied is ideal for the measurement of fragile objects like forming gels. The complex shear rigidity modulus  $G^*$  is given by the stress/strain ratio  $G^* = \sigma/\epsilon$ . The sample is placed between two glass slides each of which is stuck to one of the ceramics. The samples are typically  $\sim 35\mu\text{m}$  thick and have a surface area of  $\sim 2.5\text{ cm}^2$ . The parallelism of the glass slides is adjusted by optical interference measurements to  $\sim 5 \cdot 10^{-4}$  rad. For all samples studied the compound is introduced in the sol phase and the gel is growing *in situ*. Due to the size of our set-up it can be placed into the homogeneous magnetic field (up to  $\sim 1\text{ T}$ ) of an electro-magnet, with the direction of the field either parallel or perpendicular to the sample plane. We denote the situation with the field parallel to the velocity direction as parallel orientation and the situation with the field perpendicular to the velocity direction (but in the sample plane) as perpendicular orientation. All the experiments are performed at a temperature of  $24^\circ\text{C}$ .

This set-up allows us to follow the crosslinking process by measuring the shear modulus  $G'$  over a frequency range from 0.2 Hz to 1 kHz. Typically, we follow the crosslinking reaction for three days.

In all cases reference samples have been crosslinked in test tubes in a homogeneous magnetic field of 200 mT, which was oriented perpendicular to the cylinder axis of the tube. We thus can investigate macroscopic ( $\approx 1\text{ ml}$ ) equivalents (with cylindrical shape) of the gels measured in the rheometer. To prevent evaporation of the water the reference samples are kept in distilled water once the gel is formed.

To measure the magnetization of the gels in a homogeneous magnetic field the cylindrical sample is suspended using a non-magnetic wire of known torsional modulus. The rotation

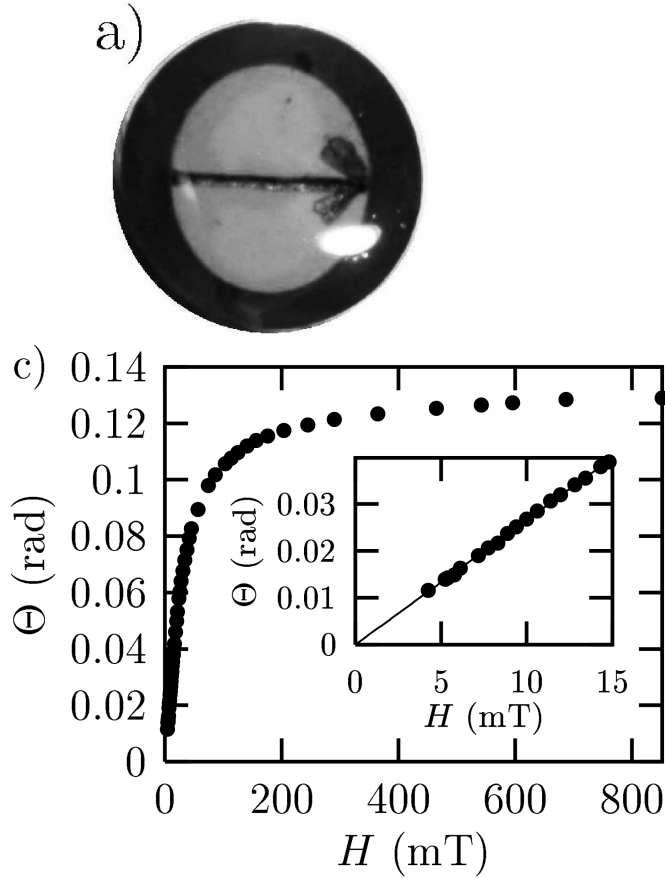


**Figure A.3:** A gel cylinder (diameter 11 mm) a) without applied field and a) after rotation in a homogeneous field of 50 mT. In c) the rotation angle as a function of the field strength is shown. For small fields, the angle is proportional to the field (see inset).

angle of the sample as a function of the field amplitude is then measured with a standard light beam deflection technique.

## A.3 Results

### A.3.1 Magnetic properties of the gel cylinders

The macroscopic samples react to an applied magnetic field in two ways. Firstly, when exposed to a magnetic field gradient the gel is attracted by the regions of higher field (as expected for any paramagnetic material). We detected the resulting force when approaching a sample to a not too small magnet (without making quantitative measurements). Secondly, in a homogeneous magnetic field the sample prefers an orientation where the frozen-in direction is parallel to the applied field (see Figs. A.3a and A.3b). In Fig. A.3a we see the position of the sample without an external homogeneous magnetic field and in Fig. A.3b in a field of 50 mT. Clearly, the sample has rotated due to the applied homogeneous magnetic field. In Fig. A.3c we have plotted the rotation angle  $\Theta$  as a function of field strength. For small magnetic fields we find a linear relation, as expected for a permanent, or more precisely, a frozen-in magnetization.



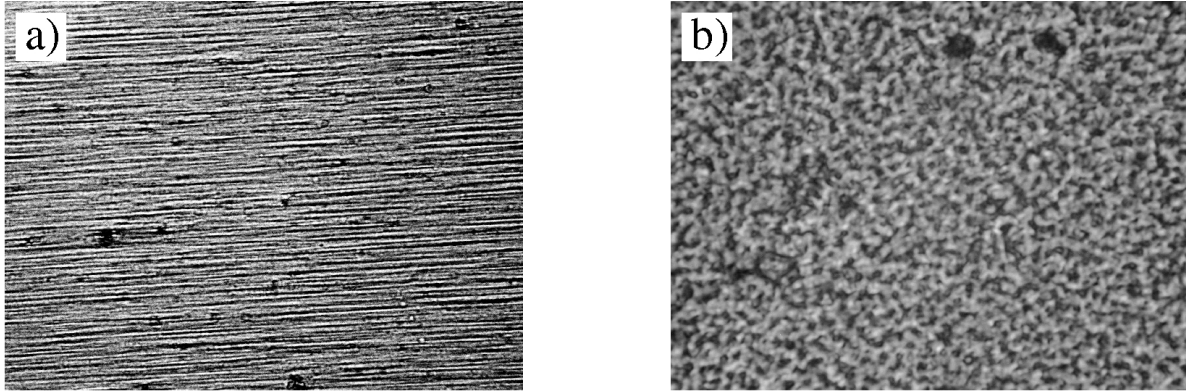


**Figure A.4:** Microscope images ( $170 \times 130 \mu\text{m}^2$ ) of two different orientations: a) The plane containing the field direction (parallel orientation) The fibers are aligned on average parallel to the field. b) Cross section perpendicular to the magnetic field (perpendicular orientation).

Thus, crosslinking the gel in a homogeneous field results in uniaxial samples with frozen-in magnetization, where the preferred axis is defined by the field orientation during the crosslinking.

### A.3.2 Optical properties of thin samples

#### Light scattering of oriented samples

As expected for a uniaxial material, oriented samples show light scattering in the directions perpendicular to the preferred axis.

#### Optical microscopy

Under an optical microscope needle-like objects with a thickness of a few microns and a length of several tens of microns are seen (Fig. A.4a). Figure A.4b shows a cut perpendicular to the axes of the needles.

#### Birefringence

When placing a thin sample, with the preferred direction in the sample plane, between crossed polarizers, total extinction can only be achieved, if the preferred orientation of the sample lies along the polarizer or analyzer direction. The sample therefore shows a small but finite birefringence demonstrating the uniaxial optical anisotropy of the material.

We note that all optical measurements have been made directly in the piezo-rheometer cell.

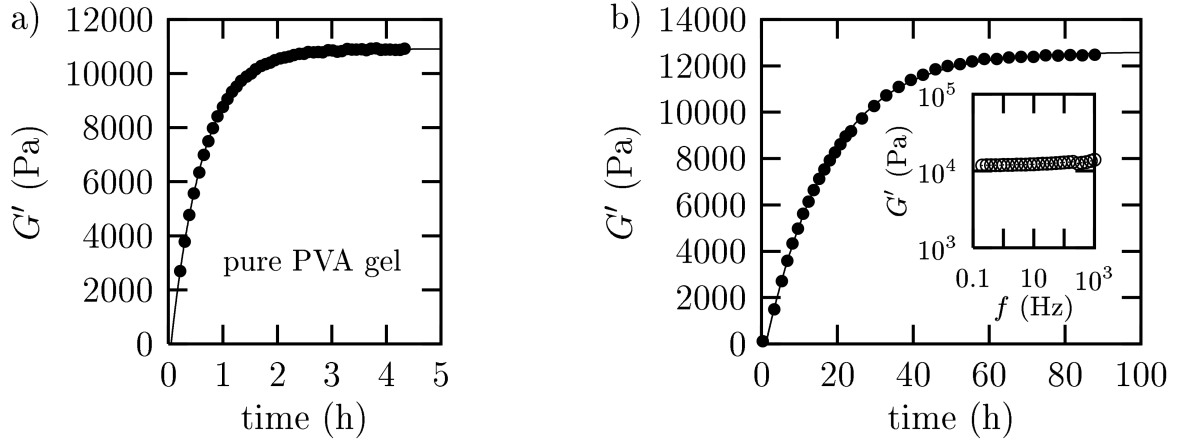


**Figure A.5:**  $G'$  measurements at a constant frequency of  $f = 1\text{Hz}$ . a) The time dependent  $G'$  for a pure PVA gel. The solid line represents the fit to a stretched exponential [see, Eq. (A.1)] with  $G'_\infty = (1.091 \pm 0.001) \cdot 10^4$  Pa,  $t_0 = 0.050 \pm 0.006$  hours,  $x = 1.00 \pm 0.01$  and  $\tau = 0.585 \pm 0.007$  hours. b) The time dependent  $G'$  for a magnetic gel in the parallel orientation in a homogeneous field of 200 mT. The solid line gives the fit to a stretched exponential with  $G'_\infty = (1.261 \pm 0.002) \cdot 10^4$  Pa,  $t_0 = 1.12 \pm 0.08$  hours,  $x = 1.01 \pm 0.01$  and  $\tau = 16.87 \pm 0.10$  hours. Inset: The shear modulus  $G'$  for  $t \sim 90$  hours as a function of frequency.

### A.3.3 Mechanical measurements

In Fig. A.5a we show  $G'$  measured at 1 Hz as a function of time for a pure PVA sample. The solid line shows that the fit to a stretched exponential gives a good representation of the data. The stretched exponential [134],

$$G' = G'_\infty \left( 1 - \exp \left\{ - \left[ (t - t_0) / \tau \right]^x \right\} \right), \quad (\text{A.1})$$

contains four parameters: i)  $G'_\infty$ , the value of  $G'$  for long times, ii)  $t_0$ , the time associated with the infinite cluster measured from the start of the rheological experiment, iii)  $\tau$ , the formation time of the network, and iv) the stretching exponent  $x$ . Figure A.5b gives the corresponding plot for a magnetic gel sample in a homogeneous magnetic field of 200 mT in the parallel geometry. Again a stretched exponential provides a good fit to the experimental data (see Sect. A.4 for a detailed discussion).

It turns out that the concentrations of HCl and GA have a strong influence on these curves. Roughly speaking, HCl controls the characteristic time (above  $\text{pH} \approx 2$  the crosslinker does not react) and GA sets the final value of  $G'$ . Even very slight (and, for all practical purposes, inevitable) differences in the actual concentration of these ingredients cause variations in the raw data (as found out from a test series done concerning the influence of the pH).

From the inset to Fig. A.5b one can see that there is no variation in  $G'$  at low frequencies over at least four orders of magnitude. This indicates that the magnetic gels investigated here possess a large hydrodynamic regime (for the time span covered by our experiments). The values of  $G'$  measured at 1 Hz in Fig. A.5a and A.5b are therefore hydrodynamic.

## A.4 Discussion

### Structure of the gel

The magnetic fluid all by itself has a  $\text{pH} \approx 8$  [96], and the crosslinker does not react above  $\text{pH} \approx 2$ . But changing the  $\text{pH}$  of the magnetic fluid (in order to start the reaction) typically results in a destabilization of the fluid, *i.e.*, the magnetic nano-particles start to form bigger clusters.<sup>2</sup> Consequently, two processes compete with each other during the crosslinking reaction: The crosslinking of the PVA chains to generate a network and the formation of clusters of magnetic particles under the influence of an applied field. Magneto-rheological fluids form chains of magnetic particles under applied magnetic fields [72]. For higher fields these chains tend to combine to fibers consisting of many chains. In fluids this chain and fiber formation is reversible, but not in our system: i) The magnetic fluid is partially destabilized by the strong acid we added. Thus some magnetic nano-particles are in contact to each other and held together by strong magnetic forces. ii) The network stabilizes the chains and fibers, because the observed size of these objects is much larger than the typical mesh size of the gel. The fibers are not compact clusters of solid particles, but rather loosely packed objects. Therefore the volume fraction of the fibers seen under the microscope appears to be much higher than what one would expect from a volume fraction of  $\Phi = 0.5$  vol. %.

For this complex gelation process we identified several ingredients: aggregation, chain and fiber formation, and the build-up of the polymer network. An open question for all magnetic gels is the precise nature of the interaction between the magnetic nano-particles and the polymer network.

### Magnetic aspects

When crosslinking the gel in a magnetic field, the easy axis of each magnetic nano-particle in the sample lies preferentially along the applied magnetic field. The polymer network freezes this configuration and gives the macroscopic material an easy axis along the applied field. Two contributions could lead to the sample rotation shown in Fig. A.3: i) A ferromagnetic-like response, and ii) the response from an anisotropic paramagnet. When balanced by the torsion of the wire one expects the rotation angle  $\Theta$  to be either linear (ferromagnetic-like) or quadratic (paramagnetic-like) in the applied field strength  $H$ . In the ferromagnetic case we find for small fields and small angles

$$\Theta = \frac{HM_0}{C} \sin(\Theta_0), \quad (\text{A.2})$$

where  $C$  is the torsional elastic constant of the wire and  $M_0$  the magnitude of the frozen-in magnetization.  $\Theta_0$  is the angle between the magnetization of the gel and the external magnetic field.

---

<sup>2</sup>Apparently the acid reduces drastically the efficiency of the coating of the magnetic nano-particles. A more detailed analysis of this effect is a non-trivial task, because the producer does not provide any detailed information about the coating.

From the slope in Fig. A.3c for small fields (shown magnified in the inset), using  $\Theta_0 \sim 0.13$  rad (the rotation angle for high fields) and  $C = 258$  in CGS units (from an independent measurement) we deduce  $M_0 \sim 1$  G. The saturation magnetization of the ferrofluid is  $M_0^f \sim 300$  G from which we deduce an upper bound for the saturation magnetization of the gel of 42 G (because the concentration of the magnetic fluid in the pre-gel was 14 vol.-%).

For the larger values of the magnetic field the paramagnetic contributions become important and lead to substantial deviations from the straight line.

### Optical aspects

The observed birefringence is rather weak. So it seems probable that the fiber formation is associated with the creation of internal tensions in the polymer network which lead to a birefringent sample. The fibers formed are at the origin of the light scattering observed.

### Time evolution of $G'$

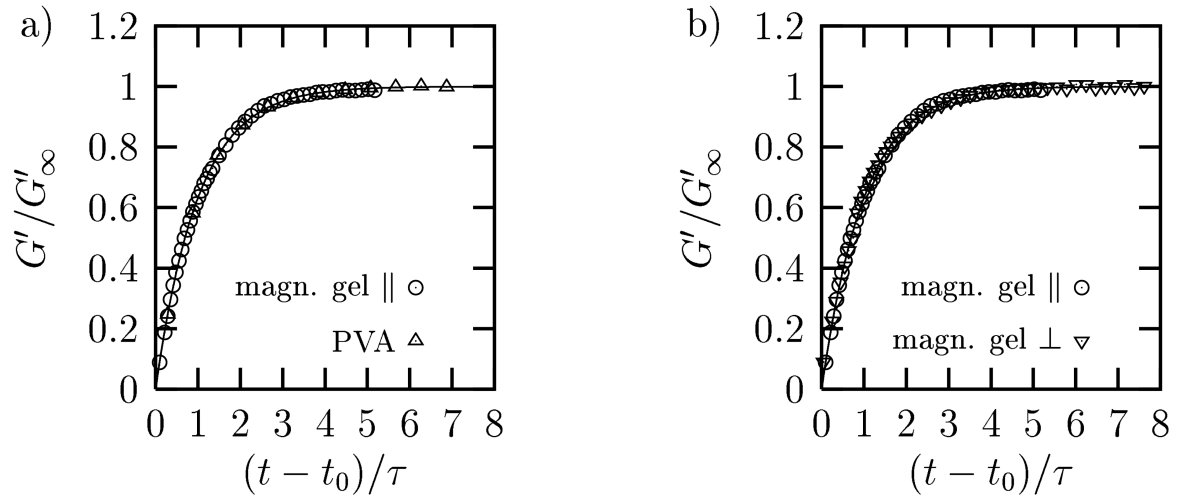
In Fig. A.6a we plot our data in terms of the rescaled variables  $G'/G'_\infty$  and  $(t - t_0)/\tau$  for the pure PVA gel and for the magnetic gel in the parallel geometry, using the parameters given in the caption to Fig. A.5. The two curves superpose perfectly thus giving rise to one master curve, although the value of the parameter  $\tau$  varies by more than an order of magnitude ( $\tau = 0.585 \pm 0.007$  for the pure PVA gel *vs.*  $\tau = 16.87 \pm 0.10$  for the magnetic gel in the parallel orientation). We emphasize that the growth behavior of the PVA gel and of the magnetic gel are both characterized by a single time scale, since the stretching exponent  $x$  is close to 1. We conclude that in both cases the same physics of gelation is at work, regardless whether the gel is charged with particles or not.

Fig. A.6b shows that the data for magnetic gels in the parallel and perpendicular orientation also fall on the same master curve as in Fig. A.6a. This implies that the magnetic gels investigated here are mechanically isotropic (or have at most a negligibly small anisotropy), in strong contrast to the magnetic and optical anisotropies. This might not be too surprising given the fact that the fibers seen in Fig. A.4 are not dense objects and therefore not very stiff.

## A.5 Conclusions and perspective

We have described the preparation of new ferrofluid-based uniaxial magnetic gels and we have characterized their physical properties. These gels are stable and basically unchanged in their physical properties over a year at least. The response of these gels to a uniform magnetic field demonstrates the frozen-in magnetization in the samples.

Mechanically our gels show no anisotropy and a broad hydrodynamic regime, in contrast to liquid crystalline elastomers [41], which have a narrow hydrodynamic regime and a substantial mechanical anisotropy (see, *e.g.*, Ref. [120]) .



**Figure A.6:** Master curves for the data of Fig. A.5: a) The gels with and without magnetic particles (the latter one in the parallel orientation) and b) the gels with different orientations (parallel and perpendicular) can be rescaled onto the same master curve (see text for details).

Clearly, further experiments are needed to determine to what extent the gel formation is controlled by diffusive and/or relaxation processes. Experiments that are done as a function of sample thickness will undoubtedly shed new light on this important issue.



---

# Appendix B

## Comparison to the first model

Before we discuss the stability of the above solution, let us briefly review a first approach we have published in the beginning of our work on the reorientation phenomena (see Refs. [2, 3]). This first approach differs from the present one (which we used also in our later publications, see Refs. [4, 117]) in the notation and some assumptions, as summarized in the following table.

	Refs. [2, 3]	Refs. [4, 117]
variables describing $\hat{n}$	$n_x, n_y, n_z$ <sup>1</sup>	$\theta, \phi$
normalization of $\hat{p}$	none	$p_x = 0, p_z = \sqrt{1 - p_x^2}$
free variables	$u, n_x$	$u, \theta, \phi, v_x, v_y, v_z, P, s^{(n)}, s^{(s)}$

The macroscopic dynamic equations we found in this earlier work vary only in the notation and the number of free variables from the present approach, so the spatially homogeneous state in Refs. [2, 3] is equivalent to Eq. (3.49)

$$\left[ \frac{\lambda + 1}{2} - \lambda n_x^2 \right] \dot{\gamma} = \frac{B_1}{\gamma_1} n_x n_z + \frac{B_0}{\gamma_1} n_x (1 - n_z), \quad (\text{B.1})$$

with  $n_z = \sqrt{1 - n_x^2}$ . In the lowest order in small quantities,<sup>2</sup> the linearized set of equations for stationary instabilities are<sup>3</sup>

$$0 = A_u q \frac{B_1}{\gamma_1} n_z - A_{n_y} \left( \frac{B_1}{\gamma_1} + \frac{K_1}{\gamma_1} q^2 \right), \quad (\text{B.2})$$

$$0 = A_u \lambda_p q \left[ -K q^4 + B_0 (1 - n_z) q^2 - B_1 (n_z^2 q^2 + n_x^2 q^2) - B_0 q_z^2 \right] + A_{n_y} \lambda_p B_1 n_z q^2, \quad (\text{B.3})$$

---

<sup>1</sup>The normalization of  $\hat{n}$  is ensured by the use of transverse Kronecker deltas in the (quasi-) currents (see Sect. 3.1 above).

<sup>2</sup>Due to typical values for low molecular weight liquid crystals, we expect  $n_x$  and  $q_z^2/q^2$  to be small.

<sup>3</sup>In this approach we did not sum up the splay of the director ( $1/2 K_1 (\nabla_i n_i)^2$ ) and the bending of the layers ( $1/2 K (\nabla_{\perp}^2 u)^2$ ) into a single term, but used both terms separately.

where we used an ansatz of the type of Eq. (3.46), with  $A_i$  denoting the amplitude of the variable  $i$ . For typical values, taken from low molecular weight liquid crystals (see Technical Note 3.2 on page 37), we approximated Eq. (B.2) with  $A_{n_y} \approx A_u q n_z$  and found, in lowest order in  $n_x$ , the critical values

$$n_{x,c}^2 = 4 \frac{B_0}{B_0 - 2B_1} q_z \sqrt{\frac{K}{B_0}} \quad \text{and} \quad (\text{B.4})$$

$$q_c^2 = q_z \sqrt{\frac{B_0}{K}}, \quad (\text{B.5})$$

with a somewhat surprising divergence of  $n_{x,c}$  for  $B_0 = 2B_1$ . To investigate this point in more detail, we now use the equivalent set of variables and equations, but with the correct normalization of  $\hat{p}$  and the notation defined in Sect. 3.1. We expand Eqs. (3.54, 3.55) in power series in  $\theta_0$  (up to  $\theta_0^2$ ) and take only the terms connected with  $\phi$  and  $u$ .

$$0 = A_\phi \frac{B_1}{\gamma_1} \theta_0 - A_u \frac{B_1}{\gamma_1} q \quad (\text{B.6})$$

$$0 = -A_u \lambda_p \left[ B_1 q^2 + K q^4 + B_0 q_z^2 - \frac{1}{2} \theta_0^2 q^2 (B_0 + 2B_1) \right] + A_\phi \lambda_p B_1 \theta_0 q \quad (\text{B.7})$$

The solvability condition of Eqs. (B.6, B.7) defines the neutral curve  $\theta_0(q)$  and its minimum directly gives the critical values  $\theta_c$  and  $q_c$  (within the approximations of this section).

$$q_c^2 = q_z \sqrt{\frac{B_0}{K}} \quad (\text{B.8})$$

$$\theta_c^2 = 4 q_z \frac{B_0}{B_0 + 2B_1} \sqrt{\frac{K}{B_0}} \quad (\text{B.9})$$

$$\hat{\gamma}_c = 4 \frac{B_1}{\gamma_1(\lambda + 1)} \sqrt{q_z \frac{B_0}{B_0 + 2B_1} \sqrt{\frac{K}{B_0}}} \quad (\text{B.10})$$

The differences between Eq. (B.4) and Eqs. (B.9) and (B.10) are mainly due to the correct normalization of  $\hat{p}$  [see Eqs. (3.40 – 3.42)].

To summarize, we conclude that our former results are a special case of the present analysis when the correct normalization of  $\hat{p}$  is implemented. Especially the divergence of the critical values at  $B_0 = 2B_1$  is found to be due to the lack of the normalization of  $\hat{p}$  in Ref. [3].



---

## Appendix C

# Generating the set of governing equations

Since the theoretical methods used in this work (irreversible thermodynamics, linear and weakly nonlinear stability analysis) offer well defined algorithms for the generation and analysis of macroscopic hydrodynamic equations, we performed parts of the calculation using Maple. In this appendix we describe the key ingredients of a suitable Maple program. The aims of such a program are twofold. First, Maple offers an easy way to handle complex analytic equations and, second, Maple allows to generate automatically from these analytic equations the corresponding Fortran code. This appendix is not intended to provide a complete listing of the Maple program but rather to demonstrate the principal procedure on some selected topics.

### C.1 Definitions and structuring the equations

To generate the governing equations for our numerical calculations, we start with the balance equations for the unknown quantities (3.26 – 3.31). The major task is to determine the reversible and irreversible currents in these equations. For both kinds of currents we need the thermodynamic conjugates. Consequently, we use this calculation as a tutorial example. In Tab. C.1 we summarize the notation used in the Maple program. The syntax we use is based on Maple V Release 5.1. Some features of this program might take a different form in more recent releases of Maple. Throughout this appendix we will assume that all variables are only functions of two spatial coordinates ( $y$  and  $z$ ). For more details about this approximation see the discussion of Fig. 2.4 on page 20. A straightforward way to define the energy density starts with the notation of all relevant quantities.

```
# useful libraries
restart:gc():
with(linalg):readlib(maylor):readlib(coeftayl):
with(codegen,fortran):
randomize():
```

APPENDIX C. GENERATING THE SET OF GOVERNING EQUATIONS

Quantity	Analytic	Maple
Director	$\hat{n} = (n_x, n_y, n_z)$ $\hat{n} = (\theta, \phi)$	$n := \mathbf{vector}([nx, ny, nz]):$ $ns := \mathbf{vector}([t, f]):$
Kronecker symbol	$\delta_{ij}$ $\delta_{ij}^\perp$	$\mathit{delta}[i, j]$ $\mathit{dperp}[i, j]$
Flow alignment tensor	$\lambda_{ijk}$	$\mathit{lambda1}[i, j, k]$
Flow alignment parameter	$\lambda$	$l$
Tilt angle	$\theta(y, z) = \theta_0 + \eta\theta_1(y, z)$	$t = t0 + a*t1(y, z)$
Shear rate	$\dot{\gamma}$	$\mathit{gd}$
Energy density	$\epsilon$	$e$
Elastic constants of the director	$K_1^{(n)}, K_2^{(n)}, K_3^{(n)}$	$\mathit{kn1}, \mathit{kn2}, \mathit{kn3}$
Elastic constants of the layers	$K_1^{(s)}, K_3^{(s)}, B_0$	$\mathit{ks1}, \mathit{ks3}, \mathit{b0}$
Coupling director $\leftrightarrow$ layers	$B_1$	$\mathit{b1}$
Free energy contributions due to the strength of the order parameter	$L_0, L_{ij}, M_{ijk}$	$\mathit{l0}, \mathit{l1}[i, j], \mathit{ms}[i, j, k]$
Viscosity tensor	$\nu_{ijkl}$	$\mathit{nua}[i, j, k, l]$
Expansion parameter	$\eta$	$a$

**Table C.1:** Overview over the notation used in the Maple program.

```

# spatial coordinates
r := vector( [x, y, z] ):
# director
n := vector( [nx(y, z), ny(y, z), nz(y, z)] ):
# layer normal
p := vector( 3 ):
p[1] := 0:
p[2] := -diff( u(y, z), y ):
p[3] := sqrt( 1-p[2]^2 ):
# velocity and its gradient
v := vector( [vx(y, z), vy(y, z), vz(y, z)] ):
va := vector( [
    seq( v[ii] + gd*delta[ii, 1]*z, ii=1..3)
] ):
Gamma_1 := array( [
    seq( [

```

```

        seq( diff(va[ii], r[ij]), ij=1..3)],
        ii=1..3)]
    ):
    # gradient of the
    # strength of the order parameter
    dds1 := vector(3, [0, diff(ds(y,z), y), diff(ds(y,z), z)]):
    # flow alignment tensor
    lambda1 := array(1..3, 1..3, 1..3, [
        seq( [
            seq( [
                seq(
                    ((l-1)*dperp[ii, ij]*n[ik]
                    + (l+1)*dperp[ii, ik]*n[ij]),
                    ik=1..3)],
                ij=1..3)],
            ii=1..3)]
        ):
    # (preliminary) expansion
    # of the variables
    small := { nx(y,z)=sin(t0 + a*t1(y,z))*cos(a*f1(y,z)),
        ny(y,z)=sin(t0 + a*t1(y,z))*sin(a*f1(y,z)),
        nz(y,z)=cos(t0 + a*t1(y,z)),
        ds(y,z) = ds0+a*ds1(y,z),1
        ...
    }:
```

The easiest way to determine the thermodynamic conjugates is to calculate them as variations of the energy density  $\epsilon$ . In the linear part of this work, we have argued that certain terms in the energy density can be neglected or combined. For completeness we will first keep all terms and only simplify the energy density for the linear calculations. The full energy density in Maple reads.<sup>2,3</sup>

```

e := 1/2*ks1*( add( diff( p[ii], r[ii]), ii=1..3))^2
    + 1/2*ks3*dotprod( crossprod(p, curl(p, x,y,z), 'orthogonal'),
        crossprod(p, curl(p, x,y,z), 'orthogonal'),
        'orthogonal')
    + 1/2*kn1*( add( diff( n[ii], r[ii]), ii=1..3))^2
    + 1/2*kn2*( dotprod( n, curl(n, x,y,z), 'orthogonal'))^2
    + 1/2*kn3*dotprod( crossprod(n, curl(n, x,y,z), 'orthogonal'),
        crossprod(n, curl(n, x,y,z), 'orthogonal'),
        'orthogonal')
```

<sup>1</sup>Note that the expansion parameter in the Maple program is called  $\mathbf{a}$  whereas it is called  $\eta$  in Chapter 6.

<sup>2</sup>In this version we have not distinguished between strength of the nematic and smectic order parameter ( $\mathbf{ds}$  may be the one or the other). In case one considers the strength of the smectic order parameter,  $\mathbf{ms}[\mathbf{ia}, \mathbf{ib}, \mathbf{ic}]$  is zero.

<sup>3</sup> $\mathbf{curl}(\mathbf{v}, \mathbf{x}, \mathbf{y}, \mathbf{z})$  is a user defined procedure which calculates the curl of a vector  $\mathbf{v}$  with respect to the given set of spatial coordinates  $(\mathbf{x}, \mathbf{y}, \mathbf{z})$ .

```

+ 1/2*b0*( 2 - n[3]
            - sqrt( add(
                    (delta[ii,3]-diff(u(y,z), r[ii]))^2,
                    ii=1..3))
            )^2
+ 1/2*b1*dotprod( crossprod(n, p, 'orthogonal'),
                  crossprod(n, p, 'orthogonal'),
                  'orthogonal')
+ 1/2*I0*ds^2
+ 1/2*add( add(
            l1[ii,ij]*dds1[ii]*dds1[ij],
            ij=1..3), ii =1..3)
+ add( add( add(
            ms[ii,ij,ik]*diff(n[ij], r[ii])*dds1[ik],
            ik=1..3), ij=1..3), ii=1..3):

```

To get the thermodynamic forces we have to calculate variational derivatives of the energy density. For this purpose we will substitute the variable in question (or its derivative) by a newly defined constant and take the derivative with respect to this new constant. In the end of the procedure the original variable is substituted back. For example, the thermodynamic force connected with the director  $n_i$  and  $\nabla_i n_j$  ( $hc1[ia]$  and  $hc3[ia,ib]$ , respectively) can be determined by procedures of the following type.

```

# variational derivatives
hx_1 := subs( nx=nx(y,z), diff( subs( nx(y,z)=nx, e), nx)):
hx_2y := subs( nx_y=diff(nx(y,z),y),
              diff(
                subs( diff(nx(y,z),y)=nx_y, e),
                nx_y)
              ):
hx_2z := subs( nx_z=diff(nx(y,z),z),
              diff(
                subs( diff(nx(y,z),z)=nx_z, e),
                nx_z)
              ):
# thermodynamical conjugates
hc1 := array(1..3):
hc3 := array(1..3, 1..3):
hc1[1] := subs( small,
              hx_1 - diff(hx_2y, y) - diff(hx_2z, z)
              ):
hc3[1,1] := 0:
hc3[1,2] := subs( small, hx_2y):
hc3[1,3] := subs( small, hx_2z):
...

```

With the substitution with `small` the spatially homogeneous part of the equations can easily be separated from the expansion terms in `a`. The reversible and dissipative currents

can be constructed using suitable formulations of the coupling parameters. As a tutorial example we will use the quasi-current of the director

$$Y_i = -\frac{1}{2}\lambda_{ijk}\nabla_j v_k + \frac{1}{\gamma_1}\delta_{ik}^\perp h_k.$$

```

for ii from 1 to 3 do
  Yrc1[ii] := subs( small,
    add( add(
      -1/2*lambda1[ii, ij, ik]*diff(va[ik], r[ij]),
      ij=1..3), ik=1..3)
    ):
  Ydc1[ii] := 1/gamma1*add( dperp[ii, ij]*hc1[ij], ij = 1..3):
od:

```

The quasi currents for the angular director coordinates  $Yrs1[ia]$  and  $Yds1[ia]$  follow by implementing Eqs. (3.38) and (3.39).

For practical reasons it turned out to be useful to determine first the spatially homogeneous state (for the tilt angle  $sol\_gd$  and for the strength of the nematic order parameter  $sol\_ds0$ ) from something like

```

sol_gd := solve(
  simplify( coeftayl( Yrs1[1] + Yds1[1], a=0, 0)) = 0,
  gd)

```

And use this result (along with the analogous expression for the spatially homogeneous correction of the strength of the nematic order parameter) to eliminate the shear rate from the governing equations and to use the tilt angle as the control parameter. In order to save computation time and memory, it is useful to expand first the coupling parameters (like the viscosity tensor  $nu[ia, ib, ic, id]$ ) and the thermodynamic conjugates up to the order needed (here called  $m\_ord$ ). In a second step we calculate the currents.

```

# distance to the critical tilt angle
dev := {t0 = t0 + a^2*eps}:
# spatially homogeneous states
sols := {gd = sol_gd, ds0 = sol_ds0}:
# expansion of the tensors in a
nu := array(0..m_ord, 1..3, 1..3, 1..3, 1..3):
for ii from 0 to m_ord do
  for ij from 1 to 3 do
    for ik from 1 to 3 do
      for il from 1 to 3 do
        for im from 1 to 3 do
          nu[ii, ij, ik, il, im] :=
            simplify(coeftayl(
              subs( small, sols, dev, nua[ij, ik, il, im]),
              a=0, ii)):
        od:
      od:
    od:
  od:

```

```

    od:
  od:
od:

```

Similarly to the viscosity tensor, all previously defined quantities must be expanded in the small quantity  $\mathbf{a}$ . The expanded quantities carry a similar name<sup>4</sup> and have a new first index which counts the order in the small quantity. Using the expanded quantities, we now construct the (quasi-) currents of the balance equations. Here we show the dissipative part of the stress tensor as an example.

```

# stress tensor ...
sd := array(0..m_ord, 1..3, 1..3):
for ii from 0 to m_ord do
  for ij from 1 to 3 do
    for ik from 1 to 3 do
      sd[ii, ij, ik] :=
        add( add( add(
          - nu[ip, ij, ik, il, im]*Gamma[ii-ip, il, im],
          ip = 0..ii), il = 1..3), im = 1..3):
    od:
  od:
od:
# ... and its divergence
dsd := array(0..m_ord, 1..3):
for ii from 0 to m_ord do
  for ij from 1 to 3 do
    dsd[ii, ij] := add( diff(sd[ii, ij, ik], r[ik]), ik = 1..3):
  od:
od:

```

It turned out to be more efficient to keep the governing equations split into three parts: the convective term, the reversible and the irreversible (quasi-) currents (called  $\text{Glk}[\mathbf{ia}, \mathbf{ib}]$ ,  $\text{Glr}[\mathbf{ia}, \mathbf{ib}]$  and  $\text{Gld}[\mathbf{ia}, \mathbf{ib}]$ , respectively).

## C.2 Linearization and the adjoint problem

Most of the work is already done.  $\text{Glk}[\mathbf{ia}, \mathbf{ib}]$ ,  $\text{Glr}[\mathbf{ia}, \mathbf{ib}]$  and  $\text{Gld}[\mathbf{ia}, \mathbf{ib}]$  contain all existing terms up to the order  $\mathbf{m\_ord}$ . Using suitable ansätze for the unknown quantities (see, *e.g.*, Tab. 3.3) we can generate the linear set of equations from the  $\mathbf{ia} = 1$  of the equations.

```

small_ex := { t1(y, z) = At*sin(qz*z)*cos(q*y),
              f1(y, z) = Af*cos(qz*z)*sin(q*y),
              ...
            }:
# amplitude vector
Am := array([At, Af, Au, Avx, Avy, Avz, Ap, Ads]):

```

---

<sup>4</sup>Gamma and nu are, *e.g.*, the expanded versions of  $\text{Gamma1}$  and  $\text{nua}$ , respectively.

```

Mr := array(1..8,1..8):
...
for ia from 1 to 8 do
  for ib from 1 to 8 do
    if ia = ib then
      Ad[ia,ib] := 1:
    else
      Ad[ia,ib] := 0:
    fi;
  od;
od;
# extracting the matrix
for ii from 1 to 8 do
  for ij from 1 to 8 do
    for ik from 1 to 8 do
      d_3[ik] := Ad[ij,ik];
    od;
    Mr[ii,ij] :=
      factor(
        coeftayl(
          subs( small_ex, Glr[1,ii]/a ),
          [Am[1], Am[2], Am[3], Am[4], Am[5], Am[6], Am[7], Am[8]]
            = [0, 0, 0, 0, 0, 0, 0, 0],
          [d_3[1], d_3[2], d_3[3], d_3[4], d_3[5], d_3[6], d_3[7],
            d_3[8]]
        )
      );
    Md[ii,ij] := ...
  od;
od;
# dividing by the spatial dependences
a := 1:
Mr2 := array(1..8,1..8):
...
M_ex := array( [ sin(qz*z)*cos(q*y), cos(qz*z)*sin(q*y),
...
                ]):
for ii from 1 to 8 do
  for ij from 1 to 8 do
    Mr2[ij,ii] := simplify( Mr[ij,ii]/M_ex[ij] ):
    Md2[ij,ii] := ...
  od:
od:
for ii from 1 to 8 do
  for ij from 1 to 8 do
    Ma2[ii,ij] := Mr2[ii,ij] + Md2[ii,ij] + Mk2[ii,ij]:

```

```

    od:
od:
    # exporting to Fortran
fortran(Ma2, precision=double, optimized, filename="mpl-lineq.f"):

```

The last step is now to solve the linear system of equations, which can be done by standard numerical techniques (like LU-decomposition and iterative improvement of eigen vectors).

As described in Chapter 6, the adjoint problem can be deduced directly from the linear problem by changing the sign of the spatial derivatives ( $\nabla_i \rightarrow -\nabla_i$ ) and transposing the matrix. Consequently its numerical implementation is straightforward along the lines shown above.

## C.3 Hierarchy of equations

### C.3.1 Order $a^2$

For the equations in higher orders in  $\mathbf{a}$  the major task is to calculate the nonlinearities and to extract from them suitable ansätze for the higher order solutions. The second order nonlinearities are contained in  $\text{Glk}[2, \text{ib}]$ ,  $\text{Glr}[2, \text{ib}]$  and  $\text{Gld}[2, \text{ib}]$ .

```

N2r := array(1..8):
...
for ii from 1 to 8 do
    N2r[ii] := coeftayl( eval( subs( small_ex,
                                Glr[2, ii]
                                )), eps = 0, 0):5
    N2d[ii] := ...
    N2[ii] := N2r[ii] + N2d[ii] + N2k[ii]
od:

```

They determine the ansatz for the second order solution  $\vec{X}_2$ . For the automatic detection of the spatial structure of  $\text{N2}[\text{ia}]$  we use

```

welle := { sin(q*y) = sy, cos(q*y) = cy,
           sin(qz*z) = sz, cos(qz*z) = cz
           }:

```

```

N2o := array(1..8):
for ia from 1 to 8 do
    N2o[ia] := 0:
    for ii from 0 to 2 do
        dum_a := coeftayl( subs( welle, N2[ia] ), sy=0, ii ):
        if (dum_a <> 0) then
            for ij from 0 to 2 do

```

---

<sup>5</sup>We neglect here all terms proportional to `eps` only for efficiency. These terms sum up to zero and cost only computation time and memory.



```

dum_b := coeftayl(dum_a, cy=0, ij):
if (dum_b <> 0) then
  for ik from 0 to 2 do
    dum_c := coeftayl(dum_b, sz=0, ik):
    if (dum_c <> 0) then
      for il from 0 to 2 do
        dum_d := coeftayl(dum_c, cz=0, il):
        if (dum_d <> 0) then
          N2o[ia] := N2o[ia] +
            sin(q*y)^ii*cos(q*y)^ij*sin(qz*z)^ik*cos(qz*z)^il
        fi:
      od:
    fi:
  od:
fi:
od:
fi:
od:
fi:
od:
print(ia, N2o[ia]):
od:

```

Using a very similar procedure as shown above, Maple generates versions of  $N2[ia]$  ( $N2a[ia]$ ) and the linear equations acting on  $\vec{X}_2$  ( $M2[ia,ib]$ ) which are suitable to be exported to Fortran.

```

fortran(M2, precision=double, optimized, filename="mpl-lin2eq.f");
fortran(N2a, precision=double, optimized, filename="mpl-inhom2.f");

```

The absence of a second order term in the amplitude equation, *i.e.*,

$$\langle \vec{X}^+ | N_2(\vec{X}_1 | \vec{X}_1) \rangle = 0 \quad (C.1)$$

follows directly from symmetry considerations.  $N_2(\vec{X}_1 | \vec{X}_1)$  contains only terms with (lateral) wave vectors  $q = 0$  and  $q = 2q_c$  and the only lateral wave vector in  $\vec{X}^+$  is  $q = q_c$ . Thus, the integral vanishes for symmetry reasons.<sup>6</sup>

### C.3.2 Order $a^3$

The third order inhomogeneity consists of three parts:  $N_3(\vec{X}_1 | \vec{X}_1 | \vec{X}_1)$ ,  $N_2(\vec{X}_2 | \vec{X}_1) + N_2(\vec{X}_1 | \vec{X}_2)$  and  $\delta L_2 \vec{X}_1$ . Since they emerge from different orders of our expansion of the governing equations and also contribute to different terms in the amplitude equation, we deal with them separately.

The  $N_3$  term follows directly when inserting the first order solution  $\vec{X}_1$  in the  $a^3$  order of the governing equations. To evaluate the integral arising from the Fredholm theorem,

---

<sup>6</sup>As argued in Chapter 6, this result also leads to the fact that the distance from the critical tilt angle scales as  $a^2$ .

it computationally efficient to split  $N_3$  into two arrays: one containing the prefactors ( $N3[ia, ib]$ ) and one containing the spatial dependences (the powers of  $\cos(qy)$ ,  $\sin(qy)$ , *etc.* are stored in  $pot3[ia, ib, ic]$ ). This separation can be realized by a procedure similar to the one shown on page 104.

```

wellered := { sin(q*y) = sy, cos(q*y) = cy,
              sin(z) = sz, cos(z) = cz
            }:
pot3 := array(1..24, 1..8, 1..4):
potl := array(1..8, 1..4):
N3 := array(1..24, 1..8):7

for ia from 1 to 24 do
  for ib from 1 to 8 do
    N3[ia, ib] := 0:
    for ic from 1 to 4 do
      pot3[ia, ib, ic] := 0:
    od:
  od:
count := 1:
for ii from 0 to 3 do
  dum_a := coeftayl( subs( wellered, N3a[ia] ), cy=0, ii ):
  if (dum_a <> 0) then
    for ij from 0 to 3 do
      dum_b := coeftayl(dum_a, sy=0, ij ):
      if (dum_b <> 0) then
        for ik from 0 to 3 do
          dum_c := coeftayl(dum_b, cz=0, ik ):
          if (dum_c <> 0) then
            for il from 0 to 3 do
              dum_d := coeftayl(dum_c, sz=0, il ):
              if (dum_d <> 0) then
                pot3[ia, count, 1] := ii:
                pot3[ia, count, 2] := ij:
                pot3[ia, count, 3] := ik:
                pot3[ia, count, 4] := il:
                N3[ia, count] :=
                  factor( subs( amp_array, dum_d )):
                count := count + 1:
              fi:
            od:
          fi:
        od:
      fi:
    od:
  od:
fi:

```

---

<sup>7</sup>In  $N3[ia, ib]$  and  $pot3[ia, ib, ic]$  the first index labels the equation ( $ia = 1 \dots 8$  for the reversible terms,  $ia = 9 \dots 16$  for the dissipative currents and  $ia = 17 \dots 24$  for the convective terms) and the labels the terms with different spatial dependences. The third index in  $pot3[ia, ib, ic]$  indicates whether the power of  $\cos(qy)$ , *etc.* is given. In  $potl[ia, ib]$  the second index of  $pot3[ia, ib, ic]$  is skipped.

```

    od:
  fi:
od:
od:

```

To analyze the  $N_2$  terms we extract the third order from  $N_2(\vec{X}_1 + \vec{X}_2|\vec{X}_1 + \vec{X}_2)$  and split it in the same way as  $N_3$  and store the results in additional elements in  $N3[ia, ib]$  and  $pot3[ia, ib, ic]$ . For convenience we also stored the solution of the linear adjoint problem in the same way in  $potl[ia, ib]$  and then integrate.<sup>8</sup>

```

indx3 := array(1..24, 1..8):
for ia from 1 to 8 do
  for ib from 0 to 2 do
    for ic from 1 to 8 do
      dum :=
        int(
          cos(q*y)^(pot3[ia+ib*8, ic, 1]+potl[ia, 1])
          *sin(q*y)^(pot3[ia+ib*8, ic, 2]+potl[ia, 2])
          *cos(z)^(pot3[ia+ib*8, ic, 3]+potl[ia, 3])
          *sin(z)^(pot3[ia+ib*8, ic, 4]+potl[ia, 4]),
          y = -Pi/q..Pi/q
        ):
      dum := int(dum, z = -Pi/2 .. Pi/2):
      if (dum <> 0) then
        indx3[ia + ib*8, ic] := dum:
      fi:
    od:
  od:
od:

```

To get the (not yet normalized) nonlinear coefficient of the amplitude equation, the elements of  $indx3$  have to be multiplied by the prefactors stored in  $N3$  and the amplitudes of the adjoint linear solution and, finally, summed up (this last step will be done in a Fortran program).

```

g := array(1..24, 1..8):
for ia from 1 to 8 do
  for ib from 0 to 2 do
    for ic from 1 to 8 do
      g[ia+ib*8, ic] :=
        A1[ia]*N3[ia+ib*8, ic]*indx3[ia+ib*8, ic]:
    od:
  od:
od:
fortran(g, precision=double, filename="mpl-g.f");

```

We use a similar procedure to calculate the linear term in the amplitude equation form  $\langle \vec{X}^+ | \delta L_2 \vec{X}_1 \rangle$ .

---

<sup>8</sup>To limit the length to the minimum necessary, we use for the following steps the dimensionless quantities defined by Eq. (3.47).

## *APPENDIX C. GENERATING THE SET OF GOVERNING EQUATIONS*

---

We now have all necessary ingredients to determine  $g^*$  (as a sum of the elements of  $g[ia, ib]$ ) and  $r_a$ . In Chapter 6 we present the results of these calculations.

---

# Bibliography

- [1] ALLEN, M. P. AND TILDESLEY, D. J. *Computer simulation of liquids*. Clarendon, Oxford, 1987.
- [2] AUERNHAMMER, G. K., BRAND, H. R., AND PLEINER, H. *Destabilization of a layered system by shear flow*. Proceedings of the Freiburger Arbeitstagung Flüssigkristalle **29** (2000), V19.
- [3] AUERNHAMMER, G. K., BRAND, H. R., AND PLEINER, H. *The undulation instability in layered systems under shear flow - a simple model*. Rheol. Acta **39** (2000), 215 – 222.
- [4] AUERNHAMMER, G. K., BRAND, H. R., AND PLEINER, H. *Shear-induced instabilities in layered liquids*. Phys. Rev. E **66** (2002), 061707–1 – 14.
- [5] BENTIVEGNA, F., FERRÉ, J., NÝVLT, M., JAMET, J., IMHOFF, D., CANVA, M., BRUN, A., VEILLET, P., Š. VIŠŇOVSKÝÝ, CHAPUT, F., AND BOILOT, J. *Magnetically textured  $\gamma$ -Fe<sub>2</sub>O<sub>3</sub> nanoparticles in a silica gel matrix: Structural and magnetic properties*. J. Appl. Phys. **83** (1998), 7776 – 7788.
- [6] BENTIVEGNA, F., NÝVLT, M., FERRÉ, J., JAMET, J., BRUN, A., Š. VIŠŇOVSKÝÝ, AND URBAN, R. *Magnetically textured  $\gamma$ -Fe<sub>2</sub>O<sub>3</sub> nanoparticles in a silica gel matrix: Optical and magneto-optical properties*. J. Appl. Phys. **85** (1999), 2270 – 2278.
- [7] BERWEGER, C. D., VAN GUNSTEREN, W. F., AND MÜLLER-PLATHE, F. *Molecular dynamics simulation with an ab initio potential energy function and finite element interpolation: The photoisomerization of cis-stilbene in solution*. J. Chem. Phys. **108** (1998), 8773 – 8781.
- [8] BÖKER, A., KNOLL, A., ELBS, H., ABETZ, V., MÜLLER, A. H. E., AND KRAUSCH, G. *Large scale domain alignment of a block copolymer from solution using electric fields*. Macromolecules **35** (2002), 1319 – 1325.
- [9] BRAND, H. R. AND KAWASAKI, K. *Gradient free energy of nematic liquid crystals with topological defects*. J. Phys. C **19** (1986), 937 – 942.

- [10] BRAND, H. R., LOMDAHL, P. S., AND NEWELL, A. C. *Evolution of the order parameter in situations with broken rotational symmetry*. Phys. Lett. A **118** (1986), 67 – 73.
- [11] BRUINSMA, R. AND RABIN, Y. *Shear-flow enhancement and suppression of fluctuations in smectic liquid crystals*. Phys. Rev. A **45** (1992), 994 – 1008.
- [12] CAR, R. AND PARRINELLO, M. *Unified approach for molecular dynamics and density-functional theory*. Phys. Rev. Lett. **55** (1985), 2471 – 2474.
- [13] CHAIKIN, P. M. AND LUBENSKY, T. C. *Principles of condensed matter physics*. Cambridge University Press, Cambridge, UK, 1995.
- [14] CHANDRASEKHAR, S. *Liquid crystals*. Cambridge University Press, Cambridge, UK, 1977.
- [15] CHEN, P. AND VIÑALS, J. *Lamellar phase stability in diblock copolymers under oscillatory shear flows*. Macromolecules **35** (2002), 4183 – 4192.
- [16] CLARK, N. A. AND MEYER, R. B. *Strain-induced instability of monodomain smectic-A and cholesteric liquid crystals*. Appl. Phys. Lett. **22** (1973), 493 – 494.
- [17] CLUNE, T. AND KNOBLOCH, E. *Pattern selection in rotating convection with experimental boundary conditions*. Phys. Rev. E **47** (1993), 2536 – 2550.
- [18] COHEN, Y., ALBALAK, R. J., DAIR, B. J., CAPEL, M. S., AND THOMAS, E. L. *Deformation of oriented lamellar block copolymer films*. Macromolecules **33** (2000), 6502 – 6516.
- [19] COHEN, Y., BRINKMANN, M., AND THOMAS, E. L. *Undulation, dilation, and folding of a layered block copolymer*. J. Chem. Phys. **114** (2001), 984 – 992.
- [20] COLLIN, D., AUERNHAMMER, G. K., GAVAT, O., MARTINOTY, P., AND BRAND, H. R. *Frozen-in magnetic order in uniaxial magnetic gels: preparation and physical properties*. Macromol. Rapid Commun. (2003), in print.
- [21] CROSS, M. C. *Derivation of the amplitude equation at the Rayleigh-Bénard instability*. Phys. Fluids **23** (1980), 1727 – 1731.
- [22] CROSS, M. C. AND HOHENBERG, P. C. *Pattern formation outside of equilibrium*. Rev. Mod. Phys. **65** (1993), 851 – 1112.
- [23] DE GENNES, P. G. *Phenomenology of short-range-order effects in the isotropic phase of nematic materials*. Phys. Lett. A **30** (1969), 454 – 455.
- [24] DE GENNES, P. G. *Short range order effects in the isotropic phase of nematics and cholesterics*. Mol. Cryst. Liq. Cryst. **12** (1971), 193 – 214.

- 
- [25] DE GENNES, P. G. *An analogy between superconductors and smectic-A*. Solid State Commun. **10** (1972), 753 – 756.
- [26] DE GENNES, P. G. AND PROST, J. *The Physics of Liquid Crystals*. Clarendon Press, Oxford, 1993.
- [27] DE GROOT, S. R. AND MAZUR, P. *Non-equilibrium Thermodynamics*. North-Holland, Amsterdam, 1962.
- [28] DELAYE, M., RIBOTTA, R., AND DURAND, G. *Buckling instability of the layers in a smectic-A liquid crystal*. Phys. Lett. **44A** (1973), 139 – 140.
- [29] DIAT, O., ROUX, D., AND NALLET, F. *Effect of shear on a lyotropic lamellar phase*. J. Phys. II France **3** (1993), 1427 – 1452.
- [30] DROLET, F., CHEN, P., AND VIÑALS, J. *Lamellae alignment by shear flow in a model of a diblock copolymer*. Macromolecules **32** (1999), 8603 – 8610.
- [31] ESCALANTE, J. I. AND HOFFMANN, H. *Nonlinear rheology and flow-induced transition of a lamellar-to-vesicle phase in ternary systems of alkyldimethyl oxide/alcohol/water*. Rheol. Acta **39** (2000), 209 – 214.
- [32] ESPAÑOL, P. AND WARREN, P. *Statistical mechanics and dissipative particle dynamics*. Europhys. Lett. **30** (1995), 191 – 196.
- [33] FALLER, R. *Influence of chain stiffness on the structure and dynamics of polymers in the melt*. PhD thesis, Johannes Gutenberg Universität, Mainz, 2000.
- [34] FENG, Q., PESCH, W., AND KRAMER, L. *Theory of Rayleigh-Bénard convection in planar nematic liquid crystals*. Phys. Rev. A **45** (1992), 7242 – 7256.
- [35] FINKELMANN, H., KOCK, H., AND REHAGE, G. *Investigations on liquid crystalline polysiloxanes 3: Liquid crystalline elastomers—a new type of liquid crystalline material*. Makromol. Chem., Rapid Commun. **2** (1981), 317.
- [36] FOLKES, M. J., KELLER, A., AND SCALISI, F. P. *An extrusion techniques for the preparation of "single-crystals" of block copolymers*. Colloid Polym. Sci. **251** (1973), 1 – 4.
- [37] FORSTER, D., LUBENSKY, T. C., MARTIN, P. C., SWIFT, J., AND PERSHAN, P. S. *Hydrodynamics of liquid crystals*. Phys. Rev. Lett. **26** (1971), 1016 – 1019.
- [38] FRANK, F. C. *On the theory of liquid crystals*. Disc. Faraday Soc. **25** (1958), 19 – 28.
- [39] FREDHOLM, I. *Sur une classe d'équations fonctionnelles*. Acta Math. **27** (1903), 365 – 390.

- [40] FRENKEL, D. AND SMIT, B. *Understanding molecular simulation*. Academic Press, San Diego, London, Boston, New York, Sydney, Tokyo, Toronto, 1998.
- [41] GALLANI, J. L., HILLIOU, L., MARTINOTY, P., DOUBLET, F., AND MAUZAC, M. *Mechanical behavior of side-chain liquid crystalline networks*. J. Phys. II France **6** (1996), 443 – 452.
- [42] GOETHE, J. W. *Die Wahlverwandtschaften*. dtv, München, 1963.
- [43] GRAF, H.-H., KNEPPE, H., AND SCHNEIDER, F. *Shear and rotational viscosity coefficients of two nematic liquid crystals*. Mol. Phys. **77** (1992), 521 – 538.
- [44] GREST, G. G. AND KREMER, K. *Molecular dynamic simulation for polymers in the presence of a heat bath*. Phys. Rev. A **33** (1986), 3628 – 3631.
- [45] GROOT, R. D. AND WARREN, P. B. *Dissipative particle dynamics: Bridging the gap between atomistic and mesoscale simulation*. J. Chem. Phys. **107** (1997), 4423 – 4435.
- [46] GUO, H. AND KREMER, K. *Amphiphilic lamellar model systems under dilation and compression: Molecular dynamics study*. J. Chem. Phys. **118** (2003), 7714 – 7723.
- [47] GUO, H., KREMER, K., AND SODDEMAN, T. *Nonequilibrium molecular dynamics simulation of shear-induced alignment of amphiphilic model systems*. Phys. Rev. E **66** (2002), 061503 (1 – 11).
- [48] GUPTA, V. K., KRISHNAMOORTI, R., CHEN, Z.-R., KORNFELD, J. A., SMITH, S. D., SATKOWSKI, M., AND GROTHAUS, J. T. *Dynamics of shear alignment in a lamellar diblock copolymer: Interplay of frequency, strain amplitude, and temperature*. Macromolecules **29** (1996), 875 – 884.
- [49] HAHN, H., LEE, J. H., BALSARA, N. P., GARETZ, B. A., AND WATANABE, H. *Viscoelastic properties of aligned block copolymer lamellae*. Macromolecules **34** (2001), 8701 – 8709.
- [50] HELFRICH, W. *Deformation of cholesteric liquid crystals with low threshold voltage*. Appl. Phys. Lett. **17** (1970), 531 – 532.
- [51] HELFRICH, W. *Steric interaction of fluid membranes in multilayer systems*. Z. Naturforsch. **33a** (1978), 305 – 315.
- [52] HESS, S. *Irreversible thermodynamics of nonequilibrium alignment phenomena in molecular liquids and in liquid crystals I. derivation of nonlinear constitutive laws, relaxation of the alignment, phase transition*. Z. Naturforsch. **30 a** (1975), 728 – 738.



- 
- [53] HESS, S. *Irreversible thermodynamics of nonequilibrium alignment phenomena in molecular liquids and in liquid crystals II. viscous flow and flow alignment in the isotropic (stable and metastable) and nematic phases.* Z. Naturforsch. **30 a** (1975), 1224 – 1232.
- [54] HOOGERBRUGGE, P. J. AND KOELMAN, J. M. V. A. *Simulating microscopic hydrodynamic phenomena with dissipative particle dynamics.* Europhys. Lett. **19** (1992), 155 – 160.
- [55] HORN, R. G. AND KLÉMAN, M. *Observations on shear-induced textures and rheology of a smectic-A phase.* Ann. Phys. (France) **3** (1978), 229 – 234.
- [56] HUANG, C. C. *Handbook of liquid crystals*, vol. 2A. Wiley-VCH, Weinheim, 1998, ch. V.2: *Physical Properties of non-chiral smectic liquid crystals*, Eds.: D. Demus, J. Goodby, G. W. Gray, H.-W. Spiess, and V. Vill.
- [57] HURAUULT, J. P. *Static distortions of a cholesteric planar structure induced by magnetic or ac electric fields.* J. Chem. Phys. **59** (1973), 2068 – 2075.
- [58] JOHNSON, D. AND SAUPE, A. *Undulation instability in smectic-C phases.* Phys. Rev. A **15** (1977), 2079 – 2085.
- [59] KELLER, A., PEDEMONTE, E., AND WILLMOUTH, F. M. *Macro lattice from segregated amorphous phases of a three block copolymer.* Colloid Polym. Sci. **238** (1970), 385 – 389.
- [60] KHALATNIKOV, I. M. *An introduction to the theory of superfluidity.* W. A. Benjamin, New York, Amsterdam, 1965.
- [61] KOELMAN, J. M. V. A. AND HOOGERBRUGGE, P. J. *Dynamic simulations of hard-sphere suspensions under steady shear.* Europhys. Lett. **21** (1993), 363 – 368.
- [62] KOPPI, K. A., TIRRELL, M., BATES, F. S., ALMDAL, K., AND COLBY, R. H. *Lamellae orientation in dynamically sheared diblock copolymer melts.* J. Phys. II France **2** (1992), 1941 – 1959.
- [63] KUMAR, S. *High-resolution X-ray study of the smectic phases of terephthal-bis-(4n)-alkylanilines.* Phys. Rev. A **23** (1981), 3207 – 3214.
- [64] KUNDLER, I. AND FINKELMANN, H. *Strain-induced director reorientation in nematic liquid single crystal elastomers.* Macromol. Rapid Commun. **16** (1995), 679 – 686.
- [65] KUNDLER, I., NISHIKAWA, E., AND FINKELMANN, H. *Nematic and smectic liquid crystal elastomers: Influence of external stress parallel and perpendicular to the director.* Macromol. Symp. **117** (1997), 11 – 19.
- [66] KÜPFER, J. AND FINKELMANN, H. *Nematic liquid single crystal elastomers.* Macromol. Rapid Commun. **12** (1991), 717 – 726.

- [67] LANDAU, L. D. AND LIFSCHITZ, E. M. *Statistical Physics/I*. Pergamon Press, Oxford, UK, 1980.
- [68] LANGELA, M., WIESNER, U., SPIESS, H. W., AND WILHELM, M. *Microphase reorientation in block copolymer melts as detected via FT rheology and 2D SAXS*. *Macromolecules* **35** (2002), 3198 – 3204.
- [69] LAURER, J. H., SCOTT PINHEIRO, B., POLIS, D. L., AND WINEY, K. I. *Persistence of surface-induced alignment in block copolymers upon large-amplitude oscillatory shear processing*. *Macromolecules* **32** (1999), 4999 – 5003.
- [70] LEHMANN, O. *Über fließende Krystalle*. *Z. Phys. Chem.* **4** (1889), 462 – 462.
- [71] LEIST, H., MARING, D., THURN-ALBRECHT, T., AND WIESNER, U. *Double flip of orientation for a lamellar diblock copolymer under shear*. *J. Chem. Phys.* **110** (1999), 8225 – 8228.
- [72] LEMAIRE, E., BOSSIS, G., AND GRASSELLI, Y. *Field induced structure in magneto and electro-rheological fluids*. *J. Phys. II France* **2** (1992), 359.
- [73] LEUNINGER, H. *Orientierungsverhalten von lamellaren PS-b-PI Diblockcopolymeren unter Scherung*. PhD thesis, Johannes Gutenberg-Universität, Mainz, 1999.
- [74] LITSTER, J. D., ALS-NIELSEN, J., BIRGENEAU, R. J., DANA, S. S., DAVIDOV, D., GARCIA-GOLDING, F., KAPLAN, M., SAFINYA, C. R., AND SCHAETZING, R. *High resolution X-ray and light scattering studies of bilayer smectic-A compounds*. *J. Phys. Coll. C3 suppl.* **4** **40** (1979), C3-339 – C3-344.
- [75] LIU, M. *Hydrodynamic theory near the nematic–smectic-A transition*. *Phys. Rev. A* **19** (1979), 2090 – 2094.
- [76] MAIER, W. AND SAUPE, A. *Eine einfache molekular-statistische Theorie der nematischen kristallinflüssigen Phase. Teil I*. *Z. Naturforsch.* **A14** (1959), 882 – 889.
- [77] MAIER, W. AND SAUPE, A. *Eine einfache molekular-statistische Theorie der nematischen kristallinflüssigen Phase. Teil II*. *Z. Naturforsch.* **A15** (1960), 287 – 292.
- [78] MANNEVILLE, P. *Dissipative structures and weak turbulence*. Academic Press, Boston, USA, 1990.
- [79] MARNIGNAN, J., PARODI, O., AND DUBOIS-VIOLETTE, E. *Instabilities in smectics-A submitted to an alternative shear flow I. — theory*. *J. Phys. France* **44** (1983), 263 – 271.
- [80] MARLOW, S. W. AND OLMSTED, P. D. *The effect of shear flow on the Helfrich interaction in lyotropic lamellar systems*. *Eur. Phys. J. E* **8** (2002), 485 – 497.

- 
- [81] MARTIN, P. C., PARODI, O., AND PERSHAN, P. S. *Unified hydrodynamic theory for crystals, liquid crystals, and normal fluids*. Phys. Rev. A **6** (1972), 2401 – 2420.
- [82] MARTINOTY, P. AND BADER, M. *Measurements of the birefringence induced in liquids by ultrasonic waves: application to the study of the isotropic phase of PAA near the transition point*. J. Phys. France **42** (1981), 1097 – 1102.
- [83] McMILLAN, W. L. *Time-dependent Landau theory for the smectic-A–nematic phase transition*. Phys. Rev. A **9** (1974), 1720 – 1724.
- [84] MOROZOV, A. N. AND FRAAIJE, J. G. E. M. *Orientations of the lamellar phase of block copolymer melts under oscillatory shear flow*. Phys. Rev. E **65** (2002), 031803–1 – 3.
- [85] MÜLLER, S., BÖRSCHIG, C., GRONSKI, W., SCHMIDT, C., AND ROUX, D. *Shear-induced states of orientation of the lamellar phase of  $C_{12}E_4$ /water*. Langmuir **15** (1999), 7558 – 7564.
- [86] MÜLLER-PLATHE, F. *Reversing the perturbation in nonequilibrium molecular dynamics: An easy way to calculate the shear viscosity of fluids*. Phys. Rev. E **59** (1999), 4894 – 4898.
- [87] NALLET, F., ROUX, D., AND PROST, J. *Hydrodynamics of lyotropic smectics: a dynamic light scattering study of dilute lamellar phases*. J. Phys. France **50** (1989), 3147 – 3165.
- [88] NETTESHEIM, F., ZIPFEL, J., OLSSON, U., RENTH, F., LINDNER, P., AND RICHTERING, W. *Pathway of the shear-induced transition between planar lamellae and multilamellar vesicles as studied by time-resolved scattering techniques*. Langmuir **19** (2003), 3603 – 3618.
- [89] NEWELL, A. C. AND WHITEHEAD, J. A. *Finite bandwidth, finite amplitude convection*. J. Fluid Mech. **38** (1969), 279 – 303.
- [90] NISHIKAWA, E. AND FINKELMANN, H. *Orientation behavior of smectic polymer networks by uniaxial mechanical fields*. Macromol. Chem. Phys. **198** (1997), 2531 – 2549.
- [91] NISHIKAWA, E. AND FINKELMANN, H. *Smectic-A liquid single crystal elastomers – strain induced break-down of smectic layers*. Macromol. Chem. Phys. **200** (1999), 312 – 322.
- [92] NISHIKAWA, E., FINKELMANN, H., AND BRAND, H. R. *Smectic-A liquid single crystal elastomers showing macroscopic in-plane fluidity*. Macromol. Rapid Commun. **18** (1997), 65 – 71.
- [93] NOIREZ, L. *Shear induced smectic-A–smectic-C transition in side-chain liquid crystalline polymers*. Phys. Rev. Lett. **84** (2000), 2164 – 2167.

- [94] NOIREZ, L. AND LAPP, A. *Shear flow induced transition from liquid-crystalline to polymer behavior in side-chain liquid crystal polymers*. Phys. Rev. Lett. **78** (1997), 70 – 73.
- [95] NOIREZ, L., PÉPY, G., AND LAPP, A. *From phase orientation to phase destruction: Opposite shear flow induced effects*. Physica B **234 – 236** (1997), 252 – 253.
- [96] OHNO, H. (SIGMA-HI-CHEMICAL, JAPAN). *private communication*.
- [97] OKUZAKI, H. AND OSADA, Y. *Effects of hydrophobic interaction on the cooperative binding of a surfactant polymer network*. Macromolecules **27** (1994), 502 – 506.
- [98] OKUZAKI, H. AND OSADA, Y. *Ordered-aggregate formation by surfactant-charged gel interaction*. Macromolecules **28** (1995), 380 – 382.
- [99] OKUZAKI, H. AND OSADA, Y. *Role and effect of cross-linkage on the polyelectrolyte–surfactant interaction*. Macromolecules **28** (1995), 4554 – 4557.
- [100] OSWALD, P. AND BEN-ABRAHAM, S. I. *Undulation instability under shear in smectic-A liquid crystal*. J. Phys. France **43** (1982), 1193 – 1197.
- [101] PANIZZA, P., ARCHAMBAULT, P., AND ROUX, D. *Effects of shear on the smectic-A phase of thermotropic liquid crystals*. J. Phys. II France **5** (1995), 303 – 311.
- [102] PASCAL, B. *Pensées*. Guillaume Desprez, Paris, France, 1670.
- [103] PLEINER, H. AND BRAND, H. R. *Macroscopic behavior of a biaxial mixture of uniaxial nematics versus hydrodynamics of a biaxial nematic liquid crystal*. J. Phys. France **46** (1985), 615 – 620.
- [104] PLEINER, H. AND BRAND, H. R. *Pattern Formation in Liquid Crystals*. Springer, New York, 1996, ch. 2: *Hydrodynamics and Electrohydrodynamics of Liquid Crystals*, Eds.: A. Buka and L. Kramer.
- [105] PLEINER, H. AND BRAND, H. R. *Nonlinear hydrodynamics of strongly deformed smectic-C and C\* liquid crystals*. Physica A **265** (1999), 62 – 77.
- [106] POLIS, D. L., SMITH, S., TERRILL, N. J., RYAN, A. J., MORSE, D. C., AND WINEY, K. I. *Shear-induced lamellar rotation observed in a diblock copolymer by in situ small-angle X-ray scattering*. Macromolecules **32** (1999), 4668 – 4676.
- [107] POLIS, D. L., WINEY, K. I., RYAN, A. J., AND SMITH, S. *Nature of viscoelasticity in lamellar block copolymers: Contraction correlated to strain localization*. Phys. Rev. Lett. **83** (1999), 2861 – 2864.

- 
- [108] QIAO, L., RYAN, J., AND WINEY, K. I. *A correlation between the lamellar contraction and applied shear stress in diblock copolymers.* *Macromolecules* **35** (2002), 3596 – 3600.
- [109] REINITZER, F. *Sitzungsber. d. Wien Ak.* **94** (1888), 719.
- [110] REINITZER, F. *Sitzungsber. d. Wien Ak.* **97** (1888), 167.
- [111] RIBOTTA, R. AND DURAND, G. *Mechanical instabilities of smectic-A liquid crystals under dilative or compressive stresses.* *J. Phys. France* **38** (1977), 179 – 204.
- [112] ROSENSWEIG, R. E. *Ferrohydrodynamics.* Cambridge University Press, London, 1985.
- [113] SAFINYA, C. R., ROUX, D., SMITH, G. S., SINHA, S. K., DIMON, P., CLARK, N. A., AND BELLOCQ, A. M. *Steric interactions in a model multimembrane systems: A synchrotron X-ray study.* *Phys. Rev. Lett.* **57** (1986), 2718 – 2721.
- [114] SAFINYA, C. R., SIROTA, E. B., AND PLANO, R. J. *Nematic to smectic-A phase transition under shear flow: A nonequilibrium synchrotron X-ray study.* *Phys. Rev. Lett.* **66** (1991), 1986 – 1989.
- [115] SCHLÜTER, A., LORTZ, D., AND BUSSE, F. *On the stability of steady finite amplitude convection.* *J. Fluid Mech.* **23** (1965), 129 – 144.
- [116] SODDEMANN, T. *Non-Equilibrium Molecular Dynamics Study of an Amphiphilic Model System.* PhD thesis, Johannes Gutenberg Universität, Mainz, 2000.
- [117] SODDEMANN, T., AUERNHAMMER, G. K., GUO, H. X., DÜNWEIG, B., AND KREMER, K. *Shear-induced undulations of smectic-A: Molecular simulations vs. analytic theory.* in preparation.
- [118] SODDEMANN, T., DÜNWEIG, B., AND KREMER, K. *A generic computer model for amphiphilic systems.* *Eur. Phys. J. E* **6** (2001), 409 – 419.
- [119] STANGLER, S. AND ABETZ, V. *Orientation behavior of AB and ABC block copolymers under large amplitude oscillatory shear in bulk and in concentrated solution.* *e-Polymers* (2002), 1 – 21.
- [120] STEIN, P., ASSFALG, N., FINKELMANN, H., AND MARTINOTY, P. *Shear modulus of polydomain, mono-domain and non-mesomorphic side-chain elastomers: Influence of the nematic order.* *Eur. Phys. J. E* **4** (2001), 255 – 262.
- [121] THURN-ALBRECHT, T., DEROUCEY, J., RUSSELL, T. P., AND KOLB, R. *Pathways towards electric fields induced alignment of block-copolymers.* *Macromolecules* **35** (2002), 8106 – 8110.
- [122] VERLET, L. *Computer "experiments" on classical fluids. i. thermodynamical properties of lennard-jones molecules.* *Phys. Rev.* **159** (1967), 98 – 102.

- [123] VIGILD, M. E., CHU, C., SUGIYAMA, M., CHAFFIN, K. A., AND BATES, F. S. *Influence of shear on the alignment of a lamellae-forming pentablock copolymer*. *Macromolecules* (2001).
- [124] VON BERLEPSCH, H. AND DE VRIES, R. *Weakly charged lamellar bilayer system: Interplay between thermal undulations and electrostatic repulsion*. *Eur. Phys. J. E* **1** (2000), 141 – 152.
- [125] VORLÄNDER, D. *Die Erforschung der molekularen Gestalt mit Hilfe der kristallinen Flüssigkeiten*. *Z. Phys. Chem.* **105** (1923), 211 – 254.
- [126] VORLÄNDER, D. *Über die Natur der Kohlenstoffketten in kristallin-flüssigen Substanzen*. *Z. Phys. Chem.* **126** (1929), 449 – 472.
- [127] WANG, H., NEWSTEIN, M. C., KRISHNAN, A., BALSARA, N. P., GARETZ, B. A., HAMMOUDA, B., AND KRISHNAMOORTI, R. *Ordering kinetics and alignment of block copolymer lamellae under shear flow*. *Macromolecules* **32** (1999), 3695 – 3711.
- [128] WEILEPP, J. *Makroskopische Eigenschaften flüssigkristalliner Elastomere*. PhD thesis, Universität Bayreuth, 1999.
- [129] WEILEPP, J. AND BRAND, H. R. *Director reorientation in nematic-liquid-single-crystal elastomers*. *Europhys. Lett.* **34** (1996), 495 – 500.
- [130] WEILEPP, J. AND BRAND, H. R. *Undulation instability in smectic-A liquid single crystal elastomers*. *Macromol. Theory Simul.* **7** (1998), 91 – 96.
- [131] WEILEPP, J., ZANNA, J., ASSFALG, N., STEIN, P., HILLIOU, L., MAUZAC, M., FINKELMANN, H., BRAND, H. R., AND MARTINOTY, P. *Rheology of liquid crystalline elastomers in their isotropic and smectic-A state*. *Macromolecules* **32** (1999), 4566 – 4574.
- [132] WIESNER, U. *Lamellar diblock copolymers under large amplitude oscillatory shear flow: order and dynamics*. *Macromol. Chem. Phys.* **198** (1997), 3319 – 3352.
- [133] WILLIAMS, D. R. M. AND MACKINTOSH, F. C. *Shear of diblock copolymer lamellae: width changes and undulation instabilities*. *Macromolecules* **27** (1994), 7677 – 7680.
- [134] WILLIAMS, G. AND WATTS, D. C. *Non-symmetrical dielectric relaxation behavior arising from a simple empirical decay function*. *Trans. Faraday Soc.* **66** (1970), 80 – 85.
- [135] WINEY, K. I., PATEL, S. S., AND LARSON, R. G. *Interdependence of shear deformations and block copolymer morphology*. *Macromolecules* **26** (1993), 2542 – 2549.

- 
- [136] ZAKHAROV, A. V. AND DONG, R. Y. *Rotational viscosity, dynamic phenomena, and dielectric properties in a long-chain liquid crystal: NMR study and theoretical treatment.* Phys. Rev. E **63** (2000), 011704.
- [137] ZANNA, J. J., STEIN, P., ASSFALG, N., FINKELMANN, H., MARTINOTY, P., AND BRAND, H. R. *Influence of molecular parameters on the elastic and viscoelastic properties of side-chain liquid crystalline elastomers.* Macromolecules **35** (2002), 5459 – 5465.
- [138] ZHANG, Y., WIESNER, U., YANG, Y., PAKULA, T., AND SPIESS, H. W. *Annealing effects on orientation in dynamically sheared diblock copolymers.* Macromolecules **29** (1996), 5427 – 5431.
- [139] ZILMAN, A. G. AND GRANEK, R. *Undulation instability of lamellar phases under shear: A mechanism for onion formation?* Eur. Phys. J. B **11** (1999), 593 – 608.
- [140] ZIPFEL, J., BERGHAUSEN, J., SCHMIDT, G., LINDNER, P., ALEXANDRIDIS, P., AND RICHTERING, W. *Influence of shear on solvated amphiphilic block copolymers with lamellar morphology.* Macromolecules **35** (2002), 4064 – 4076.
- [141] ZIPFEL, J., LINDNER, P., TSIANOU, M., ALEXANDRIDIS, P., AND RICHTERING, W. *Shear-induced formation of multilamellar vesicles (“onions”) in block copolymers.* Langmuir **15** (1999), 2599 – 2602.
- [142] ZIPFEL, J., NETTESHEIM, F., LINDNER, P., LE, T. D., OLSON, U., AND RICHTERING, W. *Cylindrical intermediates in a shear-induced lamellar-to-vesicle transition.* Europhys. Lett. **53** (2001), 335 – 341.
- [143] ZRÍNYI, M. *Magnetic-field-sensitive polymer gels.* Trends Polym. Sci. **5** (1997), 280 – 285.
- [144] ZRÍNYI, M., BARSÍ, L., AND BÜKI, A. *Deformation of ferrogels induced by nonuniform magnetic fields.* J. Chem. Phys. **104** (1996), 8750 – 8756.
- [145] ZRYD, J. L. AND BURGHARDT, W. R. *Steady and oscillatory shear flow alignment dynamics in a lamellar diblock copolymer solution.* Macromolecules **31** (1998), 3656 – 3670.





# Danke

Mein besonderer Dank gilt Herrn Prof. Brand. Sie gaben mir die Möglichkeit an diesem interessanten Thema zu arbeiten, dabei erhielt ich von Ihnen in vielen Diskussionen interessante und wichtige Hinweise. Die Freiheit, eigene Ideen zu verfolgen und auch mal etwas außerhalb des eigentlichen Themas zu forschen, schätzte ich sehr. Ohne diese Freiheit wäre der experimentelle Anhang wohl nie entstanden.

Weiterhin möchte ich Herrn Prof. Pleiner meinen Dank aussprechen: Meine zahlreichen Aufenthalte in Mainz bereicherten stets meine Arbeit. In den Diskussionen mit Ihnen entdeckte ich manche neue Sichtweise. Nicht zu vergessen ist aber auch der Kontakt zu den Mainzer "Simulanten", der durch meine dortigen Aufenthalte erst wachsen konnte.

Meine Aufenthalte in Mainz wären nur halb so erfolgreich gewesen, hätte ich dort nicht ein paar gute Freunde und Kollegen gefunden. Thomas, es war sehr interessant zu sehen wie ähnlich die Ergebnisse sehr unterschiedlicher Methoden sein können. Ohne Deine Simulationen wäre meine Diss wohl um ein Kapitel ärmer. Ich freue mich auf ein Wiedersehen und wünsche Dir, Daniela und Yannick alles Gute. Roland, Du hast mir den Einstieg in Mainz sehr erleichtert. Ich erinnere mich gerne an so manchen gemütlichen Abend bei gutem Essen und gutem Wein. Natürlich gilt mein Dank auch allen anderen aus der Mainzer Theoriegruppe, von denen ich nur ein paar Aufzählen kann: Doris (für die viele kleinen Hilfen), Markus, Oliver, Dirk, ...

Herrn Prof. Finkelmann danke ich für die regelmäßigen Einladungen zum Hüttenseminar. In dieser lockeren Atmosphäre gab es viele inspirierende Diskussionen, wobei es nicht ausschließlich um wissenschaftliche Themen ging.

Mes séjours à Strasbourg étaient toujours agréables et intéressants. Grâce à Philippe, Dominique, Daniel, David et Odile, j'ai pu travailler sur les gels magnétiques. J'aimerais bien vous remercier pour tous les aides précieuses, les discussions productives et tout le reste.

Special thanks also to Pat. The discussions with you were inspiring and helpful. Not to forget, your hospitality and the nice time Elke and I spent in Summit.

Meine Zeit in Bayreuth wurde mir durch viele unsichtbare Hilfen von Monika und Vanessa erleichtert. Euch beiden gilt ein ganz großer Dank, auch für das ein oder andere physik-freie Gespräch.

Ich bedanke mich bei den Bayreuther Theoretikern, die mir den Start erleichterten und über die ganze Zeit für eine gute Atmosphäre sorgten. Meinen beiden Zimmergenossen Jochen und Jean-Mathias danke ich für die schöne Zeit und der Mittagsrunde für die Diskussionen abseits der Physik: Martin, Jochen, Claus, Alexander, Oliver, Yumino und andere. Danke, Yumino für die Ausflüge in die japanische Kochkunst.

Zum Schluss gilt mein Dank meiner Familie. Elke und David, Ihr musstet in den letzten Wochen und Monaten viel auf mich verzichten. Ihr habt mich gestärkt und damit auch einen wichtigen Beitrag zum Gelingen dieser Arbeit geleistet.

Ich will nicht enden, ohne meinen Eltern herzlich zu danken. Ihre habt mir so viel ermöglicht und, wo Ihr konntet, den Rücken frei gehalten. Ohne Euch wäre ich heute nicht dort in meinem Leben, wo ich jetzt stehe. Danke.

*Les sciences ont deux extrémités qui se touchent. La première est la pure ignorance naturelle où se trouvent tous les hommes en naissant. L'autre extrémité est celle où arrivent les grandes âmes, qui, ayant parcouru tout ce que les hommes peuvent savoir, trouvent qu'ils ne savent rien, et se rencontrent en cette même ignorance d'où ils étaient partis; mais c'est une ignorance savante qui se connaît.*

*B. Pascal [102]*



# Lebenslauf

9. Dezember 1971

Geboren in Weißenburg/Bayern

September 1978 – Juli 1982

Grundschule: Volksschule Ellingen

September 1982 – Juli 1991

Werner-von-Siemens-Gymnasium, Weißenburg/Bayern

Juli 1991

Abitur

August 1991 – Oktober 1992

Zivildienst an der Landvolkshochschule Pappenheim

November 1992 – September 1998

Physikstudium an der Universität Bayreuth

November 1994

Diplom-Vorprüfung

August 1995 – Juli 1996

Auslandstudium an der Université Denis Diderot, Paris

September 1998

Diplom-Hauptprüfung

Seit Oktober 1998 Promotionsstudium



# Erklärung

Ich habe die vorliegende Arbeit selbständig verfasst und keine anderen als die von mir angegebenen Quellen und Hilfsmittel benutzt. Ferner habe ich zuvor keinen Promotionsversuch unternommen.

Bayreuth, den 21. Juli 2003

Günter Auernhammer